

Cosmic Rays in Galaxy Clusters

An on-the-fly Fokker-Planck Solver for OpenGadget3



Master thesis at the Faculty of Physics
Ludwig-Maximilians-University Munich

Submitted by
Ludwig Maximilian Böss

Supervised by
Dr. habil. Klaus Dolag

Munich, 24th of February 2020

Kosmische Strahlung in Galaxieclustern

Ein on-the-fly Fokker-Planck Solver für OpenGadget3



Masterarbeit an der Fakultät für Physik
Ludwig-Maximilians-Universität München

Eingereicht von
Ludwig Maximilian Böss

Betreut von
Dr. habil. Klaus Dolag

München, den 24.2.2020

"A process cannot be understood by stopping it. Understanding must move with the flow of the process, must join it and flow with it."

*- The First Law of Mentat,
quoted by Paul Atreides to Reverend Mother Gaius Helen Mohiam*

Frank Herbert - Dune

Contents

1. High Energy Processes in Galaxy Clusters	1
1.1. Shocks	1
1.2. Transport of Charged Particles	3
1.3. Particle (Re-)Acceleration	5
1.3.1. Diffuse Shock Acceleration	5
1.3.2. Shock Drift Acceleration	7
1.3.3. Turbulent Re-Acceleration	7
1.4. Shock Modification due to CR Particles	8
1.5. Energy Losses of Charged Particles	9
1.5.1. Protons	10
1.5.2. Electrons	11
1.6. Observational Evidence	13
2. Basis Provided by OpenGadget3	17
2.1. Hydrodynamics	17
2.1.1. SPH	18
2.1.2. Two-Component Fluid	19
2.2. Magneto-Hydrodynamics	19
2.3. Shockfinder	20
2.3.1. Implementation	21
2.3.2. Tests	23
3. Fokker-Planck Solver	27
3.1. Diffusion-Convection Equation	27
3.2. Distribution Function	28
3.3. Number- and Energy Density	29
3.4. Boundary Conditions	29
3.5. Number- and Energy Density Changes	30
3.6. Fluxes Between Momentum Bins	31
3.7. Spectral Cut	32
3.8. Slope Update	32
3.9. Distribution Function Update	33
4. Sources	35
4.1. Shock Injection	35
4.1.1. Efficiency Models	35
4.1.2. Shocktube Tests for $\eta(M)$	38

4.1.3.	Shock Obliquity	42
4.1.4.	Pre-Existing CR Component	45
4.1.5.	Slope of the Injected Spectrum	46
4.1.6.	Cosmic Ray Injection into the Model	48
4.2.	Supernovae	48
4.2.1.	Injection into the Model	49
4.2.2.	Tests	49
5.	Adiabatic Changes	51
5.1.	Fluxes	54
5.2.	Spectral Cut Update	54
5.3.	Energy Changes	55
5.4.	Standalone Tests	55
5.5.	Shocktube Tests	58
5.6.	Cosmological Tests	60
6.	Radiative Changes	65
6.1.	Fluxes	65
6.2.	Spectral Cut Update	66
6.3.	Number- and Energy Density Changes	66
6.4.	Standalone Tests	66
7.	Turbulent Re-Acceleration of Particles	71
7.1.	Explicit Solution for $D_0(t)$	71
7.2.	Fluxes	73
7.3.	Number- and Energy Density Gains	73
7.4.	Standalone Test	74
7.5.	$D_0(t)$ from Cluster Merger	74
8.	Idealized Galaxy Cluster Merger	77
8.1.	Initial Conditions	77
8.2.	Results	78
8.2.1.	Time Evolution of the Merger	79
8.2.2.	Analysis of the Initial Shock Front	82
8.2.3.	Analysis of a Single Shocked Particle	85
9.	Conclusion and Outlook	89
9.1.	This Work	89
9.2.	Future Work	90
I.	Bibliography	91
II.	List of Figures	101
III.	List of Tables	105

IV.Appendix	107
IV.1. Technical Setup of Sod Shocktubes	107
IV.2. Exact Riemann Solver	107
IV.3. Additional Figures	110
IV.3.1. Section 2	110
IV.3.2. Section 4	112
IV.3.3. Section 5	113
IV.3.4. Section 6	114
IV.3.5. Section 7	115
V. Acknowledgements	121
VI.Selbstständigkeitserklärung	123

1. High Energy Processes in Galaxy Clusters

Galaxy clusters are the largest gravitationally bound structures in the observable universe. As they form via hierarchical structure formation (e.g. White et al. (1993)) the gravitational energy from infalling structure needs to be converted into other forms of energy. This dissipated energy can be divided into two groups: thermal and non-thermal energy. The first can be observed via X-ray emission from shock-heated gas. The second can be observed as radiation from relativistic, charged particles, so called Cosmic Rays (CRs). These charged particles consist of electrons, protons and light ions, moving at relativistic velocities.

The purpose of this work is to include the treatment of these non-thermal components into the massively-parallel, cosmological SP-MHD code `OpenGadget3` to study the spectral evolution of particle populations and their impact on the simulations. We largely follow the implementation by Miniati (2001) by treating protons and electrons as CR populations and evolving their distribution in momentum space. There have been few attempts (see e.g. Girichidis et al. (2019) for recent work) to implement such a model into cosmological simulations, as it is challenging, computationally expensive and requires a lot of additional models in the code for accurate treatment of magnetic fields and the detection of shocks, among others. Even fewer attempts have been made to model the spectra of both electrons and protons. Here we present the extension of work started by Pasternak (prep) on an on-the-fly Fokker-Planck solver to model the distribution functions of electrons and protons and study their impact on cosmological simulations in future work.

1.1. Shocks

Shocks in general are caused by a relative flow of gas that exceeds the local sound speed. Assuming an ideal equation of state (EOS) this is

$$c_s = \sqrt{\frac{\gamma P}{\rho}} \quad (1.1)$$

where γ is the adiabatic index, for atomic, nonrelativistic gas $\gamma = 5/3$. Assuming that the gas far from the incoming bulk flow can't know of the incoming flow there has to be a discontinuity at which the gas first feels the incoming flow. This discontinuity is generally named the shock front. In dense plasmas where two-body collisions dominate this leads to a pile-up of particles and therefore an increase in density. With the particles

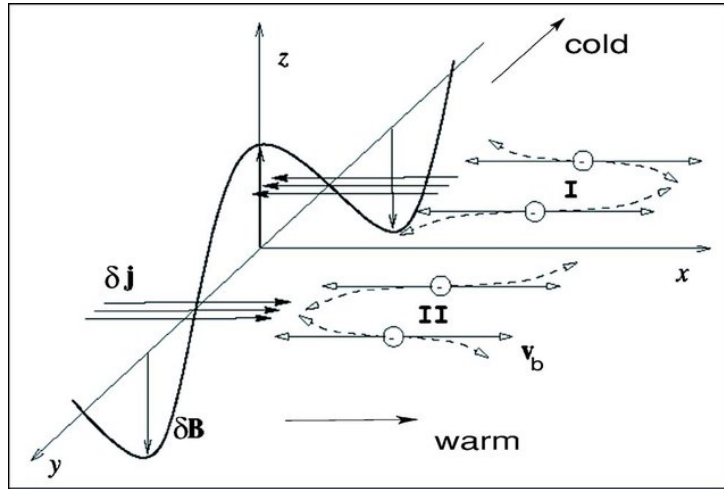


Figure 1.1.: Illustration of Weibel instability caused by a shock moving in x-direction. Taken from Startsev et al. (2007).

scattering they exchange energy and the region after the shock front, often referred to as *downstream* of the shock, is heated and becomes more turbulent compared to the region before the shock front, often referred to as *upstream*. Since the typical length scale for particle collisions is

$$\Lambda = \frac{1}{n\sigma_T} \quad (1.2)$$

where n is the particle density and σ_T is the scattering cross section, and due to the low density in most astrophysical plasmas, two-body collisions are very rare. That means that this picture cannot hold. Instead, shocks in astrophysical plasmas are often referred to as *collisionless* shocks. There are two main mechanisms for the formation of these shocks, depending on whether there is a pre-existing magnetic field or not. In the case without a pre-existing magnetic field the driving mechanism was suggested by Weibel (1959) and is therefore usually referred to as 'Weibel instability'. If the plasma is fully ionized we can consider two groups of electrons and protons/ions moving into each other due to the relative flow caused by the shock. Even though the individual groups may fulfill the essential plasma property of quasi-neutrality, once they pass through each other this neutrality is broken, as on microscopic scales there is no configuration in which the particle placement in passing can be in net neutral. This induces an electric field parallel to the shock normal, which in turn results in a magnetic field perpendicular to the shock normal. This magnetic field exerts Lorentz force on the charged particles which bends their trajectories in the direction parallel to the shock and causes random motion and thereby turbulence in the downstream region. That mechanism also causes a momentum/energy transfer between the particle groups and leads to a density increase in the downstream region, since the velocity component in the direction of the shock normal is decreased and therefore particles pile up in the downstream region. An illustration of this effect can be seen in Fig. 1.1. In the case with a pre-existing magnetic field the particles are simply deflected by the compressing fields which again leads to an energy increase and random

motion in the downstream region. Both these cases lead to a typical interaction length scale of (e.g. Maoz (2016))

$$\Lambda = \frac{v_s}{\omega_p} \quad (1.3)$$

where $\omega_p = \sqrt{\frac{4\pi e^2 n_e}{m_e}}$ is the plasma frequency and v_s is the velocity of the shock front. This is typically 9 orders of magnitude than the length scale for direct particle collisions. Independent of the shock mechanism we expect mass, momentum and energy to be conserved over the shock front. This leads to the Rankine-Hugoniot jump conditions

$$\rho_u v_u = \rho_d v_d \quad (1.4)$$

$$P_u + \rho_u v_u^2 = P_d + \rho_d v_d^2 \quad (1.5)$$

$$v_u \left(\frac{\rho_u v_u^2}{2} + \rho_u U_u + P_u \right) = v_d \left(\frac{\rho_d v_d^2}{2} + \rho_d U_d + P_d \right) \quad (1.6)$$

where the subscripts $_u$ and $_d$ refer to upstream and downstream properties of the shock front, respectively. For simplicity we only take hydrodynamic properties into account in this case. By assuming the EOS of an ideal gas to relate internal energy U of the gas to its pressure P

$$U = \frac{P}{(\gamma - 1)\rho} \quad (1.7)$$

we can solve the above equations and find the relation of up- to downstream quantity

$$\frac{\rho_d}{\rho_u} = \frac{v_u}{v_d} = \frac{(\gamma + 1)M^2}{2 + (\gamma - 1)M^2} \quad (1.8)$$

$$\frac{P_d}{P_u} = \frac{2\gamma M^2 - \gamma + 1}{\gamma + 1} \quad (1.9)$$

$$\frac{T_d}{T_u} = \frac{P_d}{P_u} \frac{v_d}{v_u} \quad (1.10)$$

where we used the Mach number $M = \frac{v_s}{c_u}$ with $v_s = \frac{v_d}{1 - \rho_u/\rho_d}$ and the sound speed in the upstream region $c_u = \sqrt{\frac{\gamma P_u}{\rho_u}}$.

1.2. Transport of Charged Particles

The trajectory of charged particles in a plasma is dominated by their own peculiar velocity and external forces acting on them. For particles with charge q the dominating force in a homogeneous magnetic field is the Lorentz force

$$\vec{F}_L = q \frac{\vec{v}}{c} \times \vec{B} . \quad (1.11)$$

Since this is strictly perpendicular to the velocity vector this forces the particles on circular tracks, in the rest-frame of the particle. In the observer frame they perform helical motions

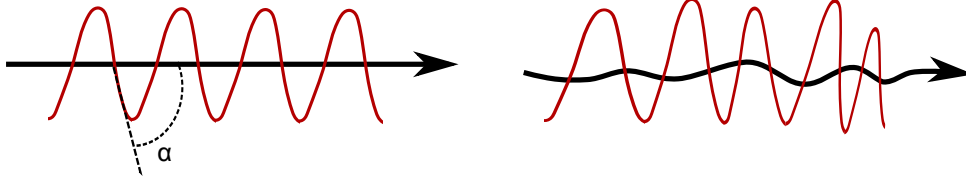


Figure 1.2.: CR propagation along a regular and irregular magnetic field line. Adopted from Pasternak (prep).

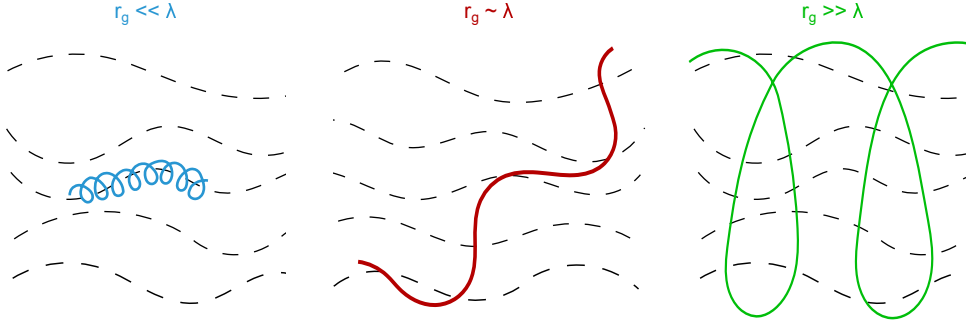


Figure 1.3.: Gyration of charged particles in irregular magnetic fields. r_g describes the gyro radius of the particle, while λ is the typical scale of the irregularities. Adopted from Pasternak (prep).

around the field lines with a pitch angle α between momentum vector \vec{p} and magnetic field vector \vec{B}

$$\cos(\alpha) = \mu = \frac{\vec{p} \cdot \vec{B}}{|\vec{p}| |\vec{B}|} . \quad (1.12)$$

This is shown in projection in the left panel of Fig. 1.2. The helical movement indicates that the Lorentz force is compensated by the centrifugal force, which allows us to define a frequency of gyration ω_c and from that a radius of gyration r_g as

$$\omega_c = \frac{qB}{\gamma mc}; \quad r_g = \frac{p_{\perp} c}{qB} \quad (1.13)$$

where γ is the Lorentz factor $\gamma = \left(1 - \left(\frac{v}{c}\right)^2\right)^{-1/2}$. We can assume that the magnetic field follows the plasma on large scales from Ohm's law

$$\vec{E} + \vec{v} \times \vec{B} = 0 \quad (1.14)$$

which is often referred to as the magnetic field lines being *frozen* into the plasma. This means that the magnetic field lines follow irregularities in the plasma and in turn charged particles follow those irregularities. See the right panel of Fig. 1.2 for an illustration. The scale of these irregularities λ together with the gyro radius r_g of a particle can impact its trajectory in different ways. This is shown in Fig. 1.3. In a simple, idealized image, if the gyro radius is much smaller than λ the particle will follow a single field line and

its irregularities. In the case of $r_g \gg \lambda$ the particle will gyrate around a bundle of field lines and won't feel small-scale irregularities. The special case of comparable scales $r_g \sim \lambda$ allows particles to leave the influence of one field line and be caught by different field lines and thereby be scattered off different irregularities. Assuming a 'sufficiently stochastic' (Drury (1983)) scattering process leads to an isotropic particle distribution, since particles should 'forget' about their initial momentum vector after a number of scattering processes. That allows us to simplify the distribution function of a particle population $F(\vec{p}, \vec{x}, t)$, which explicitly depends on the momentum vector, to an isotropic form $f(p, \vec{x}, t)$. This process is often referred to as *pitch-angle scattering*. This gives the basis to derive the Diffusion-Convection equation, which is the governing equation of our CR model, see Sec. 3.1. We will omit a derivation at this point, as it has been done by many different authors and instead refer the interested reader to Drury (1983) for a simple derivation, or Skilling (1975) for a cleaner derivation including radiative losses and Schlickeiser (2002) for a derivation including all terms discussed in Sec. 3.1.

1.3. Particle (Re-)Acceleration

Through the combination of the two previous sections we can infer some interaction between thermal gas, magnetic fields and Cosmic Rays. Depending in the structure of these velocities they fall in different categories (see e.g. Pohl et al. (2019)). If they are of stochastic origin they are considered turbulence, if they are systematic they are considered shocks, or shear flows.

1.3.1. Diffuse Shock Acceleration

The most common mechanism to explain particle acceleration by shocks is known as "Diffuse shock acceleration" (DSA), or Fermi-I acceleration after Fermi (1949). We will summarize the key concepts here, for more details please see Drury (1983) for a review. In this process charged particles with already high energies are able to escape the downstream region of a shock via the process described in Sec. 1.2. As we expect the downstream region to be turbulent and the magnetic field frozen into the gas this environment provides enough irregularities for the particle to be scattered. As the shock front itself should be small compared to the gyro radius of sufficiently relativistic particles they can enter the upstream region unperturbed by the shock. There they are reflected by the magnetic field frozen into the upstream plasma and scatter back into the downstream region. Since, from the rest frame of the shock front, the upstream velocity is much larger than the downstream velocity this causes the particle to gain energy. In the downstream region the particle is again scattered off Alfvén waves induced by the turbulent downstream medium. The scattering here causes the particle to lose some energy, but since the velocity is smaller, there is still a net energy gain of (e.g. Pohl et al. (2019))

$$\delta \equiv \frac{\Delta E}{E} \simeq \frac{4}{3} \frac{\Delta v}{c} = \frac{4}{3} \frac{x_s - 1}{x_s} M \quad (1.15)$$

where we used Eq. 1.8 to express the velocity difference between upstream and downstream region via the shock compression $x_s \equiv \frac{\rho_2}{\rho_1}$ and the Mach number M . This effect is most efficient if the magnetic field is close to parallel to the shock normal, since the particles will still gyrate around the magnetic field lines. Shocks with magnetic field lines parallel to the shock normal are often referred to as 'quasi-parallel shocks'. Additionally, as e.g. Guo et al. (2014) point out, this acceleration method is more efficient for protons and ions, than for electrons. As the gyro radius of protons is larger, due to their larger momentum, they have a higher chance of scattering into the upstream region than electrons. In contrast to that the electron gyro radius is smaller and electrons are therefore more tightly bound to the magnetic field lines and can be more easily convected downstream of the shock. Once they are convected downstream they aren't accelerated any further and can't reach the energies we observe. This leads to the 'electron injection problem'. Another benefit of this theory is that it naturally leads to a powerlaw distribution in energy/momentum (see e.g. Fermi (1949); Maoz (2016) for the complete derivation). By assuming that the energy gain δ is happening at every crossing, a particle's energy after N crossings is defined as

$$E_N = E_i(1 + \delta)^N \approx E_i e^{N\delta} . \quad (1.16)$$

Considering that with energy gain the gyro radius of the particle increases as well, we can assume that at some point r_g will be large enough for the particle to leave the shock region by random scattering and thereby leaving the acceleration mechanism. If we assign this escaping some probability P_{esc} we can derive the probability for a particle to make N passes and with that be accelerated to energy E as

$$P(E) \propto E^{-P_{esc}/\delta} \quad (1.17)$$

and from there are probability distribution of

$$\frac{dP}{dE} \propto E^{-P_{esc}/\delta - 1} . \quad (1.18)$$

To quantify P_{esc} we impose that the accelerated particles are highly relativistic so we can assume their flux over the shock front from the upstream side to be

$$f_{cr,u} = \frac{nc}{4} \quad (1.19)$$

where the factor 1/4 comes from only half the particles moving into the direction of the shock and an integration over the cosine of the isotropic pitch angle θ_i from a step we omitted here. For the relativistic particles in the downstream region we can assume that they scatter along the irregularities with velocity c . Since the irregularities themselves move with the bulk velocity of the downstream region v_d , CRs are confined to a net bulk velocity v_d , so long as they are far away from the shock front. This leads to a flux

$$f_{cr,d} = nv_d \quad (1.20)$$

and with that to an escape probability of

$$P_{esc} = \frac{f_{cr,d}}{f_{cr,u}} = \frac{nv_d}{nc/4} = \frac{4v_d}{c} \quad (1.21)$$

Inserting this into Eq. 1.18 as a substitute for the exponent, we arrive at a functional form for the slope of the probability distribution function of

$$q = \frac{3x_s}{x_s - 1} . \quad (1.22)$$

For a strong gas shock the maximum value of $x_s = 4$ can't be exceeded and we therefore arrive at a maximum slope from DSA of $q_{max} = 4$, which is very close to the observed $q_{obs} = 4.3$ for galactic CRs (e.g. Drury (1983)).

In the presence of a considerable CR component the maximum value for the compression ratio becomes larger, as we will see in Sec. 1.4 and Sec. 4.1.5. This would lead to a smaller slope, which is not matched by observations. Therefore there have been corrections for Eq. 1.22 proposed by multiple authors (e.g. Drury (1983), Berezhko and Ellison (1999), Caprioli and Haggerty (2019), Hanusch et al. (2019), Keshet et al. (2019)), which will be briefly addressed in Sec. 4.1.5.

1.3.2. Shock Drift Acceleration

In the case of a magnetic field vector which is perpendicular to the shock normal there is a second method of shock acceleration, so-called 'shock-drift acceleration'. For this effect a particle is trapped by the magnetic field compressed and amplified by the shock and moves along the shock surface and is thereby accelerated by the motional electric field (Pohl et al. (2019)). This leads to an energy gain of

$$\frac{\Delta E}{E} \propto \frac{m}{2} \vec{v}_{HT}^2 \quad (1.23)$$

where \vec{v}_{HT} is the velocity of the 'Hofmann-Teller' frame, a frame of reference in which the flow of the upstream plasma is parallel to the magnetic field. If the upstream flow is along the shock normal this is

$$\vec{v}_{HT} = \frac{\vec{n} \times (\vec{v}_u \times \vec{B}_u)}{\vec{n} \cdot \vec{B}_u} = -v_u \tan \theta_B \hat{e}_z . \quad (1.24)$$

Here \vec{n} is the shock normal, \vec{v}_u is the upstream velocity, \vec{B}_u is the vector of the upstream magnetic field, θ_B is the angle between shock normal and magnetic field vector and \hat{e}_z is the perpendicular component of the magnetic field. Even though this effect is believed to only be relevant for particle trajectories very close to perpendicular to the shock normal and therefore a small set of parameters (Pohl et al. (2019)) it is found to be a relevant contribution in accelerating CR electrons in low Mach number shocks (e.g. Guo et al. (2014)). This has the potential of solving the electron injection problem, which would be important in explaining observations from galaxy clusters.

1.3.3. Turbulent Re-Acceleration

Similar to Sec. 1.3.1 turbulent re-acceleration is caused by the scattering off MHD irregularities (see e.g. Petrosian (2001)). In the absence of a shock these irregularities can form

turbulent structures in the plasma. These structures move with a speed V in any random direction and a charged particles moving with velocity v can bounce off these structures and gain energy per scattering (see e.g. Pohl et al. (2019))

$$\frac{\Delta E}{E} \simeq 2 \frac{V^2}{c^2} + \frac{2vV \cos\theta}{c^2} . \quad (1.25)$$

Since there is a weak preference for head-on collisions compared to tail-on collisions of particles, because the relative velocities are larger in the head-on case (Fermi (1949)), when averaged over all angles θ the second term gives a small number also scaling with $\frac{v^2}{c^2}$. This makes the entire process of second order in V , which is why it is also often referred to as 'second order Fermi acceleration', again after Fermi (1949). The fact that it is second order also means that it is not very efficient, since $V \ll c$, but it is expected to be relevant for re-acceleration of particles. As e.g. Brunetti et al. (2001) point out, this effect is particularly relevant for radio emission on large scales. Since high energy losses are very efficient for electrons, as we will see in Sec. 1.5.2, electrons should cool off too fast to be able to disperse over the whole cluster, after the initial shock acceleration. With a consistent re-acceleration process the electrons could balance the loss mechanisms and therefore still be visible in radio over the diffusion timescales.

1.4. Shock Modification due to CR Particles

Now that we have a CR component injected due to the previously described processes, we can look at how this component modifies the region immediately downstream of the shock front, the *post-shock* region. For this we need to relate CR energy U_{cr} to the pressure P_{cr} via an equation of state. Since we assumed that the particle movement is random due to the pitch-angle scattering off magnetic irregularities, as discussed in Sec. 1.2, we can infer the EOS of an ideal gas

$$P_{cr} = (\gamma_{cr} - 1) \rho U_{cr} \quad (1.26)$$

where $\gamma_{cr} = 4/3$ for a gas of relativistic particles. Since the total pressure and total energy must be the same in the post-shock region with, or without CRs we can define a set of equations

$$P_{tot} = (\gamma_{th} - 1) \rho_1 U_{th} + (\gamma_{cr} - 1) \rho_1 U_{cr} = (\gamma_{th} - 1) \rho_0 U_{th} \quad (1.27)$$

$$E_{tot} = \rho_1 U_{th} + \rho_1 U_{cr} + \frac{1}{2} \rho_1 v^2 = \rho_0 U_{th} + \frac{1}{2} \rho_0 v^2 \quad (1.28)$$

where the LHS describes the case with and the RHS without CRs. It follows trivially from Eq. 1.27 that ρ with and without CRs can't be the same:

$$(\gamma_{th} - 1) \rho_1 U_{th} + (\gamma_{cr} - 1) \rho_1 U_{cr} = (\gamma_{th} - 1) \rho_0 U_{th} \xrightarrow{\rho_1 = \rho_0} U_{cr} = 0 \quad (1.29)$$

By explicitly distinguishing the densities of each case we can construct a set of equations and solve those for the new post-shock density with CR component ρ_1 .

$$(\gamma_{th} - 1) \rho_1 U_{th} + (\gamma_{cr} - 1) \rho_1 U_{cr} = (\gamma_{th} - 1) \rho_0 U_{th} \quad (1.30)$$

$$\rho_1 U_{th} + \rho_1 U_{cr} + \frac{1}{2} \rho_1 v^2 = \rho_0 U_{th} + \frac{1}{2} \rho_0 v^2 \quad (1.31)$$

Multiplying Eq. 1.31 with $(\gamma_{th} - 1)$ gives

$$(\gamma_{th} - 1) \rho_1 U_{th} + (\gamma_{th} - 1) \rho_1 U_{cr} + (\gamma_{th} - 1) \frac{1}{2} \rho_1 v^2 = (\gamma_{th} - 1) \rho_0 U_{th} + (\gamma_{th} - 1) \frac{1}{2} \rho_0 v^2 \quad (1.32)$$

where we can readily identify the first term on the right-hand side with the right-hand side of Eq. 1.30 and substitute it

$$(\gamma_{th} - 1) \rho_1 U_{th} + (\gamma_{th} - 1) \rho_1 U_{cr} + (\gamma_{th} - 1) \frac{1}{2} \rho_1 v^2 = (\gamma_{th} - 1) \rho_1 U_{th} + (\gamma_{cr} - 1) \rho_1 U_{cr} + (\gamma_{th} - 1) \frac{1}{2} \rho_0 v^2 \quad (1.33)$$

Solving this for ρ_1 gives

$$\frac{\rho_0 - \rho_1}{\rho_1} = \frac{2(\gamma_{th} - \gamma_{cr})U_{cr}}{(\gamma_{th} - 1)v^2} \quad (1.34)$$

$$\rho_1 = \frac{\rho_0}{1 - \frac{2(\gamma_{th} - \gamma_{cr})U_{cr}}{(\gamma_{th} - 1)v^2}} \quad (1.35)$$

and we can therefore see that in the case with CR energy in the post-shock region the density is higher. This of course has implications for the compression ratio and therefore the power-law slope of the distribution function as we derived it in Sec. 1.3.1, as already mentioned.

Other effects like the amplification of magnetic fields, or more complex feedback mechanisms within shock fronts (see e.g. the chapter on non-linear effects in Drury (1983)) are beyond the scope of this work, but should be considered in the future. Especially for implementing Riemann solvers for MFM (see Hinz, in prep.) these effects need to be reconsidered. For completion and as a mental note we refer to the work of Kudoh and Hanawa (2016) on this matter.

1.5. Energy losses of Charged Particles

Charged particles will lose energy due to their movement through surrounding material and magnetic fields. We will briefly discuss the most relevant loss processes in this section. Considering Fig. 1.4 we can see the different contributions to energy losses of protons and electrons. Shown here are the cooling times of individual processes at given particle energies. Cooling times are generally defined as the time it takes a particle of momentum p to lose all its momentum

$$\tau = \frac{p}{b(p)} \quad (1.36)$$

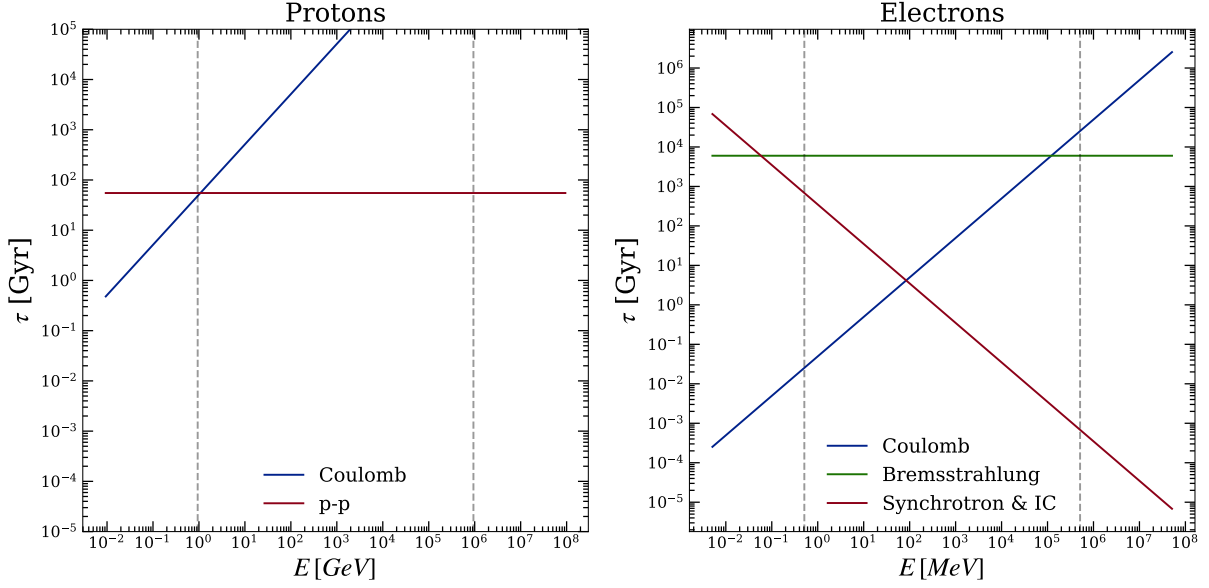


Figure 1.4.: Cooling times of different loss mechanisms for protons and electrons. Dotted lines indicate the typical energy range used for the simulations in this work.

where

$$b(p) = \frac{dp}{dt} \quad (1.37)$$

can be a number of loss processes. In order to stay consistent and for easy comparison we use the formulation by Miniati (2001) and references therein for the individual processes. For simplification most of these loss functions use the dimensionless velocity of a particle

$$\beta = p (1 + p^2)^{-1/2} \quad (1.38)$$

and the Lorentz factor

$$\gamma = (1 + p^2)^{1/2} . \quad (1.39)$$

1.5.1. Protons

For protons the dominant loss processes are Coulomb losses. Coulomb losses are caused by charged particles moving through a medium of other charged particles. In a dense gas, the particle interaction is more frequent and the protons have a high probability to collide with other protons and scatter, which leads to Coulomb collisions. Most astrophysical plasmas typically have a low density and therefore collisions are rare. In this case the protons move through the plasma at high velocities and are only slightly deflected by the surrounding protons. This still leads to a momentum loss, due to momentum exchange via the repelling forces of the similarly charged particles. Nonetheless it is easy to see that this effect will get smaller with larger velocities of the observed particle, since the

interaction timescale with the other particles decreases. Following Strong and Moskalenko (1998) we can formulate the loss process as a function of particle momentum as

$$\left(\frac{dp}{dt}\right)_{\text{Coulomb}} = \frac{2\pi Z^2 e^4}{m_e c^2} \ln \left(\frac{\gamma^2 m_e^3 c^4}{\pi e^2 \hbar^2 \rho} \frac{m_p \beta^4}{m_p + 2\gamma m_e} \right) \frac{\beta^3}{x_m^3 + \beta^3} \quad (1.40)$$

$$= 3.01 \cdot 10^{-29} \left(1 + \left[\ln \left(\frac{p^4/(1+p^2)}{1 + 2(m_e/m_p)(1+p^2)^{1/2}} \right) - \ln \rho \right] \frac{1}{75.7} \right) \quad (1.41)$$

$$\frac{\beta^3}{x_m^3 + \beta^3} \rho. \quad (1.42)$$

As we can see from Fig. 1.4 the cooling times in the energy range we used for simulations in this work are longer than the Hubble time. Nonetheless they are important to mediate the kinetic impact of the CR proton component, as for steep powerlaw slopes of the distribution function the majority of the energy is contained in the low energy end of the distribution function (e.g. Enßlin et al. (2007)). Even though the protons may not cool completely over the time of the simulation they can still loose a significant fraction of their energy and from that, according to Eq. 1.26, their pressure component.

Additionally we expect protons to interact hadronically with background gas. This should lead to a production of Kaons and Pions, which again decay into leptons, or gamma photons, depending on their charge (see e.g. Dolag and Ensslin (2000); Miniati (2001))

$$K^\pm \rightarrow \pi^0 + \pi^\pm \quad (1.43)$$

$$\pi^\pm \rightarrow \mu^\pm + \nu_\mu/\bar{\nu}_\mu \rightarrow e^\pm + \nu_e/\bar{\nu}_e + \nu_\mu + \bar{\nu}_\mu \quad (1.44)$$

$$\pi^0 \rightarrow 2\gamma \quad (1.45)$$

The latter provides the basis for observational constraints in galaxy clusters, as we should be able to observe the γ emission (see e.g. Griffin et al. (2014); van Weeren et al. (2019), first observational constraints were found by Brunetti et al. (2017)). The decay channel into electrons and positrons may provide a seed population for re-acceleration processes and could therefore provide the basis required for the diffuse radio halo observed in galaxy clusters, see Sec. 1.6. The loss rate due to inelastic scattering off background gas is given by Mannheim and Schlickeiser (1994) as

$$\left(\frac{dp}{dt}\right)_{\text{p-p}} = \begin{cases} 2.91 \cdot 10^{-29} (p - \beta) \rho & E_p \geq 1.22 \text{ GeV} \\ 0 & E_p < 1.22 \text{ GeV} \end{cases} \quad (1.46)$$

Since this process is stochastic we don't expect a strong energy dependence, which is confirmed by the constant cooling time shown in Fig. 1.4. This effect should be most relevant for feeding an additional source of electrons into our model to reproduce observations.

1.5.2. Electrons

As was the case for protons, the low momentum losses of electrons are dominated by Coulomb interactions. As electrons typically have lower momenta than protons, since

their high-momentum losses are so efficient, as we will see later, their collision rates are higher. The energy losses due to Coulomb interaction of electrons can be formulated as (Strong and Moskalenko (1998))

$$\left(\frac{dp}{dt}\right)_{\text{Coulomb}} = \frac{2\pi Z^2 e^4}{m_e c^2} \rho \left(\ln \left(\frac{m_e^3 c^4}{4\pi e^2 \hbar^2 Z} \right) + \ln \left(\frac{(1+p^2)^{1/2}}{\rho} \right) - \frac{3}{4} \right) \quad (1.47)$$

$$= 3.01 \cdot 10^{-29} \left(1 + \left[\ln(1+p^2)^{1/2} - \ln \rho \right] \frac{1}{73.56} \right) \rho . \quad (1.48)$$

Like was the case for protons this loss mechanism dominates the low energy range with cooling times at the low end of our simulated energy regime comparable to the cooling times at high energy.

As discussed in Sec. 1.2 charged particles move in helical trajectories around magnetic field lines. This leads to a deflection of the particle trajectory from a straight line and with that to photon emission and thereby energy loss. Additionally, as the electrons under consideration are relativistic the dipole emission in their rest-frame has to be Lorentz-transformed when changing to the observer frame. This changes the symmetric dipole emission to a beam in the direction of propagation and with that to 'relativistic beaming'. The photon emitted in this way are polarized and are easy to detect with modern radio telescopes (see e.g. Schlickeiser (2002) for more details on polarization and the emitted spectrum and van Weeren et al. (2019) for a recent review on observations). As the deflection depends on the gyro radius of the particle and therefore on the magnetic field we expect this loss mechanism to depend on the energy density of the magnetic field U_B . After averaging over the pitch angles of the electrons we arrive at a loss function due to Synchrotron radiation of (Miniati (2001))

$$\left(\frac{dp}{dt}\right)_{\text{Synch}} = \frac{4 \sigma_T p^2}{3 m_e^2 c^2} U_B \quad (1.49)$$

$$= \frac{4 \sigma_T p^2}{3 m_e^2 c^2} \frac{B^2}{8\pi} . \quad (1.50)$$

Another loss mechanism for high energy electrons is inverse Compton scattering off a background photon field. Here electrons scatter off photons and transfer a fraction of their energy to those photons, who are then up-scattered to higher frequencies. For the purpose of this work we take the cosmic microwave background (CMB) for our background photon field as energy density U_{IC} . This energy density of course depends on the redshift z with a decrease with redshift of $(1+z)^3$ coming from the 3 dimensional expansion of the universe and an additional $(1+z)$ from the cosmological redshift of the photons and therefore an energy loss. Again following Miniati (2001) we can express the energy loss due to inverse Compton scattering off CMB photons as

$$\left(\frac{dp}{dt}\right)_{\text{IC}} = \frac{4 \sigma_T p^2}{3 m_e^2 c^2} U_{IC} \quad (1.51)$$

$$= \frac{4 \sigma_T p^2}{3 m_e^2 c^2} 4.2 \cdot 10^{-13} (1+z)^4 . \quad (1.52)$$

As both these loss processes have the same dependence constants and momentum p , we can combine them to a single loss mechanism dependent on the ratio of the energy densities. Fig. 1.4 shows that these loss processes dominate the high energy range with cooling times of $\tau \sim \text{Myrs}$ and with that much smaller than simulation time-scales.

A final loss mechanism of electrons is Bremsstrahlung emission. Here electrons are bent out of their trajectories by positively charged particles and thereby emit radiation in a similar fashion to the synchrotron process. Unlike in the case with synchrotron emission this is not an ordered process and the radiation is therefore not polarized. Due to the quasi-neutrality of plasma we expect this effect to be very small, as there should be no charge-displacement large enough to matter to relativistic electrons. Following Strong and Moskalenko (1998) we can express the loss term due to Bremsstrahlung as

$$\left(\frac{dp}{dt}\right)_{\text{brem}} = 4\alpha r_e^2 \gamma m_e c^2 Z(Z+1) \rho \left[\ln(2\gamma) - \frac{1}{3}\right] \quad (1.53)$$

$$= 3.8 \cdot 10^{-33} \left(\ln \left[2(1+p^2)^{1/2}\right] - \frac{1}{3}\right) p \rho \quad (1.54)$$

Looking at Fig. 1.4 again we can see that the cooling times associated with this loss process are far to long to be relevant. Petrosian (2001) argues that the effect in general is about 3 orders of magnitude less efficient than the other loss processes. We therefore don't treat this effect in our model.

1.6. Observational Evidence

As mentioned in the introduction, we expect the gravitational energy released in hierarchical structure formation to lead to shocks and particle acceleration in galaxy clusters. Here we will briefly discuss the observational counterparts to the effects discussed in Sec. 1.1 through 1.5. This chapter will be largely based on the recent review by van Weeren et al. (2019) and references therein and we refer to this work for more detailed information.

Following their classification we can distinguish between 3 different classes of observable structures associated with cluster dynamics and CR acceleration:

- Revived AGN fossil plasma sources, phoenixes, and GReET
- Radio halos
- Cluster radio shocks (radio relics)

The first class originates from active galactic nuclei (AGN), most likely supermassive black holes that accrete material. They eject ultra-relativistic particles along jets that show steep spectra due to strong energetic losses of electrons. If the jets are still active they can be observed as part of radio galaxies, if they are revived and the particles are reaccelerated due to one of the beforementioned mechanisms, they fall in the first of our categories. We will not treat these sources in our model, as there are still many unknown

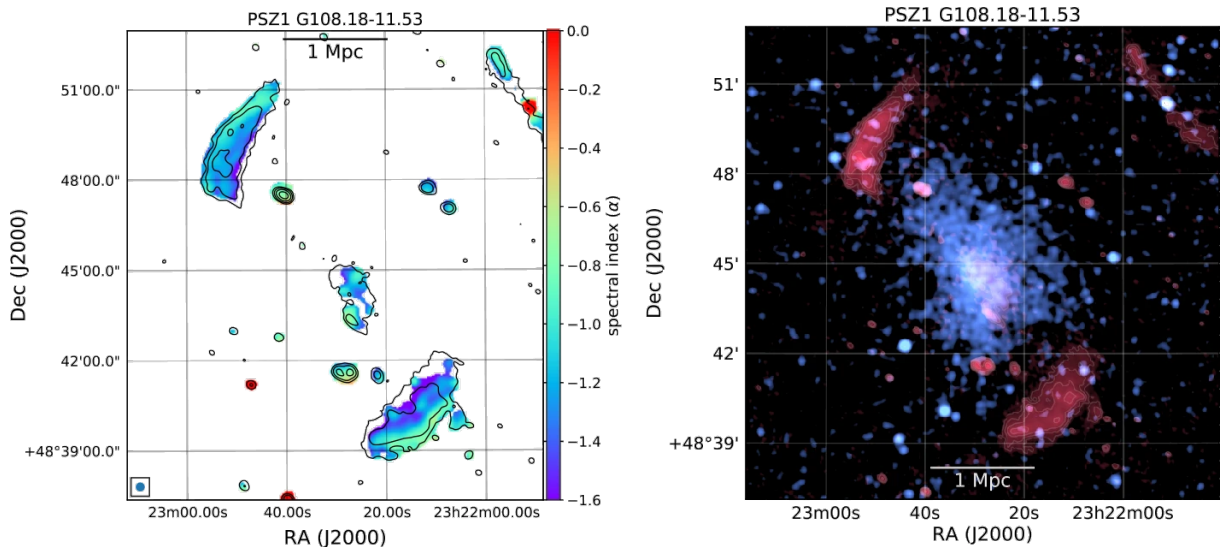


Figure 1.5.: From van Weeren et al. (2019):

Left panel: Spectral index map for the double radio shock in PSZ1G108.18–11.53 between 323 and 1380 MHz from de Gasperin et al. (2014). For both radio shocks, the spectral index steepens in the direction towards the cluster center. The 323 MHz radio contours are overlaid in black at levels of $[1, 4, 16, \dots] \times 4\sigma_{\text{rms}}$, where σ_{rms} is the map noise.

Right panel: Combined radio (red, GMRT 323 MHz) and X-ray (blue, Chandra 0.5–2.0 keV) image of PSZ1G108.18–11.53

factors concerning acceleration efficiency, slope of the injected particle distribution and the ratio between hadronic and leptonic component, see e.g. Romero et al. (2017). It would be worth to include a simple model for CR injection in the future, as they provide valuable seed populations for re-acceleration processes.

Radio halos are radio emissions on the scale of the entire cluster ($\sim 1\text{--}2$ Mpc) with a smooth and regular morphology. This halo is believed to originate from CR electrons being accelerated by shocks and diffuse over the entire cluster. This diffusion timescale should be a lot larger than the cooling timescale of the electrons, so they should not be observable. This indicates that the electrons are re-accelerated in some way, which counteracts the cooling. Radio halos are strongly correlated to the X-ray surface brightness and mostly show little substructure. They show a smooth powerlaw spectrum with a tendency for spectral steepening towards the outskirts of the halo. As van Weeren et al. (2019) point out this is poorly constraint, as there are not many observations of clusters that fix the spectrum by more than two observations at different frequencies and therefore deviations from a single slope powerlaw may be missed. Radio halos generally show no polarization, but as synchrotron emission should always be polarized this hints towards a turbulent substructure with polarization, which can't be observed with current radio telescopes. If the substructure is below the resolution limit this results in 'beam depolarization', so different polarizations within one resolution element of the observation cancel each other out.

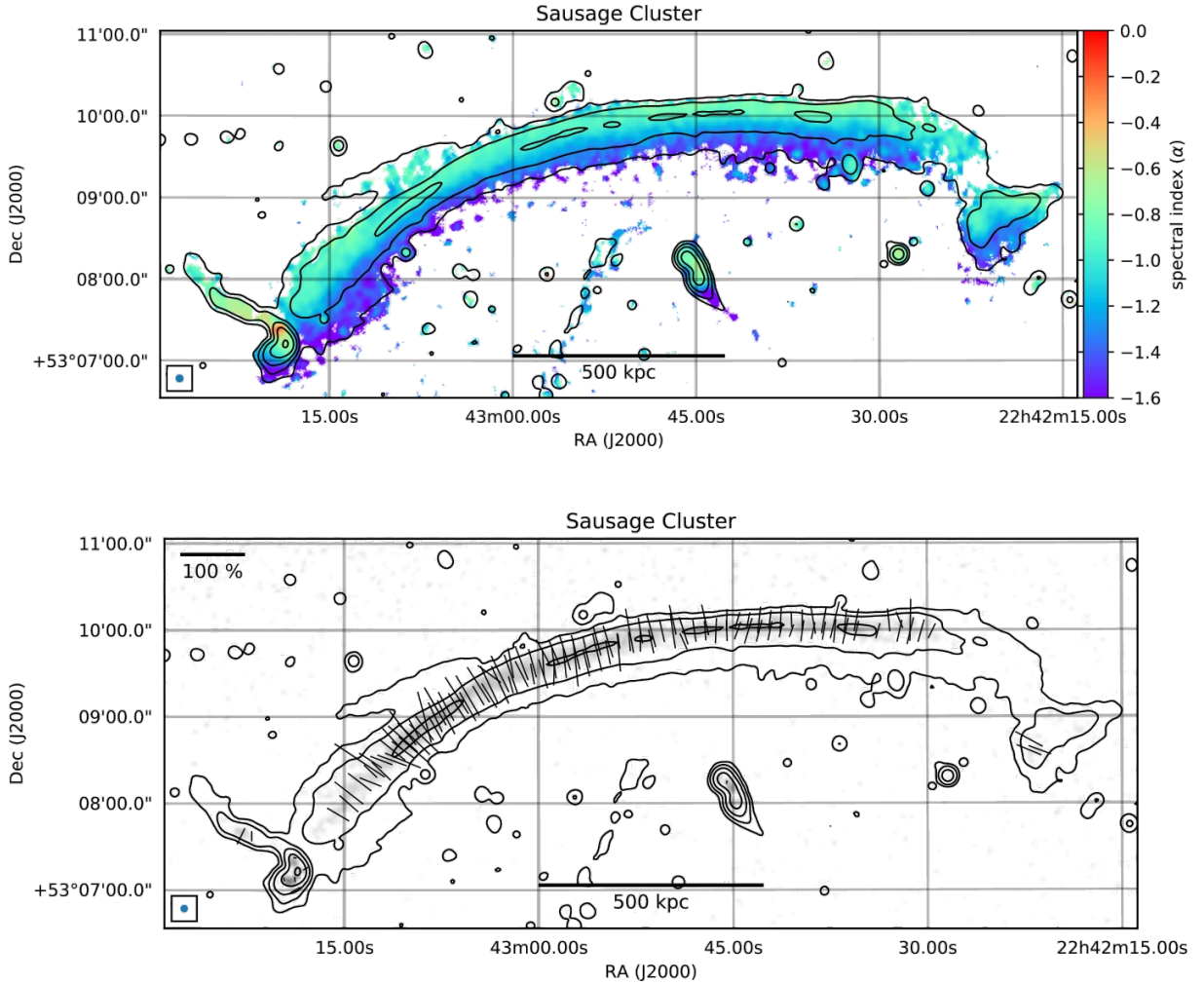


Figure 1.6.: From van Weeren et al. (2019):

Top panel: Spectral index distribution across the northern cluster radio shock in CIZA J2242.8+5301 between 0.15 and 3.0 GHz at 5" resolution (Gennaro et al. (2018)). Black contours are from a 1–4 GHz continuum image. Contours are drawn at levels of $[1, 4, 16, \dots] \times 5\sigma_{\text{rms}}$, where σ_{rms} is the map noise.

Bottom panel: Polarized intensity image at 3 GHz (Di Gennaro et al. in prep). Overlaid are the polarization electric field vectors corrected for Faraday Rotation. Black contours are the same as for the top panel

On large cluster scales we can distinguish two kind of shocks due to structure formation: Accretion shocks and merger shocks. Accretions shocks originate from the infall and accretion of gas onto the clusters at $R \sim 2 - 3R_{\text{vir}}$, where R_{vir} is the virial radius. Since the sound speed outside of the cluster is small compared to the infall velocity, this leads to very high Mach number shocks, typically expected to be $M \sim 100$. These cannot be directly observed, but are believed to impact other observables such as the Sunyaev-Zel'dovich effect, see e.g. Molnar et al. (2009).

Within galaxy clusters we expect shocks from infalling sub-structure. The Mach numbers of these shocks can be reconstructed due to the X-ray emission of the heated gas in the post-shock region as well as the spectral index of the synchrotron emission by accelerated electrons and are found to be typically $M \sim 1.2 - 4$ (e.g. Brüggen and Vazza (2020)). It has been well established that these shocks are able to accelerate particles on Mpc scales (e.g. van Weeren et al. (2010)) and that we observe the radiative losses of relativistic electrons as radio relics. These relics are elongated structures at the outskirts of the clusters which are believed to trace the shock waves of a recent merger event. In rare cases two large scale radio relics are observed, see Fig. 1.5, which can indicate the orientation of the underlying merger. The strong polarization (see bottom panel of Fig. 1.6) of the detected photons indicates ordered magnetic fields. Using measurements of the IC X-ray emission, or Faraday rotation measurements, these magnetic fields are found to be of the order $B \sim 0.1 - 5 \mu G$. Magnetic fields of this magnitude have been well reproduced in numerical simulations for some time now (see e.g. Dolag et al. (2002)). Magnetic fields are also strongly indicated by another observational feature, the spectral steepening away from the shock front, as can be seen in the top panel of Fig. 1.6. This steepening is believed to originate from energy losses of highly relativistic electrons, due to synchrotron and inverse Compton losses. As these effects are more efficient at high energies, the high energy electrons cool off faster, which leads to less emission in the high energy band and therefore a steeper spectrum.

In order to reproduce this effect in simulations, we need to model the spectrum of the CR electrons and the impact of these loss mechanisms. The spectral modeling is the purpose of this work and will give us the tools to reconstruct this observation in future cosmological simulations.

2. Basis Provided by OpenGadget3

Before we can come to the new model for CR treatment we need to take a brief look at some of the fundamental functionality of the underlying code. For this purpose we will look at the way hydrodynamics are treated with Smooth Particle Hydrodynamics (SPH), how magnetic fields are coupled to hydrodynamics and combined to Magneto-Hydrodynamics (MHD) and how we detect shocks in our simulations. Treatment of gravity, domain decomposition, multiprocessing (Springel (2005)), star formation (Springel and Hernquist (2003)), conduction (Arth et al. (2014)) and other physical processes are omitted, even though we rely on them as well, because it would exceed the scope of this work. Please see the referenced papers for more details.

2.1. Hydrodynamics

To solve hydrodynamic problems we first need to decide on how to discretize the quantities we want to observe. From the Euler equations that describe mass, momentum and energy conservation respectively (e.g. Clarke and Carswell (2014))

$$\partial_t \rho + \nabla \cdot (\rho \vec{v}) = 0 \quad (2.1)$$

$$\partial_t (\rho \vec{v}) + \rho \vec{v} \cdot \nabla \vec{v} + \nabla P = 0 \quad (2.2)$$

$$\partial_t (\rho U) + \nabla \cdot [(\rho e_{tot} + P) \vec{v}] = 0 \quad (2.3)$$

we can see that those quantities are density ρ , velocity \vec{v} , pressure P and internal energy U . This discretization comes in two main flavors: Eulerian and Lagrangian. In the Eulerian view we discretize the space in e.g. a grid and compute the quantities within a grid cell at a fixed position in space. Changes in quantity are then computed by solving the fluxes between cells. This has advantages for the hydrodynamics, such as a more accurate treatment of shocks, but is more difficult to couple to other physics, like gravity.

The second approach, Lagrangian, discretizes mass and computes the density by summing up the masses of particles within a discrete volume surrounding a moving tracer particle. All other quantities can then be computed from the continuum Lagrangian of hydrodynamics (Eq. 2.4) and how one particle's properties are affected by the surrounding particles.

$$L = \int dV [\rho v^2 - \rho U(\rho, s)] \quad (2.4)$$

The particle image can be easily coupled to gravity and other processes, while also being less prone to geometric artefacts from imposed grids. One of these Lagrangian methods is 'Smoothed Particle Hydrodynamics' (SPH), originally by Lucy (1977) and Gingold and Monaghan (1977), which is used in OpenGadget3.

2.1.1. SPH

We will briefly discuss some of the basic principles of SPH here, based on the review paper by Price (2012) and refer to this work and references therein for more details.

The basis of SPH is that we estimate the density via a sum of a number of neighboring particles. This number of particles N_{ngb} is fixed and the volume that contains this number of particles is updated as a function of h_i so that

$$N_{ngb} = \frac{4}{3}\pi h_i^3 \frac{\rho_i}{m_i} \quad (2.5)$$

where h_i gives the size of radius of the sphere in which the density is evaluated, m_i is the particle mass, ρ_i is the density and d is the mean particle separation. The radius of the sphere h_i is often referred to as the 'compact kernel support'. The kernel is a distribution function with a discrete cutoff at $r = h_i$. For the purpose of this work we use a higher order kernel suggested by Dehnen and Aly (2012), a Wendland C6 kernel, which follows

$$W(r, h_i) = \frac{1365}{64\pi h_i^3} \begin{cases} \left(1 - \frac{r}{h_i}\right)^8 \cdot \left(1 + 8 \frac{r}{h_i} + 25 \left(\frac{r}{h_i}\right)^2 + 32 \left(\frac{r}{h_i}\right)^3\right) & 0 \leq \frac{r}{h_i} < 1 \\ 0 & \frac{r}{h_i} \geq 1 \end{cases} \quad (2.6)$$

Using Eq. 2.6 we can calculate the density within our sphere of interest as

$$\rho(\vec{r}_i) = \sum_j^{N_{ngb}} m_j W(\vec{r}_i - \vec{r}_j, h_i) . \quad (2.7)$$

As can be seen Eq. 2.5 and 2.7 are degenerate in ρ and therefore need to be solved with a root-finding algorithm until the solutions converge.

All other quantities X_i are computed simply by summing up the quantities of all neighboring particles, weighted with the kernel evaluated at their distance from particle i

$$X_i = X(\vec{r}_i) = \sum_j \frac{m_j}{\rho_j} X_j W(\vec{r}_i - \vec{r}_j, h_i) . \quad (2.8)$$

In a similar fashion we can calculate the gradient of the quantity X_i by acknowledging that only the kernel depends on the particle i , which simplifies the gradient ∇X_i to the gradient of the kernel

$$\nabla X_i = \nabla X(\vec{r}_i) = \sum_j \frac{m_j}{\rho_j} X_j \nabla W(\vec{r}_i - \vec{r}_j, h_i) . \quad (2.9)$$

To obtain equations for the time evolution of the particles we derive the equations of motion from Eq. 2.4 via the least action principle to get

$$\frac{\partial L}{\partial \vec{v}_i} = m_i v_i \quad ; \quad \frac{\partial L}{\partial \vec{r}_i} = - \sum_j m_j \frac{\partial U_j}{\partial \rho_i} \Big|_s \frac{\partial \rho_j}{\partial \vec{r}_i} . \quad (2.10)$$

Using the first law of thermodynamics we can find an expression for the change in thermal energy, in modern SPH (as in `OpenGadget3`) it makes more sense to follow the change of entropy, instead of internal energy, as in the absence of dissipation it is always conserved, independent of time-integration scheme (see Sec. 3.4.3 in Price (2012) for more details). Together with an expression of the density gradient (Eqs. 26 - 28 in Price (2012)) this gives a function for the acceleration a particle experiences due to the hydrodynamic forces exerted on it by its neighboring particles

$$\vec{a}_{\text{hydro}} = \frac{D\vec{v}_i}{Dt} = - \sum_j m_j \left(\frac{P_i}{\rho_i^2} + \frac{P_j}{\rho_j^2} + \Pi_{ij} \right) \nabla_i W(\vec{r}_i - \vec{r}_j, h_i) \quad (2.11)$$

where Π_{ij} is a term for artificial viscosity, introduced to be able to deal with shocks in SPH (see e.g. Dolag et al. (2005b)). We treat this term as dynamic in time to avoid suppression of turbulence and complex flows, see Beck et al. (2015b) for more information, along with more improvements to our implementation of SPH in `OpenGadget3`. This acceleration term can be used to evolve the particles in time by any suitable time integration method and provides the basis of our hydrodynamic description.

2.1.2. Two-Component Fluid

In order to couple the additional fluid component of the cosmic rays to the hydro solver we need to make some minor adjustments to the hydro solver. For one the pressure needs to be extended from pure thermal pressure to total pressure

$$P_{\text{tot}} = P_{\text{th}} + P_{\text{cr}} . \quad (2.12)$$

Additionally we need to make sure that the total energy, or rather entropy in our case, is traced correctly. For simplicity we will look at this in the energy formulation. Since the energy is related to the pressure via an EOS for an ideal gas

$$P = (\gamma - 1) \rho U \quad (2.13)$$

and SPH conserves energy explicitly (see Eq. 38 in Price (2012)) an error in the energy evolution leads to an error in pressure, or density. To avoid this we explicitly subtract the energy converted to CRs in the acceleration process from the internal energy of the gas particles.

2.2. Magneto-Hydrodynamics

The treatment of magnetic fields and coupling to hydrodynamics as MHD was implemented by Dolag and Stasyszyn (2009). We will outline some of the key concepts here and refer to their work and references therein for more details.

To trace the time-evolution of the magnetic field one needs to solve the induction equation

$$\frac{\partial \vec{B}}{\partial t} = \nabla \times (\vec{v} \times \vec{B}) + \eta \Delta \vec{B} \quad (2.14)$$

where the magnetic diffusivity $\eta = 0$ for ideal MHD with infinite conductivity. With the additional constraints that

$$\nabla \cdot \vec{B} = 0 \quad (2.15)$$

from Maxwell's equations, we can rewrite this in the Lagrangian formalism as

$$\frac{D\vec{B}}{Dt} = (\vec{B} \cdot \nabla)\vec{u} - \vec{B}(\nabla \cdot \vec{u}) . \quad (2.16)$$

As discussed in Sec. 1.2 the dominant force on a particle in a magnetic field is the Lorentz force, which can be expressed in a symmetric, conservative form via the magnetic stress tensor as

$$M_i^{kl} = \left(\vec{B}_i^k \vec{B}_i^l - \frac{1}{2} |\vec{B}_i|^2 \delta^{kl} \right) \quad (2.17)$$

where the subscripts describe the corresponding particles, the superscripts the tensor/vector elements with $i, j \in \{1, 2, 3\}$ and δ^{kl} being the Kronecker delta. This gives a term for the acceleration of a particle due to the Lorentz force of

$$\vec{a}_{mag} = \frac{D\vec{v}_i}{Dt} = \frac{1}{\mu_0} \sum_j m_j \left[f_i^{co} \frac{M_i}{\rho_i^2} \nabla_i W_i + f_j^{co} \frac{M_j}{\rho_j^2} \nabla_j W_j \right] \quad (2.18)$$

where μ_0 is the vacuum permeability and $f_{i,j}^{co}$ are correction terms due to the variability of $h_{i,j}$ that we omitted in the case of SPH for simplicity. Eq. 2.11 and 2.18 can be easily combined to a total acceleration working on the particle and then integrated in time.

A common problem in MHD is that due to a finite numerical accuracy Eq. 2.15 is not strictly zero. This can be counteracted by introducing divergence cleaning schemes, or formulating Eq. 2.16 in such a way that Eq. 2.15 is always zero by design. Please see Dolag and Stasyszyn (2009), or Price (2012) for more information.

2.3. Shockfinder

As discussed in Sec. 1.3 the main source for relativistic particles in galaxy clusters are shocks. Identifying shocks in the simulation is therefore of fundamental importance for our model to work. There have been numerous attempts at on-the-fly shockfinding in simulations, e.g. Pfrommer et al. (2006) via entropy jumps in *Gadget2*, Schaal and Springel (2014) using the temperature gradient in *Arepo*, or Vazza et al. (2012) using temperature jumps in *Enzo*. For this work we use the shockfinder implemented in *P-Gadget3* by Beck et al. (2015a). The schematics of the shockfinder can be seen in Fig. 2.1 and we will briefly outline the implementation in the following.

2.3.1. Implementation

This implementation is based on pressure gradients, so in a first step we calculate the shock normal \vec{n}_i by finding the pressure gradient within the kernel

$$\vec{n}_i = -\frac{\nabla P_i}{|\nabla P_i|} . \quad (2.19)$$

This is very cheap in SPH as the gradient of a quantity can simply be calculated by the gradient of the kernel, as discussed in Sec. 2.1.1.

$$\nabla P_i = \frac{1}{\rho_i} \sum_j m_j (P_j - P_i) \nabla_i W(r_{ij}) \quad (2.20)$$

where r_{ij} is the absolute distance between particle i and j , divided by the kernel support h_i

$$r_{ij} = \frac{|\vec{x}_i - \vec{x}_j|}{h_i} \quad (2.21)$$

We then calculate a first weighting of the contribution of particle j to the up, or down-stream properties of the shock by projecting the position of particle j within the kernel onto \vec{n}_i . The criteria for being upstream or downstream are defined as

$$\vec{n}_i \cdot (\vec{x}_i - \vec{x}_j) < 0 \quad \rightarrow \text{upstream} \quad (2.22)$$

$$\vec{n}_i \cdot (\vec{x}_i - \vec{x}_j) > 0 \quad \rightarrow \text{downstream} . \quad (2.23)$$

As we expect the shock to be broadened by the kernel we want to get as close to the actual upstream and downstream quantities as possible by weighting the contribution of particle j higher, the further away it lies from particle i . We can easily get this by using the inverted kernel value at the position of particle j . This concept is illustrated in Fig. 2.1 (c). At the exact midpoint of the broadened shock this should reconstruct the exact upstream and downstream properties. We can obtain the inverted kernel value in the cheapest way by inverting the distance

$$r_{ij}^F = \left| 1 - \frac{\vec{n}_i \cdot (\vec{x}_i - \vec{x}_j)}{h_i} \right| \quad (2.24)$$

where F denotes that this distance is used as a first weighting step. As a second, optional, weighting step we use the distance perpendicular to the shock normal \vec{n}_i by constructing two perpendicular normal vectors $\vec{n}_{i,2}$ and $\vec{n}_{i,3}$ along the remaining two spacial dimensions. $\vec{n}_{i,2}$ can be obtained by constructing a perpendicular vector \vec{w}_2

$$\vec{w}_2 = \begin{pmatrix} 0 \\ -n_i^x \\ n_i^y \end{pmatrix} \quad (2.25)$$

where the superscripts x and y denote the respective spacial components of the shock normal, and projecting the shock normal onto that vector

$$\vec{n}_{i,2} = \vec{w}_2 - (\vec{n}_i \cdot \vec{w}_2) \vec{n}_i . \quad (2.26)$$

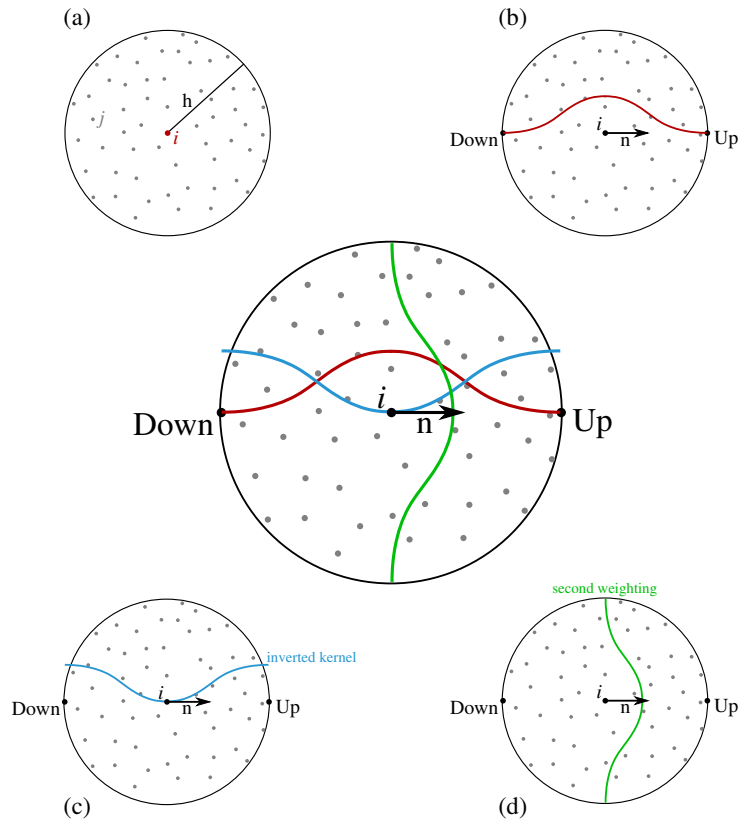


Figure 2.1.: Schematics of the shockfinder. Taken from Beck et al. (2015a).

The second perpendicular vector can then be simply be obtained from the cross-product of the two others

$$\vec{n}_{i,3} = \vec{n}_i \times \vec{n}_{i,2} . \quad (2.27)$$

Projecting the particle distances on these vectors gives the distances to evaluate the second and third weighting

$$r_{ij}^S = \left| \frac{\vec{n}_{i,2} \cdot (\vec{x}_i - \vec{x}_j)}{h_i} \right| \quad (2.28)$$

$$r_{ij}^T = \left| \frac{\vec{n}_{i,3} \cdot (\vec{x}_i - \vec{x}_j)}{h_i} \right| . \quad (2.29)$$

That way we can emphasize the contribution of particles close to the shock normal. This is useful in the case of round shock structures, as we avoid geometric projection effects. With the distances at which the kernel will be evaluated defined, we can calculate the total weight for the shock finder evaluation as

$$w_{ij} = m_j^3 W(r_{ij}^F) W(r_{ij}^S) W(r_{ij}^T) . \quad (2.30)$$

From this we can calculate the contribution of fluid quantity X to the upstream, or downstream value as

$$X_{up/down,i} = \sum_{j^{d,u}} w_{ij} X_j / \sum_{j^{d,u}} w_{ij} . \quad (2.31)$$

While the second and third weighting are only used to assure that the difference in upstream and downstream velocity is larger than along the shock surface, the first weighting is used to calculate the shock quantities. Before calculating the shock properties we employ a number of filters to avoid false detections. These filters make sure that the pressure and density jump are larger than 5% and that the velocity divergence is larger than the turbulent velocity. See Beck et al. (2015a) for more details. If the upstream and downstream properties quantify the system as a shock we can first obtain the shock compression trivially from

$$x_s = \frac{\rho_d}{\rho_u} \quad (2.32)$$

and from that the shock speed

$$v_s = \frac{|v_d - v_u|}{1 - 1/x_s} . \quad (2.33)$$

The Mach number is simply defined as

$$M = \frac{v_s}{c_{s,u}} \quad (2.34)$$

where the upstream sound speed $c_{s,u}$ is defined as

$$c_{s,u} = \sqrt{\frac{\gamma P}{\rho}} . \quad (2.35)$$

To account for the CR fluid component we follow Hopkins et al. (2020a) and modify the sound speed to

$$c_s = \sqrt{\frac{\gamma_g P_g + \gamma_{cr} P_{cr}}{\rho}} \quad (2.36)$$

It has to be noted that this is actually not as straight-forward as it seems and has to be handled with caution (see e.g. the section on non-linear effects in Drury (1983)). For the purpose of this work and the idealized simulations we find the simplification to work well, but it should be reconsidered for later, more complex systems.

2.3.2. Tests

To test the accuracy of the shock finder we set up a series of shocktubes. For a detailed description of initial condition construction please see Sec. IV.1, we will only briefly outline the setup here. First we set up a density gradient via different stacking of glass files¹, this is usually $\rho_L = 1$ and $\rho_R = 1/8$. Next we set up a pressure gradient. We chose

¹Glass files are cubes with particles positioned in such a way that the distribution is relaxed and force-free.

to keep the left, high pressure, side of the tube fixed and varied the pressure on the right, low pressure, side. These kind of shocktubes, so-called Sod-shocks (after Sod (1978)) are a standard Riemann problem and can be solved analytically. We followed the description of Pfrommer et al. (2006) for implementing an exact Riemann solver, see Sec. IV.2 for a description of the individual steps of the solution. We added an additional layer of root-finding to be able to set up a shock with a given density gradient and pressure on the left side and solve it for a target Mach number. This way we can make sure that the initial pressure gradient leads to a shock with a given Mach number and compare that to the result of our shock finder.

The results of these tests are shown in Fig. 2.2. From left to right we show density, velocity in x-direction, internal energy and the result of the shock finder. The different tests have a target Mach number of 1.5, 3, 6, 10, 30 and 60, from top to bottom. Solid lines show the result of the simulation, with every SPH particle plotted, to show eventual numerical noise. At the right column we give target Mach number, maximum detected Mach number, the width of the shock in units of the mean kernel support h_{sml} and the number of shocked particles. Additionally we show the size of the kernel of the particle with the maximum Mach number with the red error bars.

Overall the results show very good agreement with the exact solution. The density profile shows the typical SPH artifacts, like the density 'blip' at the contact discontinuity, or the broadening of the shock by smoothing out the shock transition, but the relevant states of the different shock zones are fit very well. We also note that the solution stays very stable, even for shocks with very high Mach numbers. We performed these tests with the public version of **Arepo** as well to compare our SPH solutions to a grid(-like) code. These results can be seen in Fig. IV.2 for a Mach 3 shock and Fig. IV.3 for a Mach 30 shock. We found that our solution fits the analytic solution very nicely, even compared to **Arepo** using a static mesh and an exact Riemann solver. This gives us confidence that our treatment of shocks is sufficiently accurate to be used in the CR model.

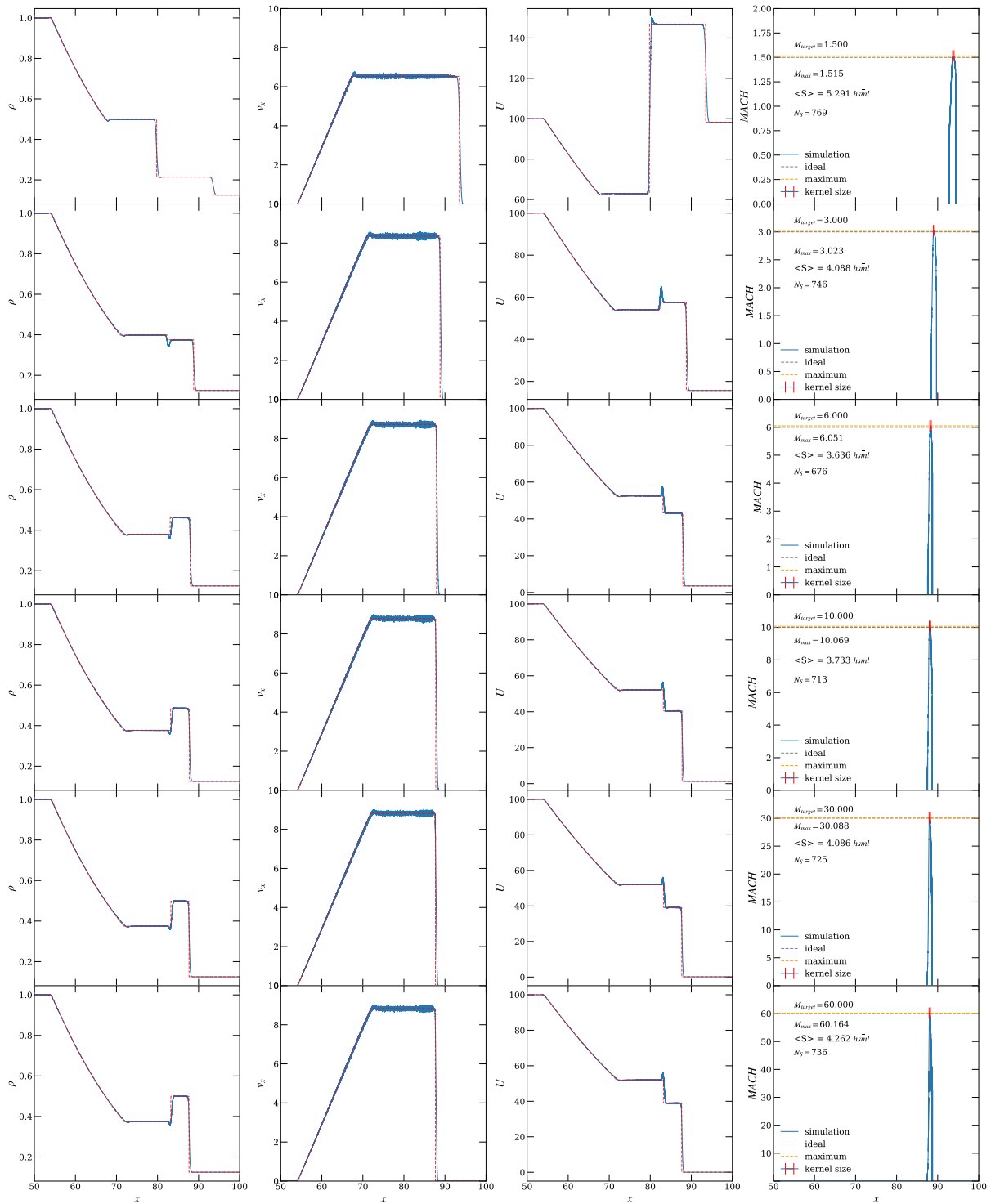


Figure 2.2.: Results of the shockfinder performance tests. Left to right panels display density, velocity component in x direction, internal energy of the gas and machnumber of the resulting shock. The red errorbars in the machnumber panels indicate the mean size of the kernel support. Included in these panels is information in the target machnumber, the width of the shock in units of the mean kernel support, as well as the number of SPH particles within the shock.

3. Fokker-Planck Solver

As the mass resolution of cosmological simulations is typically 60 orders of magnitude above a proton mass, we of course cannot trace individual Cosmic Ray particles. We therefore treat the CR component in our simulation as a population of CRs and trace the evolution of this population. For this we need to follow the time evolution of the distribution function of the CRs. Equations that describe the change of a distribution function are generally called Fokker-Planck equations, after Fokker (1914) and Planck (1917).

In this chapter we show the basic assumptions and principles used for the time evolution of the distribution function. The exact implementation and detailed description of the individual processes can be found in the following chapters.

3.1. Diffusion-Convection Equation

For CR evolution the Fokker-Planck equation we need to solve is known as the Diffusion-Convection equation (see Skilling (1975) for a complete, or Drury (1983) for a more compact derivation) and takes the form

$$\frac{\partial f}{\partial t} + \vec{u} \cdot \nabla f = \frac{Df}{Dt} = \nabla (\kappa(p) \nabla f) \quad (3.1)$$

$$+ \frac{1}{3} (\nabla \cdot \vec{u}) p \frac{\partial f}{\partial p} \quad (3.2)$$

$$+ \frac{1}{p^2} \frac{\partial}{\partial p} \left(p^2 \left[\sum_l b_l f + D_{pp} \frac{\partial f}{\partial p} \right] \right) \quad (3.3)$$

$$- \frac{f(p, \vec{x}, t)}{t_c(p, \vec{x})} \quad (3.4)$$

$$+ j(\vec{x}, p) \quad (3.5)$$

The different processes that play into the time evolution are as follows.

The LHS of Eq. 3.1 describes the time- and space dependent evolution of the distribution function. In the Eulerian formulation of hydrodynamics these parts must be traced individually, but since this work uses the Lagrangian formulation in SPH it can be combined to the convective derivative $\frac{Df}{Dt}$, mid section of Eq. 3.1. The RHS of Eq. 3.1 describes the spacial diffusion of the distribution, which for the scope of this work is omitted. We will discuss future steps to address this term in the conclusion.

Eq. 3.2 traces the adiabatic changes, so the impact of the thermal gas component of the

distribution, and will be described in Sec. 5.

The first part of Eq. 3.3 describes the radiative losses, with b_l being the individual loss mechanisms for electrons and protons. The second part models the diffusion in momentum space due to turbulent reacceleration, where the re-acceleration coefficient D_{pp} can be chosen to either be constant, or calculated for every timestep following Cassano and Brunetti (2005). See Sec. 7 for details.

Eq. 3.4 gives an additional term for catastrophic losses, where particle numbers are not conserved (see e.g. Schlickeiser (2002)). This term will be addressed in future work.

Lastly Eq. 3.5 contains the source-term for CRs. In this work we focus on only two source mechanisms: Acceleration by shocks (Sec. 4.1) and a subgrid model of Type II supernovae (Sec. 4.2).

3.2. Distribution Function

In principle particles are distributed in phase-space according to their momentum vector \vec{p} and their position vector \vec{x} at time t in the distribution function $F(\vec{p}, \vec{x}, t)$. Assuming a 'sufficiently stochastic' (Drury (1983)) scattering process, as described in Sec. 1.2, we can infer that the particle movement is random on small scales and treat the distribution of the CRs as isotropic. This simplifies the integral over all momentum vectors that would be required to obtain the number- and energy density from $F(\vec{p}, \vec{x}, t)$, to a simple integral in momentum-space over all required absolute momenta.

$$F(\vec{p}, \vec{x}, t) \rightarrow 4\pi p^2 f(p, \vec{x}, t) \quad (3.6)$$

With this simplification the Diffusion-Convection Equation can be used to trace the CR properties number- and energy density. This can be done either as a whole population as done e.g. by Hanasz and Lesch (2003); Enßlin et al. (2007); Pfrommer et al. (2016); Hopkins et al. (2020a), or by dividing the population into bins in momentum space as first proposed by Miniati (2001) and reproduced in recent work e.g. by Winner et al. (2019) or Girichidis et al. (2019). In this work we also try to explicitly model the CR distribution function. In order to do this we first need to discretize the distribution. Since observations of the CR spectrum (see e.g. Hillas (2006)) show that they follow in first order a powerlaw in energy it makes sense to discretize the distribution by piece-wise powerlaw functions and evolve the resulting bins in time. That way, as the number of powerlaw bins increases, the modeled spectrum approximates any desired distribution. Our model for the distribution function follows the functional form

$$f(p) = f_i \left(\frac{p}{p_i} \right)^{-q_i} \quad (3.7)$$

and is therefore defined by the norm of the i -th momentum bin f_i , its momentum p_i and the slope of the bin q_i .

3.3. Number- and Energy Density

From the distribution function $f(p)$ we can obtain the number density as a simple integral in momentum space

$$N_i = \frac{1}{\rho} \int_{p_i}^{p_{i+1}} dp 4\pi p^2 f(p) \quad (3.8)$$

where the volume integral in momentum space over the distribution function gives us the number of particles contained in that momentum volume. The energy density can be calculated by assuming that every particle carries an energy $T(p)$. As we deal with strictly relativistic particles we can use the relativistic energy-momentum relation

$$T(p) = pc \quad (3.9)$$

which greatly simplifies our integrals.

$$E_i = \frac{1}{\rho} \int_{p_i}^{p_{i+1}} dp 4\pi p^2 T(p) f(p) \quad (3.10)$$

$$= \frac{1}{\rho} \int_{p_i}^{p_{i+1}} dp 4\pi c p^3 f(p) \quad (3.11)$$

Since we discretized our distribution function $f(p)$ in Eq. 3.7 these equations can be solved analytically by inserting the discretisation.

$$N_i = \frac{4\pi f_i}{\rho p_i^{-q_i}} \int_{p_i}^{p_{i+1}} dp p^{2-q_i} \quad (3.12)$$

$$= \frac{4\pi f_i p_i^3}{\rho} \frac{\left(\left(\frac{p_{i+1}}{p_i} \right)^{3-q_i} - 1 \right)}{3 - q_i} \quad (3.13)$$

$$E_i = \frac{4\pi c f_i}{\rho p_i^{-q_i}} \int_{p_i}^{p_{i+1}} dp p^{3-q_i} \quad (3.14)$$

$$= \frac{4\pi f_i p_i^4}{\rho} \frac{\left(\left(\frac{p_{i+1}}{p_i} \right)^{4-q_i} - 1 \right)}{4 - q_i} \quad (3.15)$$

3.4. Boundary Conditions

To properly decouple the CR fluid component from the non-relativistic gas we need to set the boundary conditions of our distribution function accordingly. For the presented work we chose open boundaries at the lower end of the distribution function and closed boundaries at the upper end. The physical motivation of this is that, as CRs cool and lose energy/momentum they smoothly transition to the non-relativistic thermal pool of

particles. This will be discussed in more detail in Sec. 5. For this assumption to hold, the lower end of the distribution function should be well in the relativistic regime.

It is worthy to note that this shifts the problem of accurately handling semi-relativistic particles to the hydro solver. For our purposes we assume a gap in the transition between the Maxwell-Boltzmann distribution of particles and the powerlaw high-energy tail. That way we can treat our implementation as a two component fluid with distinct equations of state with a sharp jump between the two and postpone the problem of an intermediate state.

The upper end of the distribution function is chosen to have a closed boundary. In order to achieve this we employ a movable upper boundary that also works as a cutoff of the distribution. This parameter needs to be updated at every timestep, the implementation of this will be discussed in Sec. 3.7. Here the physical motivation is that particles can be further accelerated beyond the arbitrarily chosen initial upper limit of the distribution function. Numerically we avoid an artificial pile-up of energy and particles in the last momentum bin.

3.5. Number- and Energy Density Changes

The key point of evolving the distribution function is to trace the changes in number- and energy density in time. For simplicity we can follow the approach by Miniati (2001) and Pasternak (prep) and derive this as an example for adiabatic changes and radiative losses. The part of the diffusion-convection equation governing those effects is

$$\frac{Df}{Dt} = \frac{1}{3} \frac{\partial u}{\partial x} p \frac{\partial f}{\partial p} + \frac{1}{p^2} \frac{\partial}{\partial p} (p^2 b_l f) . \quad (3.16)$$

By multiplying both sides of Eq. 3.16 with $4\pi p^2/\rho$ to be able to associate the LHS with Eq. 3.8 and integrating both sides over the i -th momentum bin we arrive at

$$\frac{DN_i}{Dt} = \frac{1}{\rho} \left\{ \left(\frac{1}{3} \frac{\partial u}{\partial x} p + b_l(p) \right) 4\pi p^2 f(p) \right\}_{p_i}^{p_{i+1}} . \quad (3.17)$$

Here we used integration by parts, since both terms in Eq. 3.16 are of shape $f(p)g'(p)$. As proposed by Miniati (2001) we can integrate this in time and can identify the RHS as the time averaged fluxes over the momentum boundaries. We will discuss the solution for the fluxes in Sec. 3.6. This gives us a number density of the i -th bin after a timestep Δt

$$N_i^{t+\Delta t} = N_i^t + \frac{1}{\bar{\rho}} \left(F_{n_{i+1}}^m - F_{n_i}^m \right) \quad (3.18)$$

where $F_{e_{i+1}}^m$ and $F_{e_i}^m$ are the number density fluxes into and out of the bin respectively. $\bar{\rho}$ denotes the mean density over the timestep.

Similarly, to obtain the energy after a timestep we multiply Eq. 3.16 with $4\pi cp^3/\rho$ to be able to associate the LHS with Eq. 3.11 and perform the same integral as before. Unlike

in the previous integral the second term of the partial integration does not cancel out and we are left with a somewhat more complex function

$$\frac{DE_i}{Dt} = \frac{1}{\rho} \left\{ \left(\frac{1}{3} \frac{\partial u}{\partial x} p + b_l(p) \right) 4\pi c p^3 f(p) \right\}_{p_i}^{p_{i+1}} - \left(\frac{4}{3} \frac{\partial u}{\partial x} E_i + \frac{1}{\rho} \int_{p_i}^{p_{i+1}} dp b_l(p) 4\pi c p^2 f(p) \right). \quad (3.19)$$

To simplify this equation we can introduce the quantity $R_i(q_i, p_i)$ as a shorthand for the energy loss integral per bin

$$R_i(q_i, p_i) = \frac{4 - q_i}{p_{i+1}^{4-q_i} - p_i^{4-q_i}} \int_{p_i}^{p_{i+1}} dp p^{2-q_i} \left(\frac{1}{3} \frac{\partial u}{\partial x} + \sum_l^{N_{losses}} b_l(p) \right). \quad (3.20)$$

Here again $\frac{1}{3} \frac{\partial u}{\partial x}$ denotes the adiabatic changes and $\sum_l^{N_{losses}} b_l(p)$ the individual radiative loss processes. In most cases these factors can't be solved in one step, but need to be split up in individual processes. As in Miniati (2001) we can now express the energy of a particle after the timestep Δt as

$$E_i^{t+\Delta t} \left(1 + \frac{\Delta t}{2} R_i(q_i, p_i) \right) = E_i^t \left(1 - \frac{\Delta t}{2} R_i(q_i, p_i) \right) + \frac{1}{\bar{\rho}} \left(F_{e_{i+1}}^m - F_{e_i}^m \right) \quad (3.21)$$

with $\bar{\rho}$ being the mean density over the timestep, $F_{e_{i+1}}^m$ the energy flux into the bin and $F_{e_i}^m$ the energy flux out of the bin.

3.6. Fluxes Between Momentum Bins

Following Miniati (2001) we can identify the first term of the integral by parts as the time averaged fluxes over one bin boundary as

$$F_{n_i}^m = \int_t^{t+\Delta t} dt' \left[\frac{1}{3} \frac{\partial u}{\partial x} p + b_l(p) \right] 4\pi p^2 f(t', p) |_{p_i} \quad (3.22)$$

$$F_{e_i}^m = \int_t^{t+\Delta t} dt' \left[\frac{1}{3} \frac{\partial u}{\partial x} p + b_l(p) \right] 4\pi c p^3 f(t', p) |_{p_i} \quad (3.23)$$

This is a consequence of our fixed momentum boundaries. A particle of momentum p_u gains, or loses some momentum over a timestep Δt and arrives at momentum p_i . Since we use fixed momentum boundaries we cannot move those boundaries to account for this change and instead need to calculate a flux over the momentum boundary into a higher, or lower bin. This becomes more intuitive if we consider the definition of our momentum changes

$$\frac{dp}{dt} = -\frac{1}{3} \frac{\partial u}{\partial x} p - b_l(p). \quad (3.24)$$

Substituting dt' in Eq. 3.23 with

$$dt = \frac{dp}{-\frac{1}{3} \frac{\partial u}{\partial x} p - b_l(p)} \quad (3.25)$$

obtained from Eq. 3.24 gives an equation for the fluxes only dependent on p

$$F_{m_i}^m = - \int_{p_u}^{p_i} dp 4\pi p^2 f^m(p) \quad (3.26)$$

$$F_{e_i}^m = - \int_{p_u}^{p_i} dp 4\pi c p^3 f^m(p) \quad (3.27)$$

with

$$f^m(p) = \begin{cases} f_i \left(\frac{p}{p_i}\right)^{-q_i} & \text{if } p_u > p_i \\ f_{i-1} \left(\frac{p}{p_{i-1}}\right)^{-q_{i-1}} & \text{if } p_u \leq p_i \end{cases} \quad (3.28)$$

and p_u being the momentum a particle needs to have to arrive at momentum p_i after a timestep Δt . To solve this integral we use separation of variables in Eq. 3.24

$$\int_t^{t+\Delta t} dt = \int_{p_u}^{p_i} \frac{dp}{-\frac{1}{3} \frac{\partial u}{\partial x} p - b_l(p)} \quad (3.29)$$

$$\Delta t = \int_{p_u}^{p_i} \frac{dp}{-\frac{1}{3} \frac{\partial u}{\partial x} p - b_l(p)}. \quad (3.30)$$

Knowing Δt as the timestep of our simulation and p_i as the i -th momentum bin we only need to calculate adiabatic changes and radiative losses as described in Sec. 5 and Sec. 6 respectively to find p_u and with that the lower boundary of the flux integral. If the integrals have an analytic solution p_u can be found exactly, if they don't, we need to use approximations for the integrands and solve the integral to some order.

3.7. Spectral Cut

Updating the spectral cut of the distribution function works in a very similar fashion to calculating the values for p_u . We need to find analytic or approximate solutions for the integral in Eq. 3.30. For the cut, instead of p_u we need to solve the resulting equation for p_i , since we are interested in calculating the momentum the particle arrives at after a timestep Δt , if it started out with momentum p_u .

3.8. Slope Update

The distribution function is fully defined by four variables: f_i , q_i , E_i and N_i . If we solve Eqs. 3.13 and 3.15 for f_i we are left with a set of two equations only dependent on three of those variables. As we already discussed how to update E_i and N_i we can equate these two equations and are left with

$$\frac{E_i}{N_i p_{i-1} c} = \frac{3 - q_i \left(\frac{p_i}{p_{i-1}}\right)^{4-q_i} - 1}{4 - q_i \left(\frac{p_i}{p_{i-1}}\right)^{3-q_i} - 1} \quad (3.31)$$

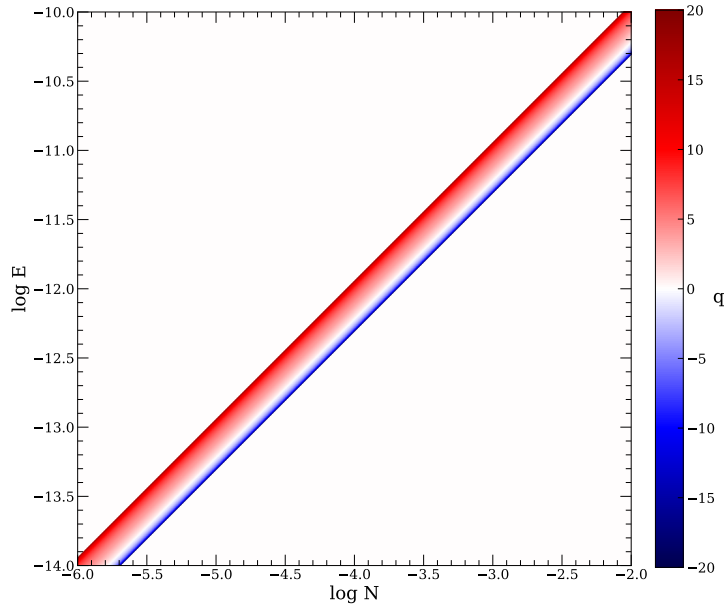


Figure 3.1.: Example parameterspace of the slope.

where f_i canceled out. This equation can be solved numerically for q_i with any suitable root-finding algorithm. Most implementations like Miniati (2001), Winner et al. (2019) and Girichidis et al. (2019) use the Newton-Rhapson method to find the slope q_i . We also tested this method, but decided to use Brent’s method (Brent (2013)) for root finding instead. Unlike the Newton-Rhapson method, Brent’s method does not require solving the derivative of the function as well. In our tests this lead to a convergence about one order of magnitude faster, while also being on average six orders of magnitude more accurate. Since solving the slope is the single most computationally expensive task of our model, this greatly increases the overall performance and especially scaling with the number of momentum bins.

As the parameterspace of the Eq. 3.31 shows (Fig. 3.1), given the right combination of energy- and number density we can find positive and negative slopes, even though the parameterspace for the negative slopes is slightly smaller. This means that we can model any shape of the distribution function as long as our functional form of energy- and number density losses, gains and fluxes are correct. Especially for loss effects that cool the lower part of the spectrum this is of grave importance.

3.9. Distribution Function Update

With all other variables updated we can finally update the normalization of distribution function. This can in principle be done by solving either of Eq. 3.13 or 3.15 for f_i . In practice it is slightly cheaper to solve Eq. 3.13 so that the new normalisation of bin i can

be computed from

$$f_i = \frac{\rho N_i}{4\pi p_i^3} \frac{3 - q_i}{\left(\frac{p_{i+1}}{p_i}\right)^{3-q_i} - 1} \quad (3.32)$$

Ideally one could also solve both Eqs. and construct an interpolation scheme between the two to reduce errors. This could be tested for potential benefits in future work.

4. Sources

Before we can treat the effects that change the distribution function, we of course first need to get our initial distribution function in the first place. For the purpose of this work we only handle injection at shock. Sec. 4.1 will introduce an injection model at resolved shocks, while Sec. 4.2 will introduce a simple sub-grid model that models CR injection at supernova shocks, which can't be resolved in cosmological simulations.

4.1. Shock Injection

As discussed in Sec. 1.3 a main source of CRs in galaxy clusters is particle acceleration at shocks. For that we need to assume that shock energy is transferred into CR energy with some efficiency η . In our model we use an efficiency following Ryu et al. (2003)

$$\eta = \frac{E_{CR,2} u_2}{0.5 \rho_1 u_{sh}^3} \quad (4.1)$$

which leads to a CR energy density in the postshock region defined as

$$e_{CR,2} = \eta \frac{1}{2} u_{sh}^3. \quad (4.2)$$

Additionally, as the shocks in our simulation are broadened by the kernel we need to make sure that the energy is distributed over the total size of the shock and the integral of the shock energy is conserved. To do this we divide Eq. 4.2 by the fraction of the kernel width a particle sees per timestep

$$e_{CR,2} = \eta \frac{1}{2} u_{sh}^3 \left(\frac{2h_{hsm1}}{\Delta t} \right)^{-1}. \quad (4.3)$$

This energy will then be injected into the CR model and subtracted from the internal energy/entropy of the gas particles.

4.1.1. Efficiency Models

Finding a functional form for η proves difficult and has been attempted by numerous authors. In this work we consider four different models. The first model was proposed by Kang et al. (2007). They find that their previous results from Kang and Jones (2007),

where they used the **CRASH** code to solve the diffusion-convection equation at shocks and study the impact of the CR component, are best fit by Eq. 4.4 and Eq. 4.5.

$$\eta(M) = \begin{cases} 1.96 \cdot 10^{-3}(M^2 - 1) & \text{for } M \leq 2.0 \\ \sum_{n=0}^4 b_n \frac{(M-1)^n}{M^4} & \text{for } M > 2.0 \end{cases} \quad (4.4)$$

$$\eta(M) = \sum_{n=0}^4 b_n \frac{(M-1)^n}{M^4} \quad (4.5)$$

Eq. 4.4 describes the efficiency of Cosmic Ray acceleration at pure gas shocks, while Eq. 4.5 describes the efficiency at shocks with a pre-existing (fossil) CR component in the downstream region. This is usually referred to as re-acceleration.

The parameters b_i are given as

$$b_0 = 5.46, \quad b_1 = -9.78, \quad b_2 = 4.17, \quad b_3 = -0.334, \quad b_4 = 0.57 \quad (4.6)$$

for initial acceleration and

$$b_0 = 0.24, \quad b_1 = -1.56, \quad b_2 = 2.8, \quad b_3 = 0.512, \quad b_4 = 0.557 \quad (4.7)$$

for re-acceleration. This model assumes that any supersonic shock is able to accelerate particles and has a very high saturation value of about 57% of the shock energy transferred into CRs. Eq. 4.5 proves to be a useful fitting formula for most of the models under consideration here and is therefore used wherever applicable.

The second model was proposed by Kang and Ryu (2013) and corrects the previous maximum efficiency down to around 21%, while also assuming that every supersonic shock can accelerate particles. While the authors don't provide the values for their fitting functions like in the previous work, we find that their values for initial acceleration are well approximated by

$$\eta(M) = \begin{cases} 1.8803 \cdot 10^{-5} \cdot M^{5.3341} - 0.0006 & \text{for } M \leq 5.0 \\ \sum_{n=0}^4 b_n \frac{(M-1)^n}{M^4} & \text{for } 5 < M \leq 15 \\ 0.21152 & \text{for } M > 15 \end{cases} \quad (4.8)$$

with

$$b_0 = -2.87, \quad b_1 = 9.6676, \quad b_2 = -8.8771, \quad b_3 = 1.9384, \quad b_4 = 0.1806. \quad (4.9)$$

The efficiency of reacceleration is well described by fitting with Eq. 4.5 using

$$b_0 = -0.722, \quad b_1 = 2.7307, \quad b_2 = -3.2854, \quad b_3 = 1.3428, \quad b_4 = 0.1901. \quad (4.10)$$

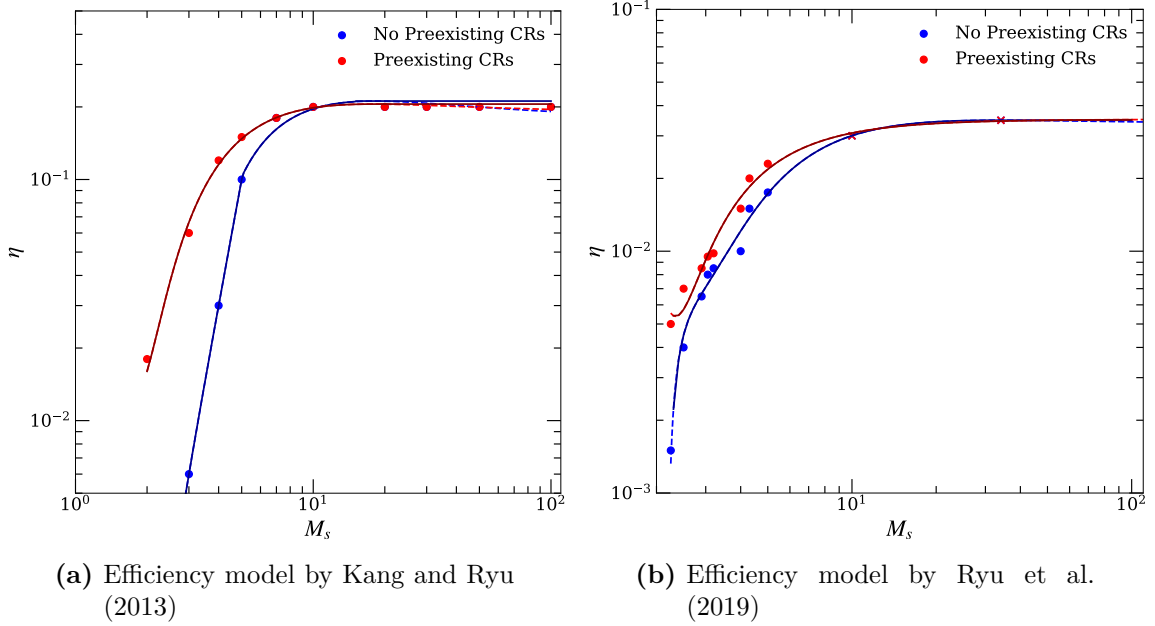


Figure 4.1.: Example for the modelling of the efficiency functions. Points correspond to the datapoints provided by the respective authors and lines show the fit.

To avoid a decrease in efficiency at high Mach numbers that would follow from the pure fitting formula we set the reacceleration efficiency to be constant if $M > 17.8$ at $\eta(M) = 0.2055$. A plot of the discussed fit can be seen in Fig. 4.1 (a). The points represent the data from the publication while lines show the fit.

A third model was proposed by Caprioli and Spitkovsky (2014). They use particle in cell (PIC) simulations where electrons are modelled as a fluid and the equations of motion are solved from the full Maxwell equations for test particles. In the case of their work these test particles are protons and light ions. They perform a series of simulations where they shoot the electron fluid/ion mix at a reflective wall with varying inflow velocities. As the fluid and particles hit the wall and reflect they develop a shock front that slowly moves against the inflow. With that they can model shock properties from first principles and make assumptions about injection efficiency and slope of the resulting power spectrum. Due to the expensive simulations and their focus more on shock geometry, which will be discussed in Sec. 4.1.3, they don't provide enough datapoints to fit a functional form of η to their data. For the purpose of this work we take the same approach as Vazza et al. (2016) and simply consider the Caprioli and Spitkovsky (2014) efficiency to be half the one from Kang and Ryu (2013)

$$\eta(M)_{\text{CS14}} = 0.5 \cdot \eta(M)_{\text{KR13}} \quad . \quad (4.11)$$

Note that we only use the 0.5 factor from Vazza et al. (2016), not the 0.15 they propose in total. This is due to their statistical treatment of shock obliquity. They make an

additional assumption that only 0.3 of shocks have a shock obliquity with less than 45° and only those shocks are able to accelerate CRs. Since we can trace the angle between shock normal and B-field self-consistently (see 4.1.3 for more details) we are not limited to these assumptions.

The last model we consider is the most recent one at the time of this work, by Ryu et al. (2019), who also model acceleration of individual particles with PIC simulations. They also don't provide a fitting formula and only focus on the range $2.25 \leq M < 5.0$. For the minimum Mach number of 2.25 they emphasise the argument by Ha et al. (2018) that only shocks with a Mach number above 2.25 are able to sufficiently accelerate particles. To get a functional form for the larger Mach numbers as well we extrapolated their values to match the overall shape of the functional form. The datapoints and fits can be seen in Fig. 4.1 (b), where points correspond to datapoints from the publication, crosses to extrapolated values and lines to the fits. While we acknowledge that these extrapolations are fairly arbitrary we argue that they are motivated by mimicking the shape of the Kang and Ryu (2013) results, albeit being shifted down one order of magnitude. Both curves for initial acceleration and reacceleration are well approximated by Eq. 4.5 with parameters

$$b_0 = -1.5255, \quad b_1 = 2.4026, \quad b_2 = -1.2534, \quad b_3 = 0.2215, \quad b_4 = 0.0336 \quad (4.12)$$

for initial acceleration and

$$b_0 = 0.3965, \quad b_1 = -0.21898, \quad b_2 = -0.2074, \quad b_3 = 0.1319, \quad b_4 = 0.0351 \quad (4.13)$$

for reacceleration. Fig. 4.2 shows a comparison of all the DSA models introduced in this chapter. We can see a clear trend of correcting the models to lower and lower efficiency over time.

For this work we will use the model by Ryu et al. (2019), as it is the most recent and shows in comparison more efficient acceleration at low Mach number shocks, which are found in galaxy clusters (see van Weeren et al. (2019) and references therein). It also matches observational constraints indicating that the ratio of CR to thermal energy is $\leq 10\%$ (see Brunetti et al. (2017); van Weeren et al. (2019)).

4.1.2. Shocktube Tests for $\eta(M)$

We tested the accuracy of our injection mechanism by performing a series of shocktube tests with target Mach numbers ranging from 3 to 100. To be able to compare to an analytic solution we modified the suggested exact Riemann solver by Pfrommer et al. (2016) to be able to use Mach number dependent acceleration efficiencies. In order to ensure numerical convergence we needed to add an additional layer to the Riemann solver, as the Pfrommer et al. (2016) solution is not numerically stable. Because of how their solution is formulated with the incomplete β -function one can't simply use any root finding algorithm to find the post-shock density, as the incomplete β -function is not defined for two negative arguments. To find the post-shock density and with that the compression ratio at the shock which is needed for the rest of the post-shock properties a good first guess for the compression ratio needs to be supplied in order to lie within the narrow range of

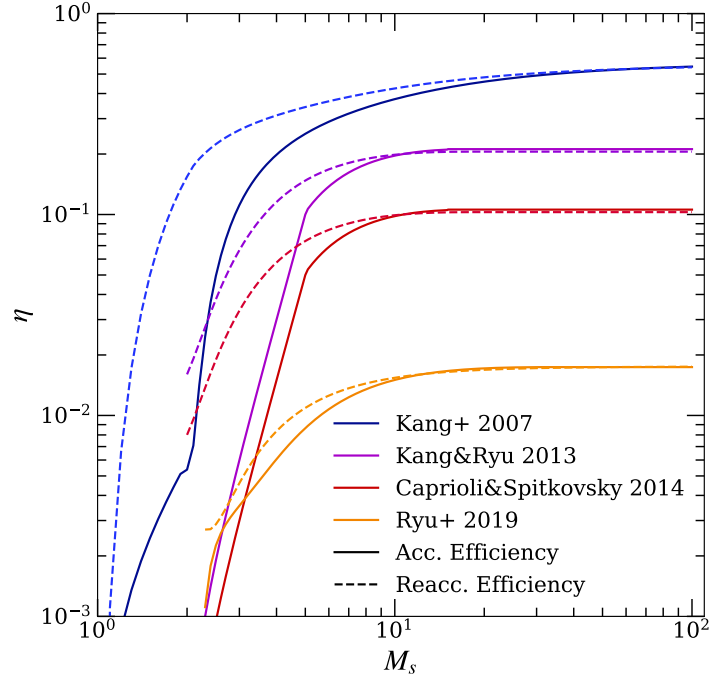


Figure 4.2.: Comparison of all implemented DSA models.

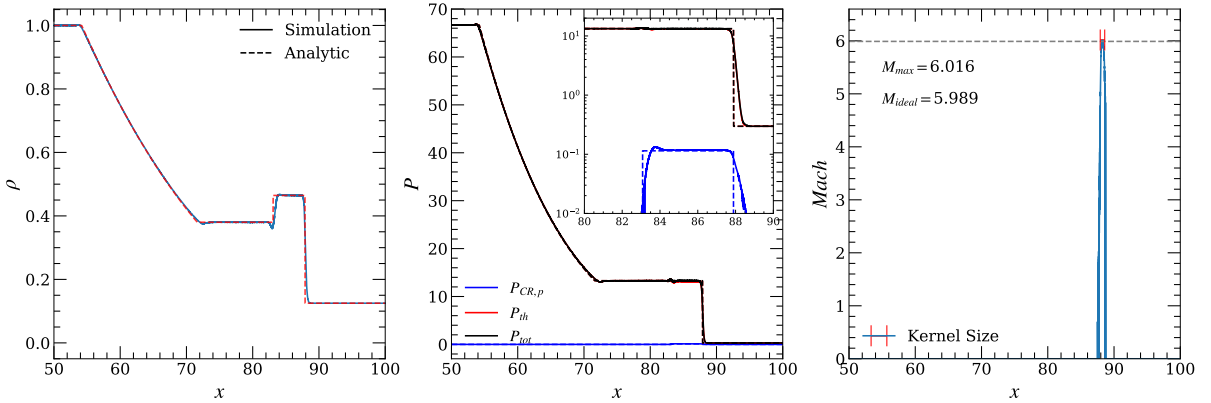


Figure 4.3.: Result of a Mach 6 shocktube test with the Ryu et al. (2019) efficiency model. Dashed lines show the analytic solution, solid lines the result of the simulation. Every particle is plotted.

values that can converge to the actual solution. We solved this with a brute-force attempt by iterating over a set of first guess options and checking which iteration did not result in an error from the incomplete β -function. Furthermore we extended their analytic solution to also account for shock obliquity which will be discussed in Sec. 4.1.3.

Fig. 4.3 shows the result of a shocktube that would result in a Mach 6 shock in the case without CR acceleration. Dashed lines indicate the analytic solution for the Ryu et al. (2019) efficiency model and solid lines are the result of the simulation. We plot every par-

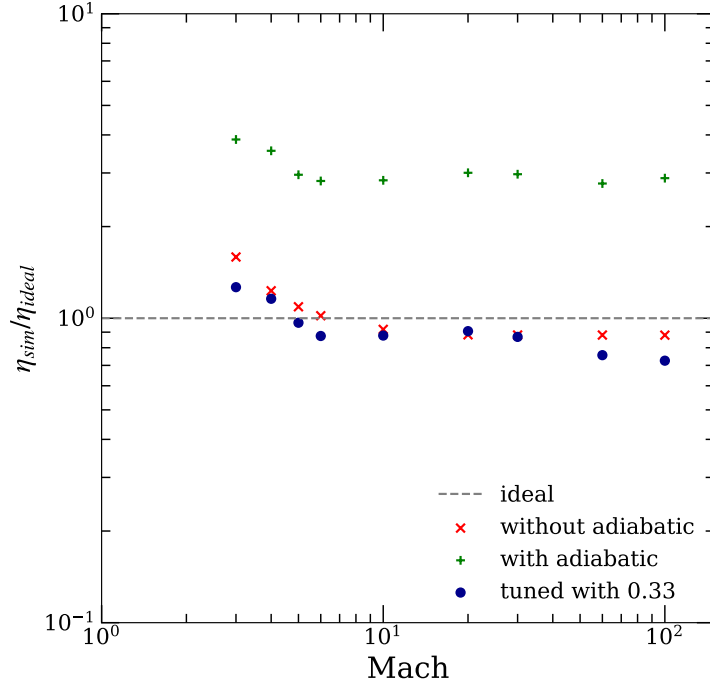


Figure 4.4.: Result of all shocktubes with Ryu et al. (2019) efficiency. Shown are the ratios of the resulting CR energy in the post shock region divided by the ideal energy obtained via our modification of the Riemann solver for CR acceleration proposed by Pfrommer et al. (2016).

ticle to include numerical noise. The simulation was run without allowing for adiabatic changes in the CRs to only focus on the accuracy of our shock injection efficiency. From left to right we show density, pressure, with an additional inset plot to show the logarithm of the pressure, and Mach number. Overall all plots show very good agreement with the analytic solution. The density shows excellent agreement with the analytic solution, except for the typical artifacts of SPH, like the density blip at the contact discontinuity and a smoothing out of the shock. The pressure also shows excellent agreement with the predicted solution. This is especially evident when looking at the logarithm of the pressure in the inset plot. Here the most important part of the result is the blue line which indicates the CR pressure component and therefore the injected CRs. As can be seen the result is in nearly perfect agreement and in large parts of the post shock region the error is below the level of numerical noise. Contrary to Pfrommer et al. (2016) we find that the initial blip in CR pressure (at $x \approx 84$) originates from the first few timesteps of the simulation and does not vanish over the rest of the simulation. This is due to inaccuracies in the shock finding algorithm. As the shock develops from the contact discontinuity, the post-shock region is initially smaller than the kernel size. This leads to an error in Mach number estimation as the density jump within the kernel is not the actual jump from pre- to post-shock region, but from pre-shock region to the high density region at the left state. This in turn leads to a miscalculation of the shock speed and with that

too much shock energy being transferred to CR energy.

Finally in the right plot of Fig. 4.3 we show the result of the shock finder. We capture the analytic shock Mach number with an error below one per cent, as in the pure hydrodynamical test cases. We show the mean kernel size of all shocked particles in the red error bars and conclude, together with the nice agreement of the CR pressure component, that our correction from Eq. 4.3 gives a satisfying result.

Taking into account adiabatic compression over the shock leads to an additional problem. If CRs are injected at the accurate rate without adiabatic changes, additional adiabatic compression will lead to an overshooting in post-shock CR energy. Dubois et al. (2019) solve this issue by flagging a cell for CR injection and store the injected energy. They then inject the CR energy into the cell after a number of timesteps to assure that it was fully passed by the shock. As we were not confident in the stability of this concept, especially in more turbulent production runs, we took a different approach. We reran the set of tests with enabled adiabatic changes and checked for the error in the post-shock region. This can be seen in Fig. 4.4. While the runs without adiabatic changes, indicated by the red x, show overall excellent agreement with the analytic solution, except for a slight discrepancy at high and low Mach numbers, we can see a clear offset in the runs with adiabatic changes, indicated by the green +. Conveniently this offset is systematic at roughly a factor of three. We therefore introduced an additional tuning factor to down-tune our shock efficiency by a factor of 0.33. The results of these runs are marked with blue points. While the tuning is again not perfect at very high and low mach numbers it is computationally very cheap and we accept the results as sufficient for the current work. Future work should nonetheless investigate more accurate and physically motivated solutions. We expect this behavior to also depend e.g. on the used kernel and number of neighbors, but a proper parameter study of this would exceed the scope of this work.

To test the stability of our coupling to the hydro solver, as well as the efficiency, we performed the same set of shocktube tests with the efficiency model by Kang and Ryu (2013). Fig. IV.4 shows the results for a sample of shocktubes. As was the case with Fig. 4.3 dashed lines indicate the analytic solution, while solid lines are the results of the simulation with every particle plotted. We find overall excellent agreement with the analytic results, except for the shock finder in the high Mach number shocks. This can be explained by the CR injection at the front of the kernel, so slightly ahead of the actual shock. The effect can be seen in the inset plot in Fig. 4.3. We find the CR component slightly ahead of the actual shock front, due to the broadening of the shock and injection at every timestep. This in turn gives a larger sound speed in the pre-shock region due to Eq. 2.36. Even though we capture the shock speed correctly, which is evident due to the agreement of the CR component with the analytic solution, we underestimate the Mach number. Other than that we can see that the total pressure is conserved and the subtraction of entropy from the gas particles works well. The nice agreement at very high Mach numbers of 60, or 100 is especially encouraging. This indicates that even with a significant CR component our coupling to the hydro solver stays stable and gives accurate results.

4.1.3. Shock Obliquity

The work by e.g. Caprioli and Spitkovsky (2014) shows that CR acceleration efficiency not only depends on the Mach number of the shock, but also on the shock geometry. They perform a (small) parameter study to determine the impact of the angle between shock normal and B-field and find a relatively stable efficiency until $\sim 45^\circ$ and a steep drop in efficiency between $\sim 45^\circ$ and $\sim 60^\circ$. Most recent work (e.g. Vazza et al. (2016)) treats this crude picture as it is and uses a statistical approach to give an additional efficiency parameter, as discussed briefly in 4.1.1. Another frequently used option is to just allow CR injection in a specific angle range, so to switch acceleration on and off.

In this work we take the same approach as Pais et al. (2018) or Dubois et al. (2019) and introduce an additional factor $\eta(\theta_B)$ in our total acceleration efficiency. Pais et al. (2018) use the values by Caprioli and Spitkovsky (2014) to fit a functional form to their data

$$\eta(\theta_B) \simeq \frac{1}{2} \left[\tanh \left(\frac{\theta_{crit} - \theta_B}{\delta} \right) + 1 \right] \quad (4.14)$$

with $\delta = \pi/18$ and $\theta_{crit} = (\pi/4; \pi/3)$. Here $\theta_{crit} = \pi/4$ corresponds to a shock without and $\theta_{crit} = \pi/3$ to a shock with pre-existing CR component, from Caprioli and Spitkovsky (2014) and Caprioli et al. (2018) respectively. These efficiencies were modeled for ions, for which DSA should be most effective at quasi-parallel shock, as discussed in Sec. 1.3.1. For electrons quasi-perpendicular shocks should be the main driver of acceleration, as pointed out by e.g. Guo et al. (2014). We therefore take the simple approach of shifting the efficiency model by 90° for electrons for the purpose of this work.

To check the applicability of this additional efficiency parameter in our model we performed a set of shocktube tests. For this we set up a pressure gradient as in Pfrommer et al. (2016) with $P_L = 63.499$ and $P_R = 0.1$ and a constant injection efficiency of $\eta = 0.5$. This ensures low numerical noise due to independence from the shock finder and high CR fraction in the post-shock region. Also it makes for an easy comparison to the work by Dubois et al. (2019), as they use the same setup. For the initial set of tests we constructed initial conditions as described above and introduced a negligible magnetic field with a magnetic pressure component 10 orders of magnitude below the thermal one. That way we can assure that the shock is not modified by the magnetic field, while still being able to obtain a B-field vector. To avoid an impact of the shock on the magnetic field we switched the magnetic field evolution off by hand. While this is very unphysical, for these tests we are only interested in the performance of our θ_B finding algorithm. To find the angle between shock-normal (\hat{n}_{sh}) and B-field (\vec{B}) we use the cosine similarity. Since we are only interested in the range $0^\circ - 90^\circ$ and know that there is a symmetry at 90° we can obtain the $\cos(\theta_B)$ as

$$\cos(\theta_B) = \left| \frac{\hat{n}_{sh} \cdot \vec{B}}{|\hat{n}_{sh}| |\vec{B}|} \right|. \quad (4.15)$$

The results for the accuracy of our θ_B finding algorithm can be seen in Fig. 4.5. We obtain the target value for θ_B within an error of only a few per cent, with the exception

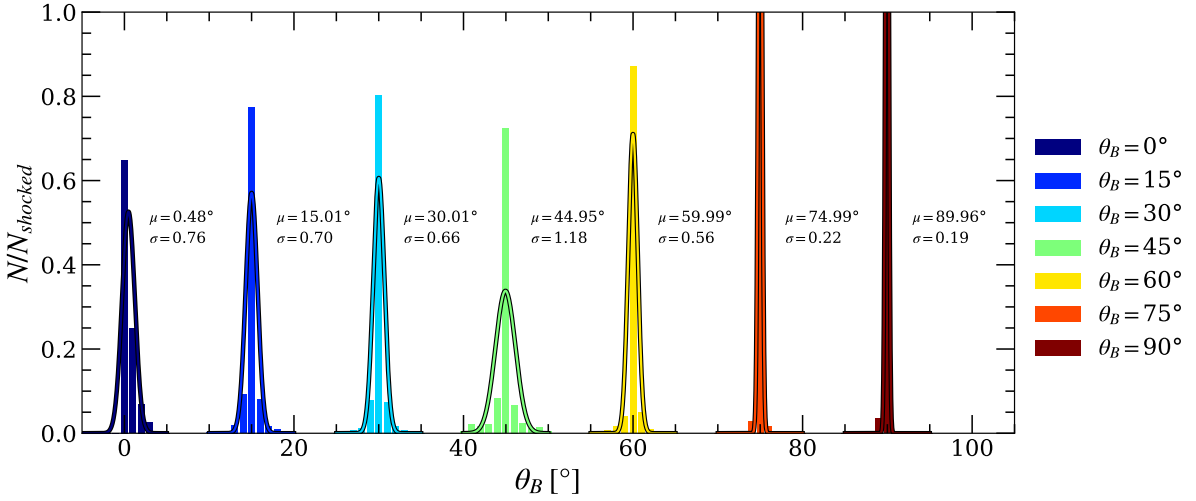


Figure 4.5.: Shown here is the accuracy with which we can capture the angle between the shock-normal and the B-field. The bars correspond to a histogram normalized to the total number of shocked particles. They are binned in 1° bins $\pm 5^\circ$ around the target value for θ_B . The lines show a gaussian fit to the data with the values for mean (μ) and standard deviation (σ) next to the fit.

of $\theta_B = 45^\circ$ where our error is slightly larger. For the 0° case it has to be noted that since we use the absolute value for the cosine, the error to the left of the target angle is artificially folded on top of the error on the right, which increases our total error in mean and standard deviation. Regardless of errors on these cases we can see that in any simulation more than 65% of the shocked particles lie within a one degree interval of our target angle and we therefore conclude that our method is sufficiently accurate.

To further analyze the error in the 45° case we also looked at an individual particle and tracked its values for θ_B and η_B over every timestep of the shock. This is also relevant as our shock is broadened by the kernel and our particles are accelerated over the entirety of the broadened shock and not just at one single timestep. Fig. 4.6 shows the results of these tests. From these results we see that, after an initial swing-in process, we arrive at a very well agreement with the target values. As there seems to be a tendency for our method to overestimate the angle in this swing-in period we loose some energy that should be injected into CRs. Since this swing-in is limited to the first 5% - 10% of the shock we accept this error as it is, without artificial tuning. Finally the left plot of Fig. 4.7 shows our agreement with the ideal values for $\eta(\theta_B)$ and the corresponding L1-Error. Values are normalized to the value at $\theta_B = 0$ to compensate for a systematic offset introduced by not perfectly agreeing with the acceleration efficiency without an additional θ_B . The right plot shows the resulting CR pressure in the post-shock region. This shows the offset already at $\theta_B = 0$ and how it repeats systematically for the different angles. We note that that systematic error is on the level of the numerical noise introduced by the shockfinder and find in general very good agreement with the analytic solution. As in all previous

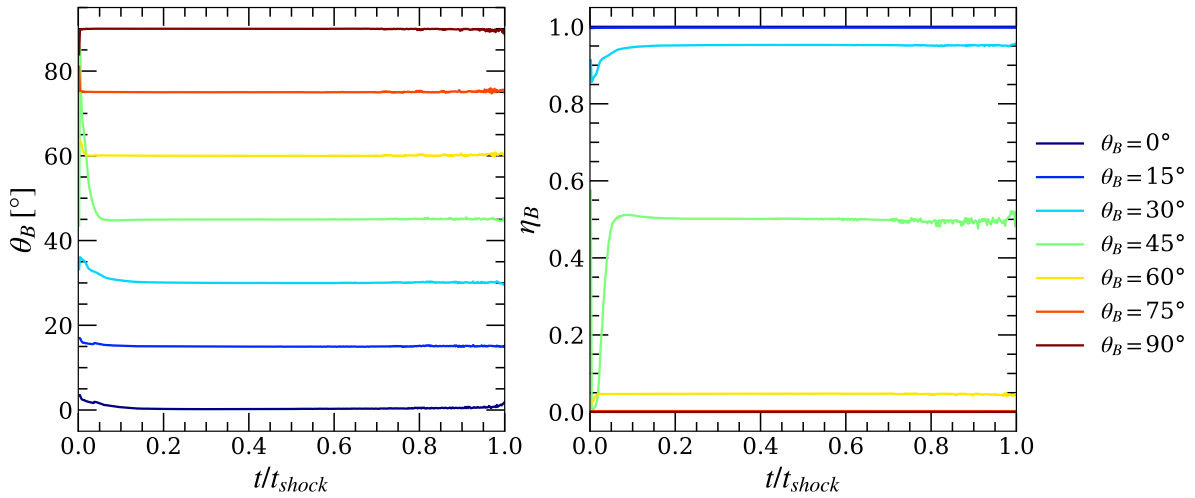


Figure 4.6.: Shock angle and θ_B efficiency a particle experiences over the shock duration with fixed B.

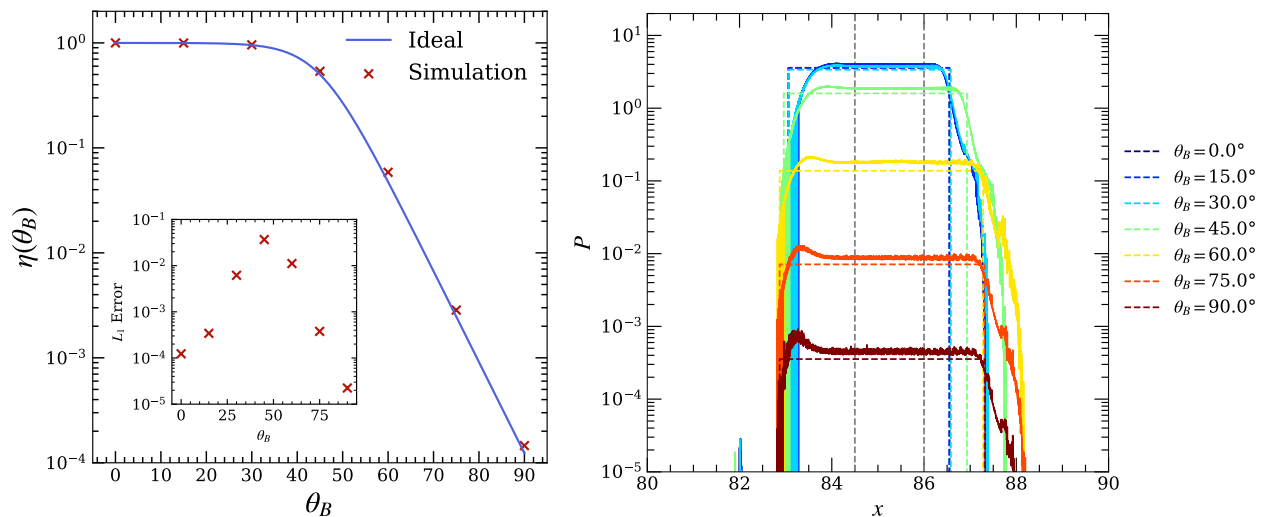


Figure 4.7.: Left: $\eta(\theta_B)$ as a function of θ_B . The simulation values are obtained from the median value of a segment of the post-shock region, indicated with grey dashed vertical lines in the right plot.

Right: CR pressure component in the postshock region. Dashed lines indicate the ideal solution, solid lines the result from the simulations. Colors correspond to the input value of θ_B as in the previous plots.

plots of shocktubes all particles are plotted. In a physical simulation the magnetic field is adiabatically compressed by the shock front. This leads to an alignment of the magnetic field with the shock front and thereby a non-constant η_B over the shock. This result can be seen in Fig. 4.8.

A sufficient analysis of the impact of this effect on CR acceleration is beyond the scope

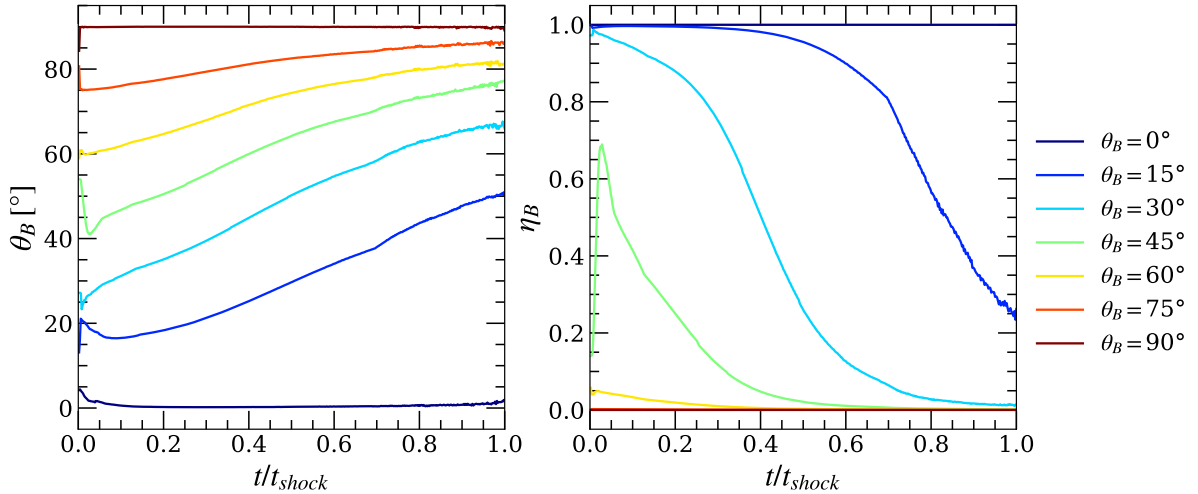


Figure 4.8.: Shock angle and θ_B efficiency a particle experiences over the shock duration with B-field evolution.

of this work. We started first attempts to compare our results to the work by Pais et al. (2018) who examine the impact of CR acceleration on SN blastwaves, but have to revisit this in future work. Ideally we would like to extend on their idealized work by using a realistic ISM from Steinwandel et al. (2019b). This would allow us to study SN bubble expansion into a turbulent ISM while also resolving the magnetic field structure. That way we could model the expected synchrotron emission and compare to observations.

4.1.4. Pre-Existing CR Component

Another efficiency component pointed out by many authors (eg. Kang et al. (2007, 2014); Caprioli et al. (2018); Dubois et al. (2019)) is a preexisting component of CRs. They find that re-acceleration of fossil particles is more efficient than initial acceleration and provide re-acceleration efficiencies obtained with some pre-existing CR to thermal pressure ratio $X_{CR} \equiv P_{cr}/P_{th}$. Dubois et al. (2019) handle this component by combining it with the Mach number dependent acceleration to a factor $\xi(M, X_{CR})$ and even extrapolate the behavior for very large values of X_{cr} .

We take a simpler approach, like Vazza et al. (2012), by using the values for X_{CR} given for the re-acceleration efficiencies by the previously discussed authors. We then linearly interpolate the efficiency between the one with and without preexisting CRs. The interpolation is weighted with the ratio of the value for X_{CR} from the simulation and the value the efficiency models were using. This is for Kang et al. (2007) $X_{CR} = 0.3$ and the others $X_{CR} = 0.05$. Of course this does not account for changed efficiencies at larger values of X_{CR} , so it can be improved in future work.

To test the re-acceleration we performed the same set of shocktube tests as discussed in Sec. 4.1.2 with the efficiency model by Kang and Ryu (2013) and a pre-existing CR component of $X_{CR} = 0.05$. While Pfrommer et al. (2016) also provide an analytic solution

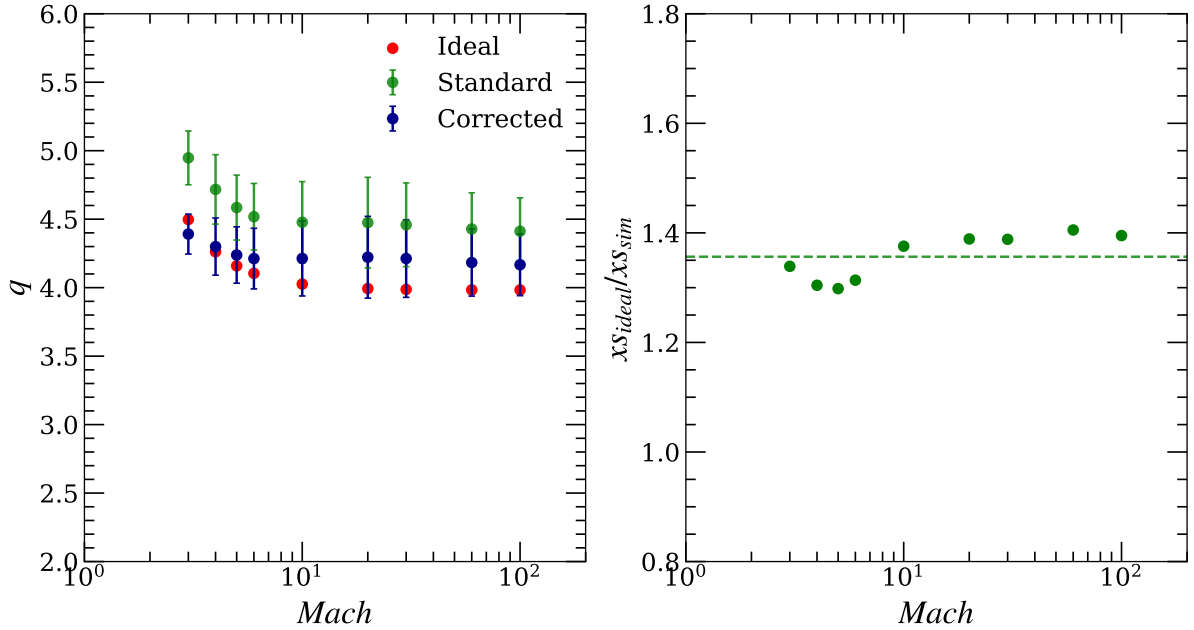


Figure 4.9.: Left: Measured and ideal slopes of the resulting power spectrum. Right: relative error of the compression ratio in the simulation and the ideal solution.

for shocks with a pre-existing CR component and re-acceleration, we found the proposed solution too unstable. We therefore are not able to compare our results to an analytic solution, but will nonetheless analyze the general behavior. Fig. IV.5 shows the results of our shocktube tests. We can see that the total pressure stays stable even for very strong shocks. For the shocks with a Mach number smaller than 30 we find excellent agreement between the measured and theoretical Mach number, which shows that our modification for Eq. 2.36 works. For larger Mach numbers this starts to deviate, but we attribute that to the same effect of premature acceleration as discussed before.

4.1.5. Slope of the Injected Spectrum

Like in Miniati (2001) we use the derivation from Drury (1983) presented in Sec. 1.3.1 to obtain the slope of the resulting powerlaw in the post-shock region from the shock compression x_s

$$q = \frac{3x_s}{x_s - 1} \quad . \quad (4.16)$$

Since our shock is broadened by the kernel it is not necessarily given that we reconstruct the correct compression ratio. In fact the data from shocktubes (RHS of Fig. 4.9) shows that we systematically underestimate the correct compression ratio by a factor $q_{corr.} \approx 1.3$. This leads to bad agreement with the ideal slopes (LHS of Fig. 4.9). Once we employ the correction factor we can see that the agreement improves and the ideal values lie within the errorbars of the simulated ones.

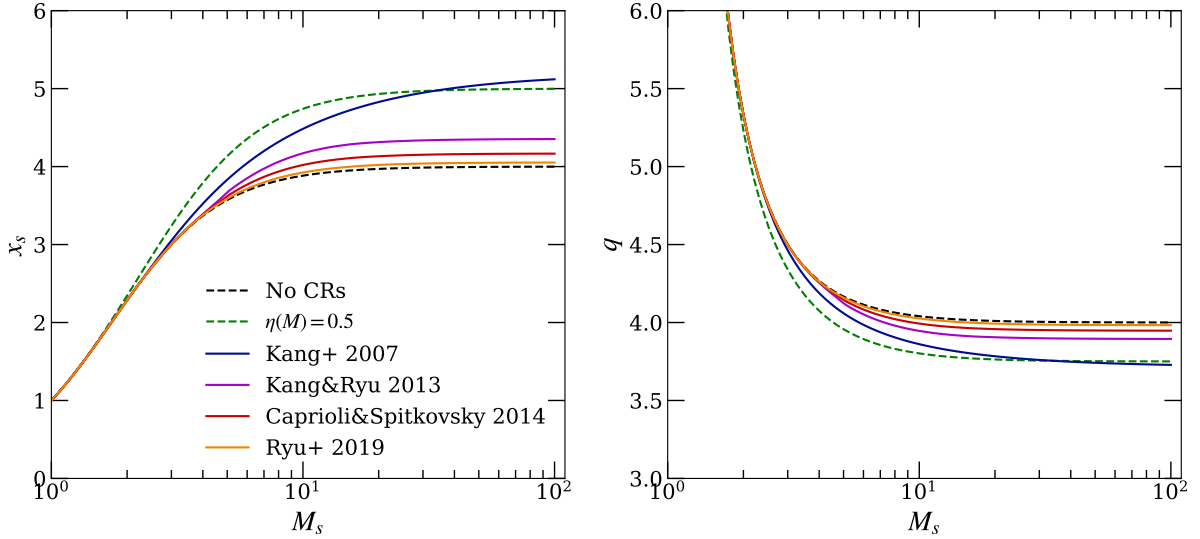


Figure 4.10.: Left: Analytic solution to the compression ratio as a function of Mach number for different efficiency models. Right: Analytic solution to the resulting powerlaw slope from standard DSA.

It has to be noted that there is also a non-linear component to the injection slope of particles accelerated by shocks. The linear model of DSA arrives at a maximum slope of $q = 4$, as it assumes a standard hydrodynamic shock, where the compression ratio of the gas converges to $x_s \approx 4$. Since a polytropic fluid of gas and CRs can be more easily compressed due to the softer EOS of the CR component (see Sec. 1.4) this crude assumption may not be valid any more in regions with significant CR pressure component. Fig. 4.10 shows the effect of CR acceleration with the previously discussed efficiency models on the shock compression ratio and consequently on the injected slope. Multiple authors suggested modifications to the linear treatment of DSA (e.g. Drury (1983), Berezhko and Ellison (1999), Caprioli and Haggerty (2019), Hanusch et al. (2019), Keshet et al. (2019)). As an example we implemented the correction suggested by Caprioli and Haggerty (2019). They argue that the compression ratio in SNR may be as high as 10, which would lead to a spectral slope $q < 4$. Since this contradicts observations, they performed an initial series of PIC simulations to test their hypothesis. They model the slope from first principles and together with the resulting compression ratio arrive at an additional term for the injected slope. This leads to an expression for the non-linear DSA (NLDSA) slope of

$$q_{NLDSA} = q_{DSA} + \frac{3}{x_s + 1} . \quad (4.17)$$

This term is implemented in our model, but it has to be specifically compiled in. Since the goal of this work is to apply the model to galaxy cluster simulations, where the CR component is expected to be on the scale of a few per cent, as mentioned before, we neglect this term at the moment, but keep it as an option for future work.

4.1.6. Cosmic Ray Injection into the Model

Combining the results from the previous sections we can now inject CRs into our model. The total energy to inject can be calculated by inserting the different components for η from Sec. 4.1.1-4.1.4 into Eq. 4.3

$$e_{CR,2} = \eta(M, X_{cr}) \eta(\theta_B) \frac{1}{2} u_{sh}^3 \frac{\Delta t}{2h_{hsml}} \quad . \quad (4.18)$$

This total energy budget needs to be distributed over electrons and protons, following some energy ratio. Unfortunately this ratio is poorly constraint with

$$\frac{E_e}{E_p} \equiv K_{e,p} \sim 0.01 - 0.025 \quad (4.19)$$

following Beck and Krause (2005), or even lower with $K_{e,p} \sim 0.005$ (Spitkovsky, private communication).

With the energy budget calculated and distributed we need to find the distribution function of the newly injected CRs. For this work we assume that the distribution function follows a single powerlaw in momentum space, where the slope q_{inj} of the powerlaw is calculated as described in Sec. 4.1.5. From this assumption we can calculate the value of the distribution function at the lowest bin boundary by inverting Eq. 3.15

$$f_{0,inj} = \frac{\Delta E_{inj}(4 - q_{inj})}{\frac{4\pi c p_{min}^4}{\rho} \left(\left(\frac{p_{max}}{p_{min}} \right)^{4 - q_{inj}} - 1 \right)} \quad (4.20)$$

where p_{min} and p_{max} are the lower and upper boundary of the distribution function as defined in the parameter file. The other normalizations can then be interpolated from the powerlaw shape as

$$f_{i+1} = f_i \left(\frac{p_{i+1}}{p_i} \right)^{-q_{inj}} \quad . \quad (4.21)$$

With the normalisation f_i and slope q_{inj} of every bin calculated we can inject CR number and energy density per bin by solving Eqs. 3.13 and 3.15 respectively. The spectral cutoff of the distribution is either reset to p_{max} if it was below that before the injection or kept as is, if it was above p_{max} . Once the energy and number density of every bin is updated we can update the total distribution function by first solving the slope of the individual bins with Eq. 3.31 and then recalculating the normalisation f_i using Eq. 3.32.

4.2. Supernovae

As a second source mechanism we explored a subgrid model for type II supernovae (SNII), as used in Pfrommer et al. (2016). They model the injection of CR energy per timestep as

$$\Delta E_{CR} = \eta \cdot \text{SFR} \cdot \xi \cdot \Delta t \quad (4.22)$$

where η is the efficiency, or how much energy of the SNII is transferred into CRs, SFR is the star-formation rate, ξ is the canonical SN energy per formed solar mass and Δt is the timestep of the simulation. η has a canonical value of $\eta \approx 0.1$ (Ackermann et al. (2013); Helder et al. (2012); Morlino and Caprioli (2012)) and both SFR and timestep are given by the main code. We used the star formation model proposed by Springel and Hernquist (2003) which uses a density threshold for star formation triggering and a EOS for an ideal gas. ξ is given by the canonical SN energy of $E_{SNII} \approx 10^{51} \text{ erg}$ and by the fraction of formed stars that are above $M_* > 8M_\odot$ and are therefore able to explode as core-collapse SNe. Since we don't form individual stars, due to resolution limitations, but rather deal with stellar populations, this fraction depends on how the stellar populations are sampled. The sampling of stellar populations in `OpenGadget3` is done via the initial mass function (IMF) by Chabrier (2003). This leads to a specific SN energy per solar mass of $\xi = 4 \cdot 10^{48} \frac{\text{erg}}{M_\odot}$.

4.2.1. Injection into the Model

Injection is in principle very similar to shock injection. We obtain the total energy to be injected via Eq. 4.22 and distribute it between electrons and protons according to some predefined energy ratio $R_{e,p}$, typically $R_{e,p} = 0.005$. We use a constant injection slope

$$q_{inj} = 4.3 \quad (4.23)$$

as this is the approximate powerlaw slope observed from galactic CRs (e.g. Drury (1983)). Like was the case with shock injection this constrains all required free parameters. This allows us to compute the norm of the lowest momentum bin via inverting Eq. 3.15 and interpolate the other normalisations via Eq. 4.21. Next steps are again to solve Eqs. 3.13 and 3.15 to obtain the number and energy density to be injected into each bin. The spectral cutoff is reset, if it was below p_{max} and left as it is otherwise. Last we update the slope according to Eq. 3.31 and recalculate the normalisation f_i using Eq. 3.32.

4.2.2. Tests

We tested the implementation by running an isolated galaxy with a realistic hot halo, as described in Steinwandel et al. (2019a). The simulation was run with improved SPH and full MHD with a constant seed-field in x-direction of $B_x = 1nG$. Star formation was simulated using the model by Springel and Hernquist (2003). The CR module used SFR injection, adiabatic changes (see Sec. 5) and radiative losses (Sec. 6). We show an early snapshot of the simulation in Fig. 4.11. The left panel shows density and the right panel magnetic field strength. The contour lines trace synchrotron emission contours calculated from the electron spectra, normalized to the maximum value and spaced out by an order of magnitude in intensity. As we can see, the synchrotron emission, and with that the injected CR electron populations, trace the high density regions. This is of course what we expect, as the high density regions are prone to star formation and the gas particles that contain CRs indeed show high values of star formation. Beyond the first snapshots

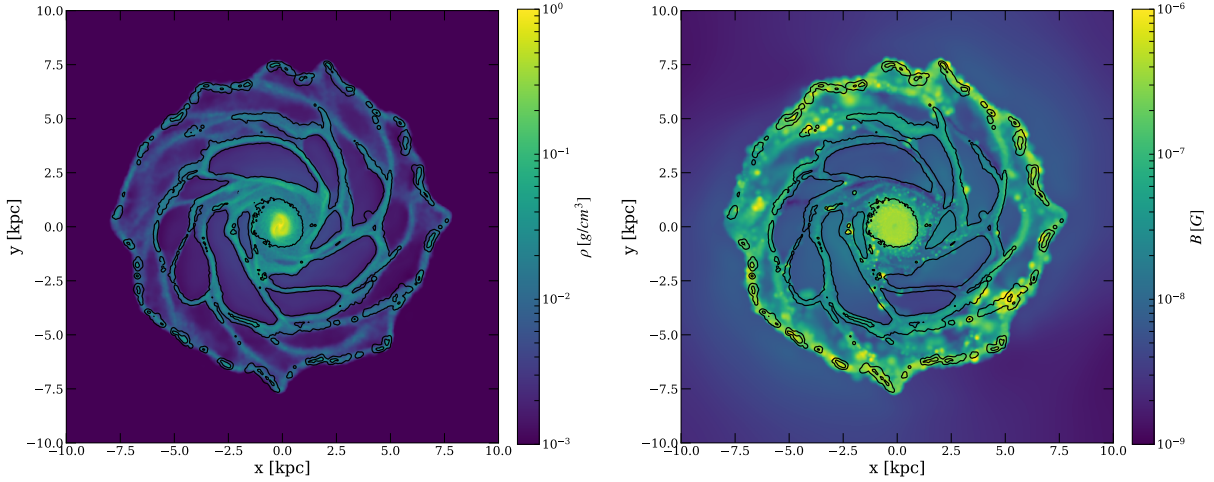


Figure 4.11.: Early snapshot of an isolated galaxy simulation. Left shows gas density, while right shows the magnetic field. Contour lines indicate the modelled synchrotron emission by CR electrons. They are normalized to the maximum emission and spaced out by an order of magnitude in intensity.

we encountered issues as the SFR becomes too large with CR injection, which leads to a feedback loop and eventually a crash of the code. This can be explained via the EOS of the CRs. As they have a more compressible EOS, the pressure support by CRs is weaker. This leads to a further collapse of the gas and higher density. Since the model by Springel and Hernquist (2003) is defined via critical density this leads to more SF and therefore more CR injection.

We postpone this model to later work, where we would like to couple it to the underlying SF model, rather than the resulting SFR, in the same way as the magnetic SN seeding implemented by Beck et al. (2013). Additionally we will need to implement inverse Compton losses for protons and electrons to mediate the kinematic impact of CRs and help avoid the catastrophic feedback loop. On top of that we need to implement a spacial diffusion model to transport the CRs away from the SF regions, which will further reduce the feedback.

5. Adiabatic Changes

As charged particles move through a plasma at relativistic velocities they excite Alfvén waves via the CR streaming instability (e.g. Lerche (1967), Kulsrud and Pearce (1969)). These waves in turn scatter the CRs, which leads to the pitch-angle isotropy discussed in Sec. 3.2 and confines them in the rest-frame of the Alfvén waves (e.g. Skilling (1975) and references therein). If this Alfvén rest-frame (Pfrommer et al. (2016)) is adiabatically compressed a part of the compressive energy is transferred to CRs. On the other hand, if the Alfvén rest-frame expands the CRs will lose energy. Since these processes are self-similar we expect the powerlaw distribution to stay in shape and only shift to higher momenta for compression, or lower momenta for expansion.

For this behavior to be reflected in our model, we need to emphasize the boundary conditions. Naively we can solve the flux integrals and energy change integrals from Sec. 3.6 and Sec. 3.5 respectively. For an adiabatic collapse with a closed lower boundary condition this will preserve the total energy of the CR distribution, as the existing energy is shifted to higher momenta. This leads to a horizontal shift of the distribution function with the lower momentum bins decreasing in energy, since their content is subsequently shifted to the higher momentum bins. The top of Fig. 5.1 illustrates this behavior. As discussed above this would be unphysical. If the Alfvén rest-frame is adiabatically compressed, since no energy exchange with the environment can happen in adiabatic compression, the energy increase is transferred into CRs by accelerating particles at the tail of the Maxwell-Boltzmann distribution to relativistic velocities. This makes them part of our CR population and fills the lower momentum bins, preserving the powerlaw slope in the process. As briefly discussed in Sec. 3.4 and shown in Fig. 5.2 this requires an open lower boundary of our distribution function, which allows for inflow of formerly thermal particles.

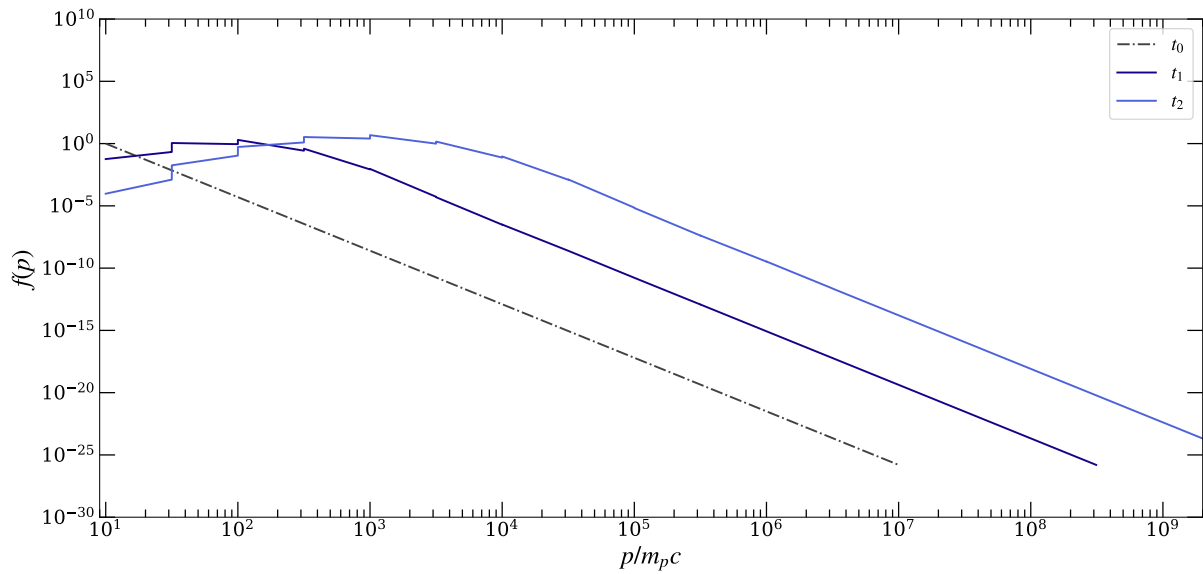
This inflow can be achieved by interpolating the lowest momentum boundary to a "ghost bin" and solving the flux over the lowest boundary

$$p_g = p_0 \cdot 10^{-\Delta p} \quad (5.1)$$

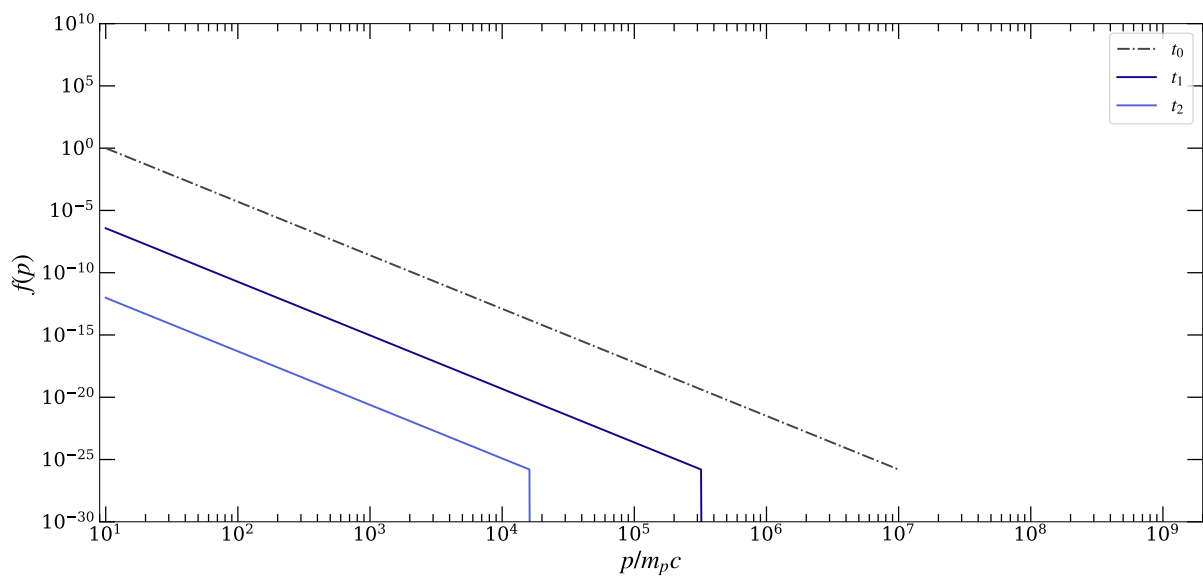
where p_g is the boundary of the ghost bin, p_0 is the boundary lowest bin and Δp is the bin-width of the spectrum. The normalization of the ghost bin can then be interpolated as

$$f_g = f_0 \left(\frac{p_0}{p_g} \right)^{q_0} \quad (5.2)$$

where again f_0 is the norm and q_0 is the slope of the lowest bin.



(a) Adiabatic collapse



(b) Adiabatic expansion

Figure 5.1.: Collapse and expansion test without bin interpolation.

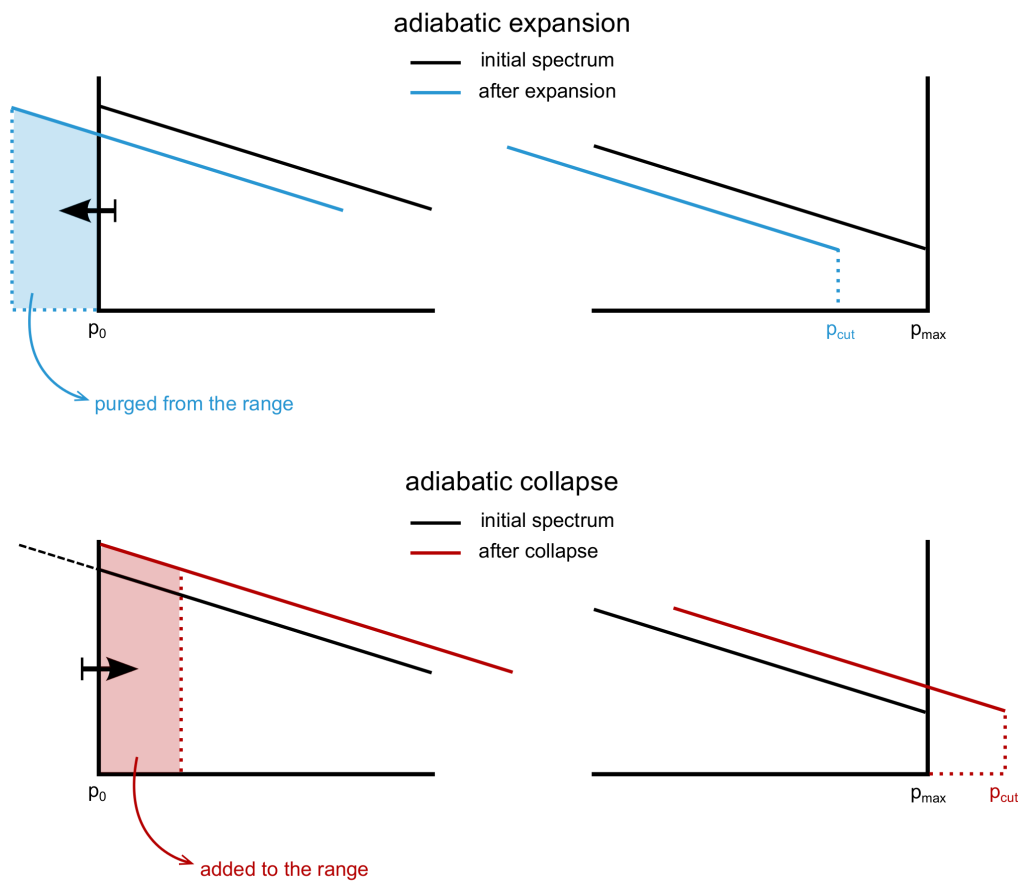


Figure 5.2.: Schematics of fluxes at the boundary conditions. Adopted from Paster-nak (prep).

5.1. Fluxes

To compute the fluxes between momentum bins we first need to find the upper boundary of Eq. 3.30. In a SPH formalism it is easier to deal with actual density changes than velocity divergence, as is the case in Miniati (2001). We can relate the velocity divergence $\frac{\partial u}{\partial x}$ to density changes in SPH as

$$\frac{\rho}{\rho_0} = e^{-\frac{\partial u}{\partial x} \Delta t} \quad (5.3)$$

$$-\frac{\partial u}{\partial x} \Delta t = \ln \left(\frac{\rho}{\rho_0} \right) \quad (5.4)$$

$$-\frac{\partial u}{\partial x} = \frac{\ln \left(\frac{\rho}{\rho_0} \right)}{\Delta t} \quad (5.5)$$

$$-\frac{1}{3} \frac{\partial u}{\partial x} p = \frac{1}{3} \frac{\ln \left(\frac{\rho}{\rho_0} \right)}{\Delta t} p \quad (5.6)$$

This leads to an expression for the momentum change due to adiabatic expansion/compression of

$$\left(\frac{\partial p}{\partial t} \right)_{\text{adiab.}} = -\frac{1}{3} \frac{\partial u}{\partial x} p = -\frac{1}{3} \ln \left(\frac{\rho}{\rho_0} \right) \frac{p}{\Delta t} \quad (5.7)$$

Integrating this by parts, as described in Sec. 3.6, gives

$$\Delta t = \Delta t \ln \left(\frac{\rho}{\rho_0} \right)^{\frac{1}{3}} \int_{p_u}^{p_i} \frac{dp}{p} \quad (5.8)$$

which can be solved for the upper momentum boundary p_u as

$$p_u = p_i \left(\frac{\rho_t}{\rho_{t+\Delta t}} \right)^{1/3} \quad (5.9)$$

This boundary can then be inserted into the flux integrals in Eqs. 3.26 and 3.26 to compute the number- and energy density fluxes between momentum bins.

This of course requires us to store the density of the previous timestep in an additional field of the SPH particle `struct`, as normally the density changes overwrites the original density.

5.2. Spectral Cut Update

Since we also need to trace the spectral cut of the distribution we need to solve Eq. 5.8 for p_i and identify this as the new spectral cutoff, as discussed in Sec. 3.7

$$p_{\text{cut},t+\Delta t} = p_{\text{cut},t} \left(\frac{\rho_{t+\Delta t}}{\rho_t} \right)^{1/3} \quad (5.10)$$

5.3. Energy Changes

As shown in Sec. 3.5 the changes in number density due to adiabatic changes only depend on the fluxes between momentum bins

$$N_i^{t+\Delta t} = N_i^t + \frac{1}{\bar{\rho}} \left(F_{n_{i+1}}^m - F_{n_i}^m \right) . \quad (5.11)$$

where $\bar{\rho}$ is the mean density over the timestep. For the energy density changes we need to solve

$$E_i^{t+\Delta t} = E_i^t \left(\frac{4}{3} - \frac{1}{3} \frac{\rho_t}{\rho_{t+\Delta t}} \right) + \frac{1}{\bar{\rho}} \left(F_{e_{i+1}}^m - F_{e_i}^m \right) \quad (5.12)$$

which is a modification of 3.21 due to transformation from Eulerian into Lagrangian formalism.

5.4. Standalone Tests

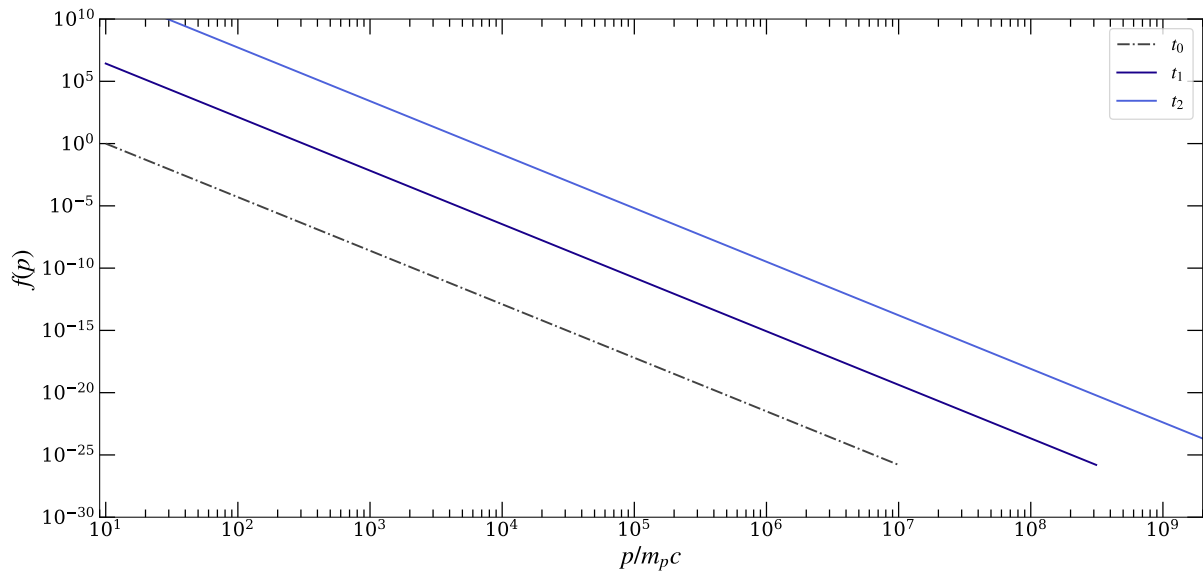
To test the stability of the implementation of adiabatic changes in our model we set up a stand-alone scheme. That way we can avoid the introduction of numerical noise from the hydro-solver and also reduce the computational cost of the tests. The standalone scheme simply calculates a fixed density change and calls the adiabatic changes function with the updated parameters.

For the first set of tests we set up a collapse/expansion model with a fixed velocity divergence

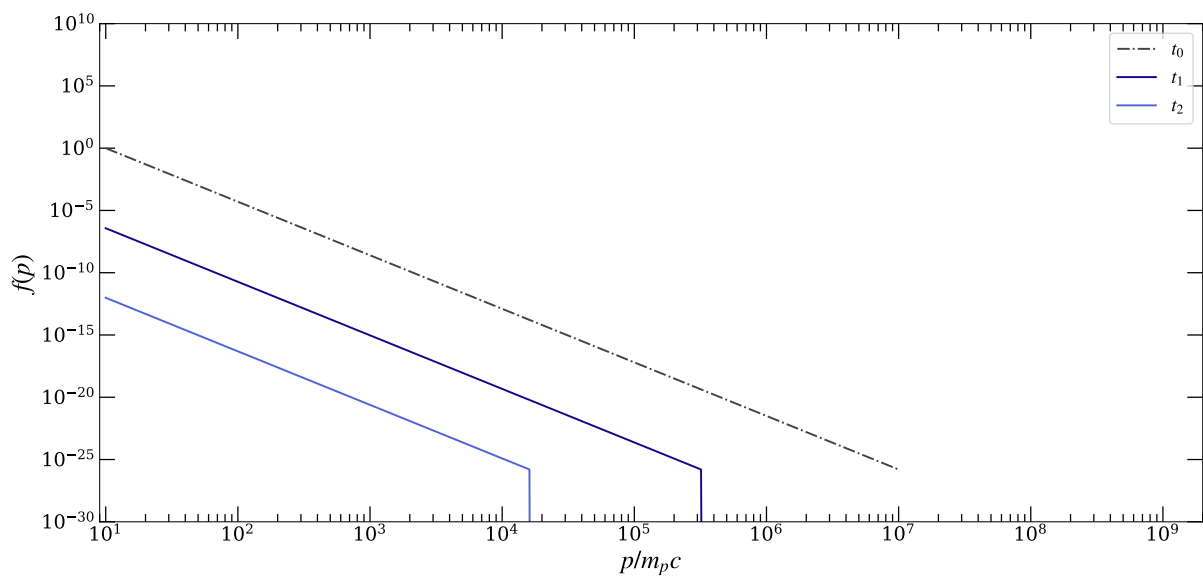
$$\nabla \cdot \vec{v} = \pm 2.3 \cdot 10^{-13} \frac{\text{cm}}{\text{s}} . \quad (5.13)$$

We deliberately chose a low momentum space resolution of only 12 bins to make kinks and errors in the distribution function easily visible. The results of this standalone test can be seen in Fig. 5.3. Here we used the bin interpolation method as previously discussed, as it gives a more physical result. The top plot in Fig. 5.3 shows an adiabatic collapse, while the bottom one shows an adiabatic expansion. As we expect in the case of the collapse the total energy rises and with that the distribution function is shifted to the right. The distribution function itself remains in an excellent powerlaw shape and shows no jumps between bins. Similarly the expansion leads to a left-shift of the distribution function in the bottom plot.

For further detail on the conservation of properties defined by the distribution function, we performed a set of adiabatic "bounce" tests. In these tests we used the same velocity divergence as in the previous tests, but ran a simulation with *collapse - expansion - expansion - collapse* pattern. That way we can compare the values of CR energy, number density and distribution function slope each time the simulation returns to the initial state. The result of this test is shown in Fig. 5.4 for 12 momentum bins on the left and 48 momentum bins on the right. The x-axis gives the momentum bin for which the value is obtained, while the y-axis gives the relative error to the initial value. Colors indicate the errors for distribution function slope, CR energy and CR number density. Solid lines



(a) Adiabatic collapse



(b) Adiabatic expansion

Figure 5.3.: Collapse and expansion test with bin interpolation.

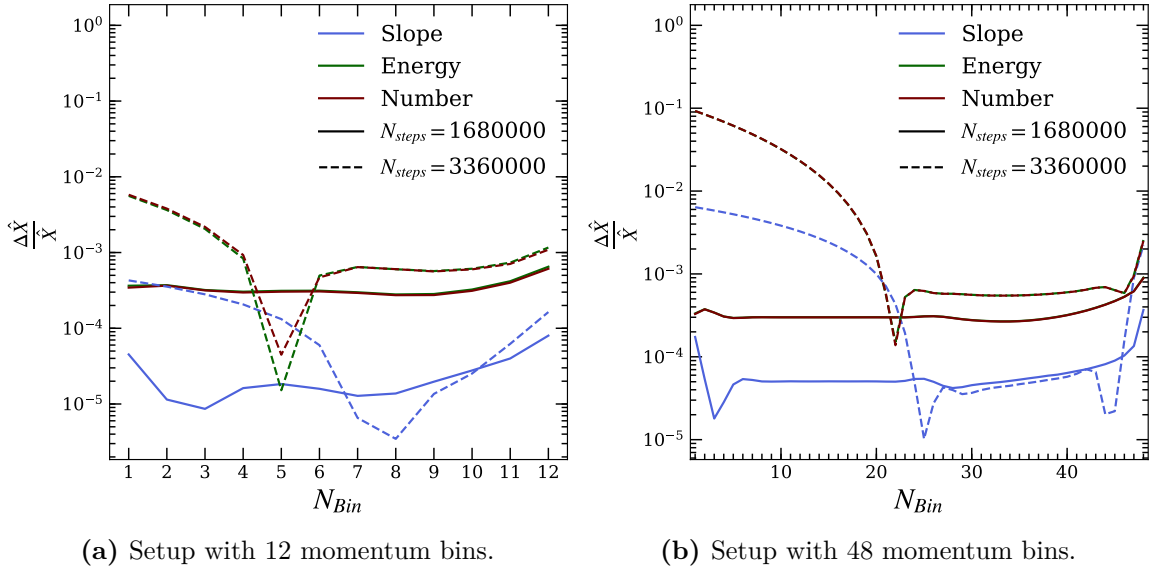


Figure 5.4.: Relative error of the adiabatic bounce test after the collapse phase (solid lines) and after the expansion phase (dashed lines).

refer to the state after *collapse - expansion* and dashed lines to the state after *expansion - collapse*.

For the first half of the simulation these results look very promising in both levels of resolution. Both energy and number density error are only of the order of 10^{-4} and the error for the slope is even smaller by an order of magnitude. It can also be noted that the error is very consistent over all momentum bins and therefore hints towards a slight offset in the distribution function. This is acceptable after almost 1.7 million computation steps.

The second half of the simulation reveals a larger discrepancy from the ideal solution. While the higher momentum bins still agree fairly well with the ideal solution and show errors slightly below 10^{-3} , the lower momentum bins show errors one, to two orders of magnitude larger. This is problematic as especially for distributions with larger slopes the lower bins dominate the contribution to energy and number density of the CRs.

A possible explanation for this behavior is the bin interpolation scheme. The error most likely originates from the second collapse phase. In the second expansion phase the distribution function is shifted to the left of the initial distribution. Physically this means that particles are purged from being in the CR pool and return to the thermal pool. As the second collapse starts the distribution function shifts to the right and high energy thermal particles are accelerated further by scattering off compressing Alfvén waves and become part of the CR pool again. Numerically we need to interpolate the lowest bin to solve the integral for the flux of thermal particles into the lowest bin. A small error in the slope of the lowest bin will then lead to an error in the flux integrals and with that an error in the energy and number density. This will in turn introduce an error in the next slope update and then the error will propagate further.

Even after further investigation we did not find a satisfying solution to this problem yet. We found that the error can be decreased by using a smaller timestep, but the general shape of the introduced error stays the same. We will keep investigating this problem in future work.

5.5. Shocktube Tests

From the first law of thermodynamics we can derive that the pressure change of an ideal gas under adiabatic expansion, or collapse follows

$$P_{cr,d} = P_{cr,u} \left(\frac{\rho_d}{\rho_u} \right)^{\gamma_{cr}} \quad (5.14)$$

where the subscripts u and d refer to the state up- or downstream of the shock.

To test how well this prediction holds we set up a series of shocktube tests with a seed population and no additional CR injection (see Sec. 4.1). The seed population was set up to fulfill $P_{cr,0} = 0.3 P_{th,0}$ on both sides of the initial contact discontinuity. This way we can study the accuracy of our adiabatic changes by comparing the states upstream and downstream of the shock. The results of a shock with Mach 3 and Mach 10 can be seen in Fig. 5.5 and Fig. IV.6, respectively.

For the Mach 3 shock we find that $\frac{\rho_u}{\rho_d} = 3.064$ and $P_{cr,u} = 0.392$. Inserting this in Eq. 5.14 would give the ideal value $P_{cr,d/ideal} = 1.746$. We find $P_{cr,d} = 2.0$ in the postshock region, which means that we overestimate the adiabatic pressure increase roughly by a factor of 15%. In the case of the Mach 10 shock the compression factor is $\frac{\rho_u}{\rho_d} = 3.895$ and the upstream CR pressure is $P_{cr,u} = 0.0315$. This gives the ideal upstream CR pressure $P_{cr,d} = 0.193$. The simulation shows a downstream CR pressure of $P_{cr,d} = 0.225$ and therefore overestimates the post shock pressure again by roughly 15%. To check for consistency of this offset we performed this test for the same set of target Mach numbers as in in Sec. 4.1.2. The results for the numerical values in up- and downstream regime are shown in Tab. 5.1 and a visualisation is given in Fig. IV.7. The plot in Fig. IV.7 shows us that our coupling to the hydro-solver stays stable, even with a significant CR fraction and at very high Mach numbers. The errors, last row in Tab. 5.1, show a consistent offset of roughly 15%. This overestimation can be explained by our choice of boundary conditions for the low momentum boundary. To reiterate, under adiabatic compression we choose to have inflow from the high-energy thermal pool of particles into our CR population. This conserves the powerlaw shape of our function, but of course explicitly does not conserve energy. Instead we have a constant inflow of energy and therefore too much CR pressure in the post-shock region. Seeing as our total pressure is conserved in Fig. IV.7 we can assume that our model works and we in fact take energy from the high energy thermal component.

Mach	3.0	4.0	5.0	6.0	10.0	20.0	30.0	60.0	100.0
$\frac{\rho_u}{\rho_d}$	3.064	3.42	3.61	3.72	3.895	3.973	3.986	3.996	3.996
$P_{cr,u}$	0.3923	0.2087	0.1302	0.08923	0.0315	0.00781	0.003466	0.000866	0.0003116
$P_{cr,d/ideal}$	1.746	1.075	0.721	0.5146	0.193	0.04913	0.02191	0.00549	0.001976
$P_{cr,d/sim}$	2.0	1.248	0.841	0.6	0.2246	0.0569	0.02531	0.006325	0.002275
$\frac{\Delta P_{cr,d}}{P_{cr,d/ideal}}$	0.1455	0.1608	0.1655	0.1665	0.1637	0.1578	0.1554	0.1527	0.1516

Table 5.1.: Values for compression factor, upstream CR pressure, ideal solution and simulation data of the downstream CR pressure and the corresponding error for a set of shocktube tests with Mach numbers ranging from Mach 3 to Mach 100.

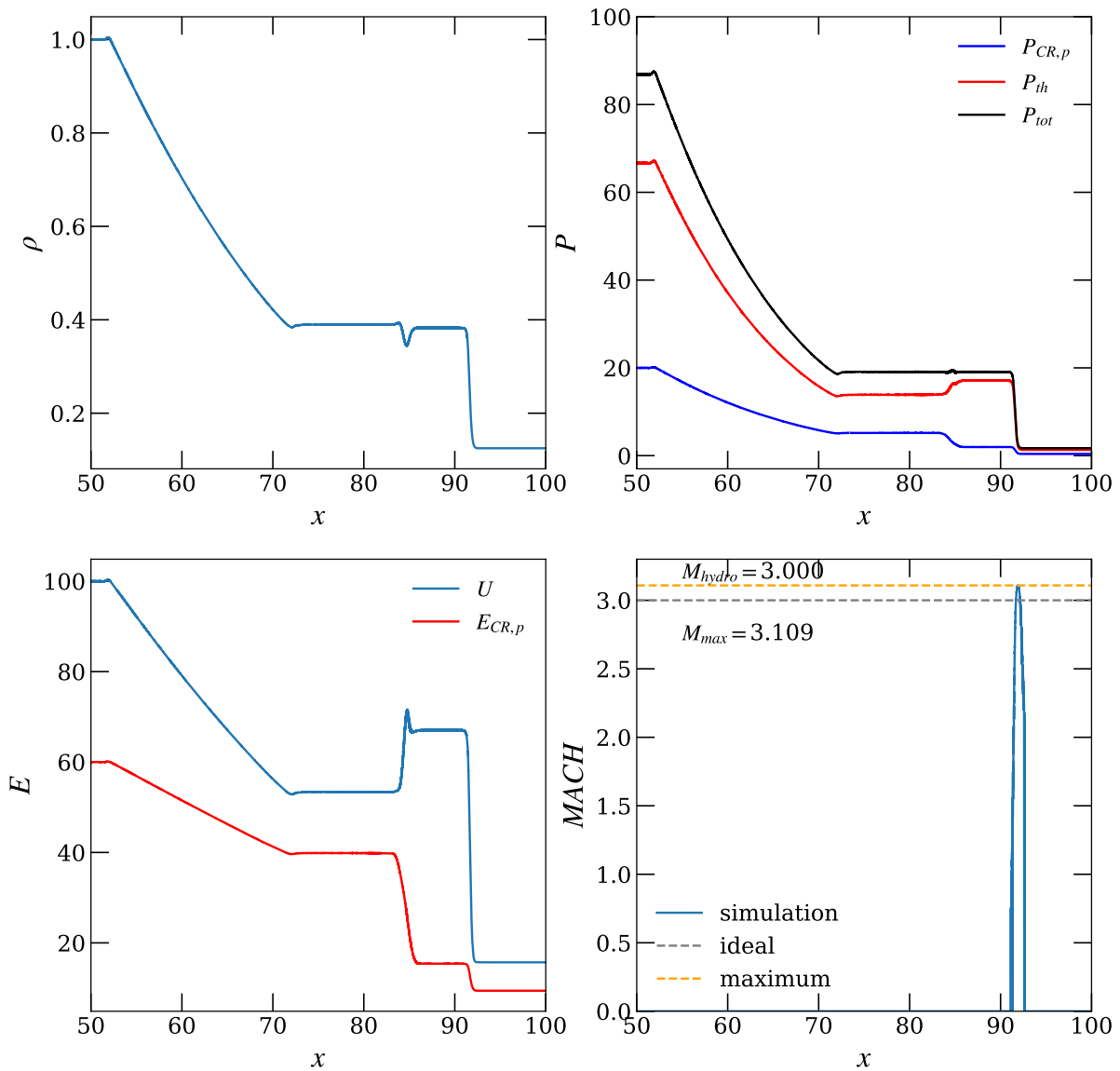


Figure 5.5.: Result of a shocktube test with a seed CR population and $P_{cr} = 0.3 P_{th}$.

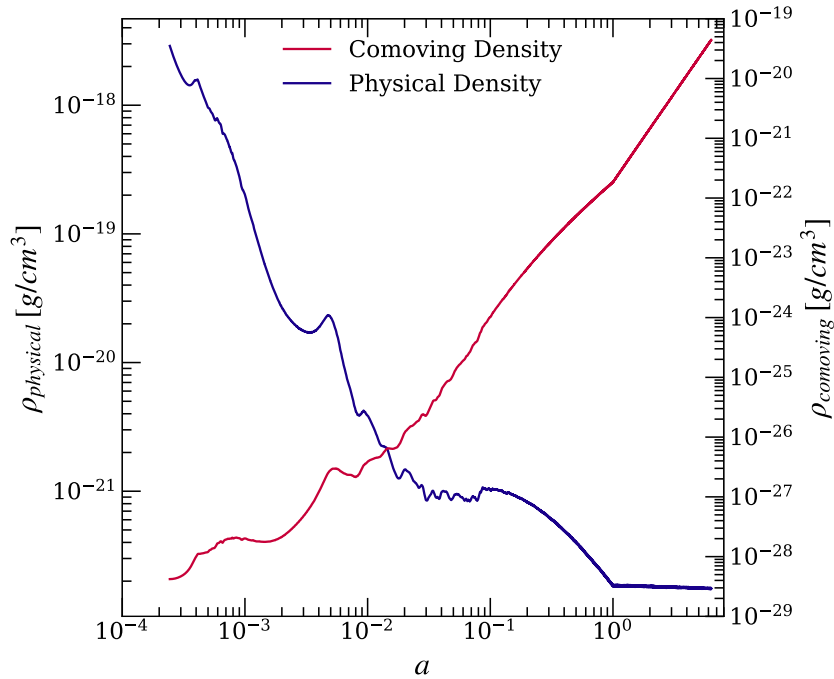


Figure 5.6.: Evolution of the densities as a function of cosmological scale factor. While the comoving density increases (right y-axis) the physical density decreases because of the cosmic expansion.

5.6. Cosmological Tests

As a second physical test we ran a cosmological test suggested by Bertschinger (1985). In this test we set up a large glass file and construct a density inhomogeneity by adding 8 additional particles in a grid in the box center. The box is then evolved with comoving integration and the inhomogeneity will collapse in the comoving frame. The increasing comoving density is shown as the red line with the right y-axis in Fig. 5.6. We plot the density evolution of a single of the perturber particles for every timestep. If we convert the simulation into the physical frame and evaluate the densities via

$$\rho_{phy}(t) = \rho_{comov}(t) \cdot a(t)^{-3} \quad (5.15)$$

where $a(t)$ is the cosmological scale factor, we can see, that in the physical frame the collapse is not fast enough to counter the cosmological expansion and the physical density actually decreases. This is shown as the blue line and the left y-axis in Fig. 5.6. To illustrate the effect on the CR population we show the spectrum of the same perturber particle in the top plot of Fig. 5.8. The test was run with 48 momentum bins, a seed CR population with $P_{cr,0} = 0.05 P_{th,0}$ and only adiabatic changes enabled. We started the simulation at $z = 4096$ and ran it until $z = -0.7$. The spectral evolution shows the expected self-similar shift to lower momenta as the density decreases. The spectral cut update seems to work well, as we don't see any unexpected up-turn of the distribution

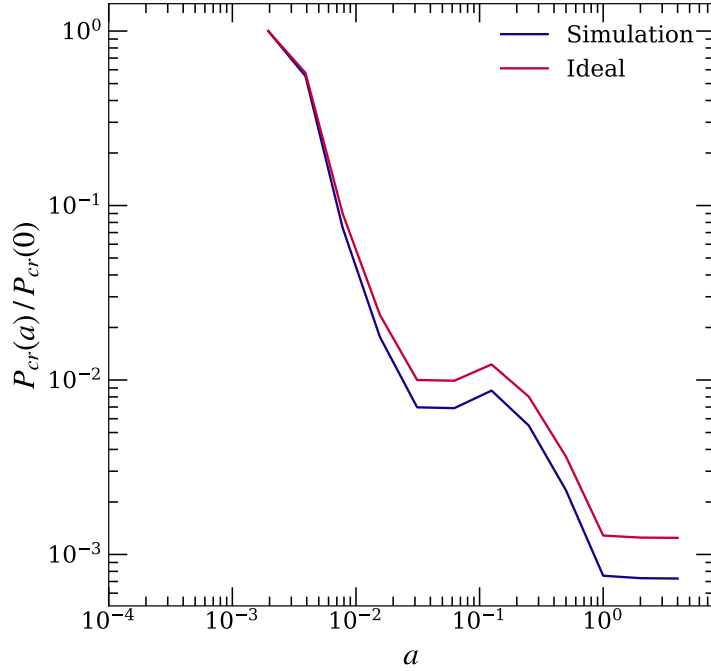


Figure 5.7.: Relative change of pressure under adiabatic expansion.

function in the last populated bin, which would indicate a too low spectral cutoff. The rest of the distribution function also looks promising, as the overall powerlaw shape is conserved over the entire simulation. This becomes even more clear when we look at the distribution function in a different way. In Fig. IV.8 we multiply the spectral norm $f(p)$ by p^{q_0} , where q_0 is the initial powerlaw slope. In this view we expect the distribution function to be a horizontal line with a sharp drop-off at the spectral cut. Indeed we can see that the distribution function follows the expected shape with only some wrinkles where the slope of the bin shows a small error. To further quantify this we analyzed the slope of the individual momentum bins for five perturber particles. We show the time evolution of the median slope of the distribution in the bottom plot of Fig. 5.8. For visualisation reasons we spaced out the particles along the x-axis, they are actually evaluated at the same redshifts. The errorbars indicate the standard deviation of the slopes in each distribution. To avoid artificial contamination of our sample we select only those bins that are at least 5 bins below the spectral cutoff. With a momentum resolution of 48 bins this still gives us a sample of 33 bins for our analysis. As can be seen the slope stays very consistent at $q = 4.3$. The error increases slightly over the course of the simulation, but even in the worst case stays below a 5% scatter. Over the simulation time of 33.07 Gyrs, assuming a flat cosmology with $H_0 = 69 \frac{\text{km}}{\text{s Mpc}}$ and $\Omega = 0.29$, we find this error acceptable. Finally, as in the previous section, we use Eq. 5.14 to compare the intrinsically calculated pressure change with the analytic one. The results of this are shown in Fig. 5.7. We normalized the pressure to the one at redshift $z = 511$ and show the time evolution of the simulation output (blue line) and analytic calculation (red line).

Contrary to the case of the shocktube tests in Sec. 5.5 we find that the pressure is slightly below the analytic solution. This indicates an actual error, instead of only an artifact of our boundary conditions. It would be worth to check if this error gets smaller at higher spectral resolution, or if it is an actual error in the implementation. As the Bertschinger test is quite computationally expensive this resolution study is beyond the scope of this work, but should be revisited at a later time. For the purpose of this work we accept the error as it is, since, like was the case with the slope error, it is quite small considering the total simulation time.

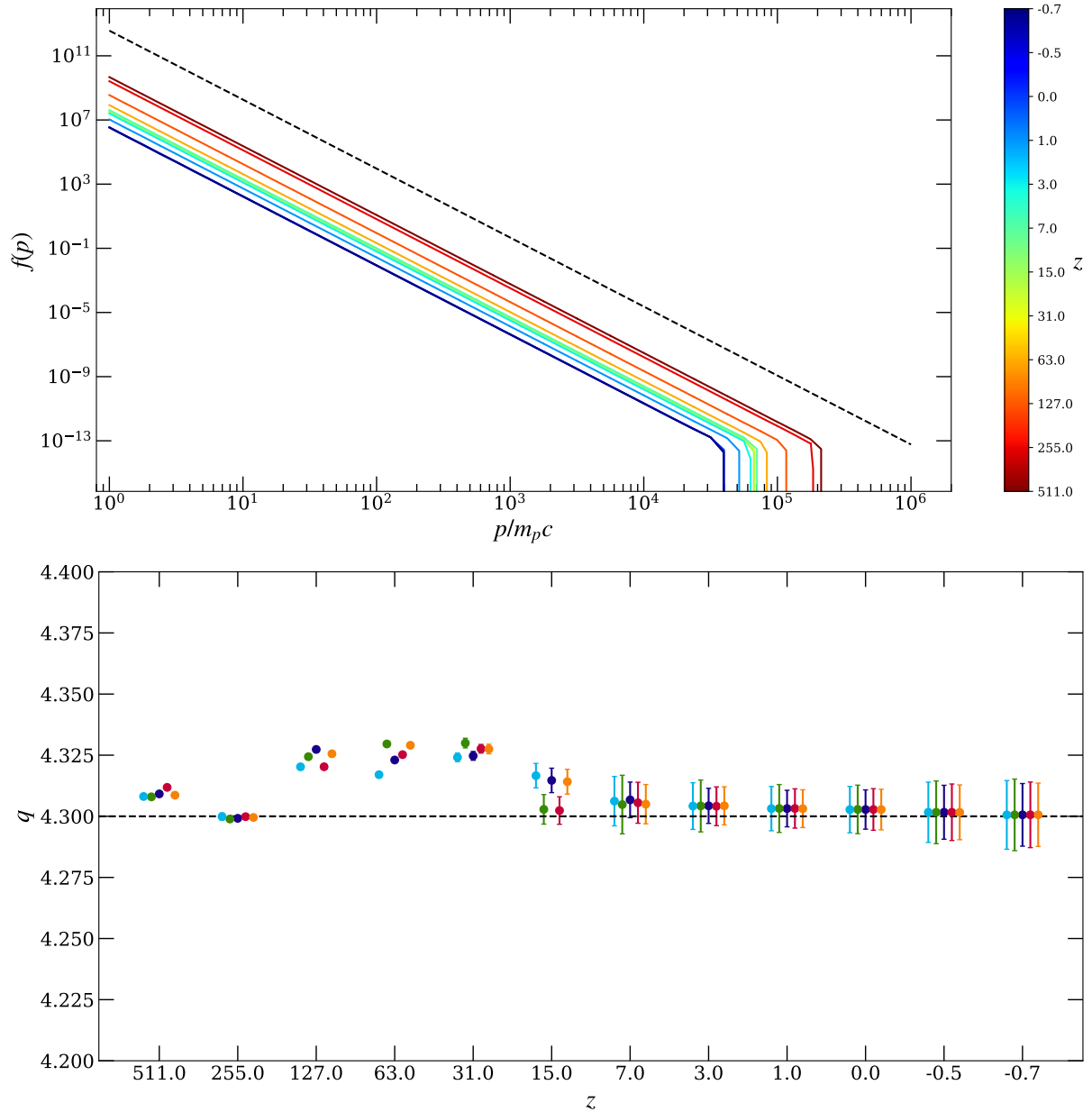


Figure 5.8.: Top: Spectral evolution of the initial distribution (dashed line). As in the non-cosmological case a decrease in density, hence adiabatic expansion, leads to a left-shift of the distribution function. The slope of the bins below the cut-off should remain constant and does so in the simulation. Bottom: Change of the slope of the bins below the cut-off. As can be seen the slope stays nicely constant over the whole simulation.

6. Radiative Changes

As discussed in Sec. 1.5 Cosmic Rays can lose their energy via a multitude of radiative processes. For protons these are dominated by Coulomb losses (Eq. 1.42) and inelastic scattering off background gas (Eq. 1.46). Both these loss functions can only be solved approximately for the upper integration boundary of Eq. 3.30. The solution for this problem needs to be postponed to future work. This is especially important for the Coulomb losses, as the low momentum part of the distribution function dominates the kinetic contribution of the CRs (e.g. Enßlin et al. (2007)). Girichidis et al. (2019) solve the Coulomb losses for their model approximately, but don't provide much insight on how they approximate the function.

For electrons the dominating loss process at the low momentum end is also Coulomb interaction, while the high momentum end is dominated by synchrotron and inverse Compton losses. Similar to the protons, albeit less complex, there is no analytic solution for Coulomb losses of electrons which we can solve for an upper momentum boundary p_u . We tested the implementation for Coulomb losses by Winner et al. (2019) who follow formulation of Gould (1972) and solve the function approximately, but unfortunately this did not work by the time this work was finalized and will therefore be postponed.

For this work we focus on the two loss mechanisms relevant for high energy/momentum electrons, namely synchrotron and inverse Compton losses. Our implementation follows Eq. 1.50 and 1.52 respectively. As was the case with adiabatic changes we will first derive the analytic form for p_u to solve the flux integrals, then the spectral cutoff and finally the analytic form for $R_i(q_i, p_i)$ to solve the energy losses. At the end of the chapter we will show the test results of our model.

6.1. Fluxes

Since both synchrotron and inverse Compton losses have the same dependence on p they can be treated as one loss mechanism

$$\left(\frac{dp}{dt}\right)_{\text{Synch+IC}} = \frac{4}{3} \frac{\sigma_T}{m_e^2 c^2} (U_{IC} + U_B) p^2 = \mathcal{C} p^2 \quad (6.1)$$

where \mathcal{C} will be used as a shorthand for the constants and energy densities in the following equations. Inserting Eq. 6.1 into Eq. 3.30 gives

$$\Delta t = \frac{1}{\mathcal{C}} \int_{p_i}^{p_u} dp p^{-2} = -\frac{1}{\mathcal{C}} \left(\frac{1}{p_u} - \frac{1}{p_i} \right) \quad (6.2)$$

As was the case for adiabatic changes this equation can be solved analytically for p_u

$$p_u = \frac{p_i}{1 - \mathcal{C}p_i\Delta t} . \quad (6.3)$$

Inserting this upper boundary into Eq. 3.26 and Eq. 3.27 gives the fluxes of number- and energy density between the bins.

6.2. Spectral Cut Update

Similarly the cut of the momentum distribution can be obtained by solving Eq. 6.2 for p_i , which is equivalent to the spectral cut after a timestep Δt

$$p_{Cut,t+\Delta t} = \frac{p_u}{1 + \mathcal{C}p_{Cut,t}\Delta t} . \quad (6.4)$$

As \mathcal{C} is strictly positive this leads to a consistent shift of the cutoff to lower momenta.

6.3. Number- and Energy Density Changes

As was the case with adiabatic changes, the number density update is defined by the fluxes between momentum bins

$$N_i^{t+\Delta t} = N_i^t + \frac{1}{\bar{\rho}} (F_{n_{i+1}}^m - F_{n_i}^m) \quad (6.5)$$

which can be solved via the analytic solution for the upper momentum boundary p_u in Eq. 6.3. For energy density updates we first need to solve Eq. 3.20 by inserting Eq. 6.1

$$R_i(q_i, p_i) = \frac{4}{3} \frac{\sigma_T}{m_e^2 c^2} (U_{IC} + U_B) \frac{4 - q_i}{p_{i+1}^{4-q_i} - p_i^{4-q_i}} \int_{p_i}^{p_{i+1}} dp p^{4-q_i} \quad (6.6)$$

$$= \frac{4}{3} \frac{\sigma_T}{m_e^2 c^2} (U_{IC} + U_B) \frac{4 - q_i}{5 - q_i} \frac{p_{i+1}^{5-q_i} - p_i^{5-q_i}}{p_{i+1}^{4-q_i} - p_i^{4-q_i}} \quad (6.7)$$

which allows us to solve Eq. 3.21.

As $R_i(q_i, p_i)$ is generally defined as the integral over the sum of all loss processes the integrals can be split up into individual $R_i(q_i, p_i)|_{b_l}$. This makes extension of the model to further loss processes easy, as soon as analytic, or approximate functions of p_u are found.

6.4. Standalone Tests

To check the accuracy of our cooling implementation we used the analytic solution for synchrotron and inverse Compton cooling derived by Kardashev (1962). His Eq. 5 can be reformulated to give the slope q of a distribution at time t

$$q(p, t) = -\frac{\partial \ln f}{\partial \ln p} = q_0 + (q_0 - 4) \frac{tp / (\tau_{p_n} p_n)}{1 - tp / (\tau_{p_n} p_n)} \quad (6.8)$$

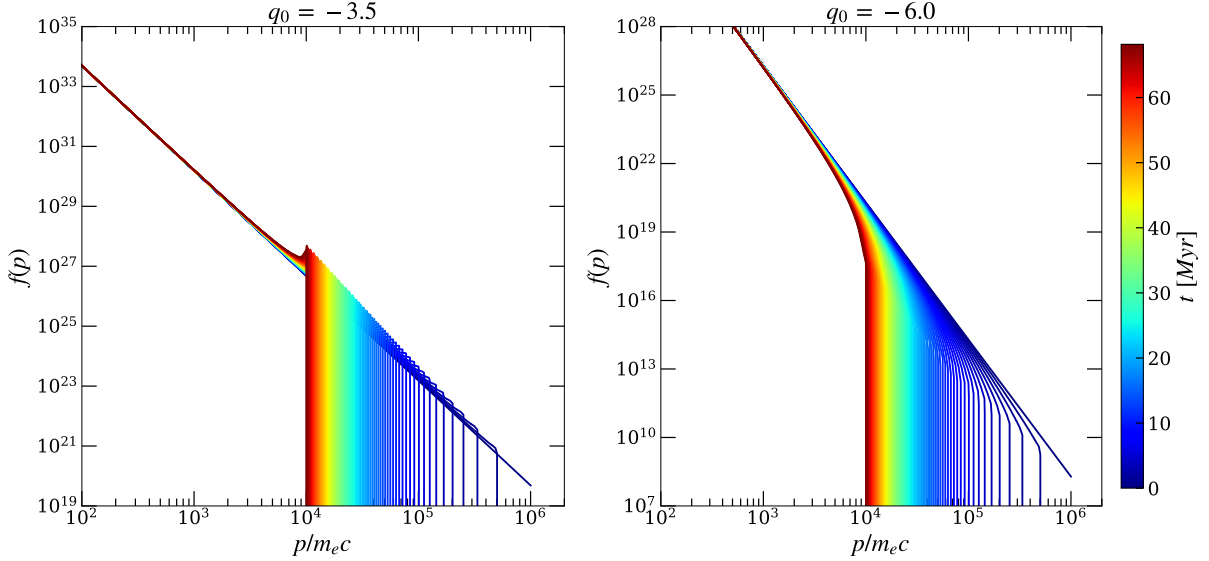


Figure 6.1.: Synchrotron cooling with $B_x = 5\mu G$ and inverse Compton scattering at $z = 0$ with 192 momentum bins.

where τ_{p_n} is the cooling time of some arbitrary momentum p_n . Using the cooling time from Miniati (2001) Eq. 65 and defining for convenience $p_n = 10^4$, $t = \tau_{p_n}$ we arrive at a simple relation for the slope of every bin at the cooling time of p_n

$$q(p) = q_0 + (q_0 - 4) \frac{p/p_n}{1 - p/p_n} . \quad (6.9)$$

From this formulation we can predict different behaviors for $q_0 < 4$ and $q_0 > 4$. For $q_0 < 4$ we expect a decrease in spectral slope, so an upwards bending of the initial spectrum followed by a sharp cutoff at p_n . The physical interpretations of this is that for smaller slopes there are more electrons at the high momentum end of the spectrum than at larger slopes. The Cooling process at high momentum is so rapid that electrons are shifted to lower momenta considerably faster than the electrons at those momenta can cool. This leads to a pileup of electrons in the highest momentum bins below the cutoff. At slopes $q_0 > 4$ there are fewer electrons in the high momentum end and therefore the pileup is avoided. At these initial slopes we expect a spectral steepening and a smooth cooling of the electrons.

To analyze if we reproduce this general behavior we set up a standalone test with with a constant magnetic field of $B = 5\mu G$ and inverse Compton scattering off CMB photons at $z = 0$. Only radiative losses were switched on, all other contributions were switched off. The test was run for different slopes q_0 at a very high momentum resolution of 192 bins. We show two of these tests, namely with $q_0 = 3.5$ and $q = 6.0$ in Fig. 6.1. As expected we observe an upturn of the distribution function followed by a sharp cutoff for $q_0 < 4$ and a gradual steepening for $q_0 > 4$ as the simulation time approaches the cooling time. Furthermore we can see that the spectral cutoff agrees well with the analytic solution,

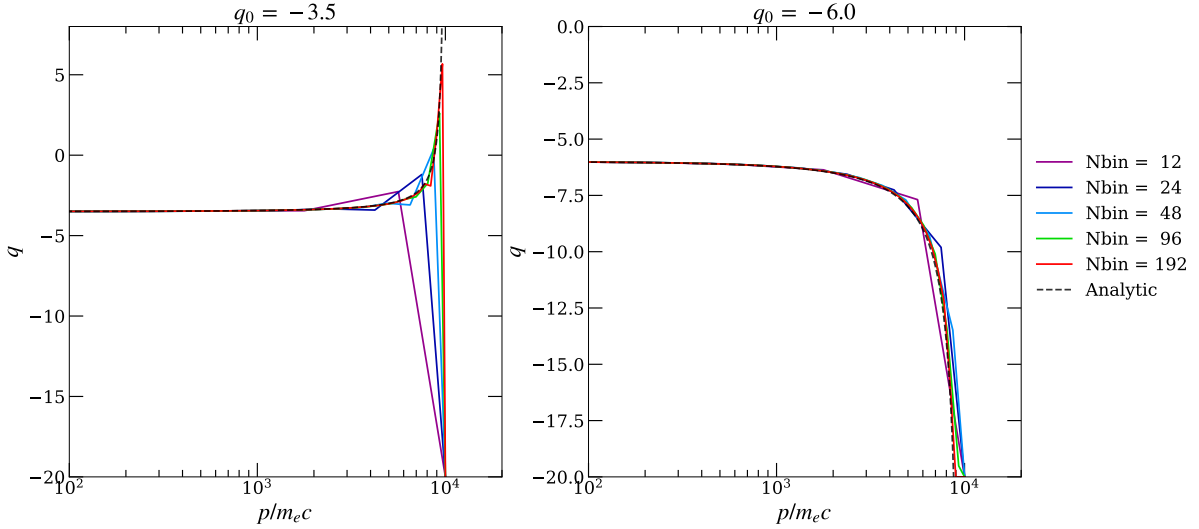


Figure 6.2.: Convergence to the analytic solution for synchrotron and inverse Compton cooling for different numbers of momentum bins.

as in both cases the highest momentum of the spectrum is at $p = 10^4$, which it has to be by test design. To further quantify our agreement with the analytic solution and to test our convergence with momentum bins we analyzed the individual slopes of the bins according to Eq. 6.8. The results of these tests can be seen in Fig. 6.2. Please note that we flipped the sign of Eq. 6.8 here as well as in the titles of Fig. 6.1 to avoid confusion. For both values of q_0 we can observe a nice converging behavior with increasing spectral bin count. While 12 momentum bins are clearly very crude, 24 and 48 bins already start to converge to the expected round shape. With 96 bins the slopes, especially for $q_0 = 6$, are in very good agreement, while the solution with 192 bin can be considered almost perfectly converged. The discrepancy in the last bin observed in all cases is an artifact of how we chose to display the results. As we use lines instead of markers for a cleaner look, we draw a line between the last calculated slope and the maximum value a slope can have. By design all bins above the spectral cutoff are set to a maximum slope, $q_{max} = 20$ in this case, to save computation time. If we did not set that maximum slope we would waste computing time in the root-finding process to update the slope. As bins with a slope higher than 20 contain hardly any energy anyway they are not relevant for the total energy budget and can therefore be ignored. This in turn shows that our calculation of the spectral cutoff works nicely, as all lines end at $p = 10^4$, the maximum momentum possible at the end of the simulation, as defined by the cooling time.

In addition to these accuracy tests we also ran a set of tests to see the impact of the number of momentum bins on computational cost. For these tests we reran the standalone test with a box of 7^3 particles at varying spectral resolutions. We show the results of these tests in Fig. IV.9, transparent lines indicate every timestep, while bright lines are a fit to the mean of ca. 20 timesteps. We normalize the timesteps to the total time, to simplify direct comparison between the runs. As the plot shows the implementation scales very

well with increased bin count. Even at 96 bins, which already showed excellent agreement to the analytic solution in Fig. 6.2, the performance impact is still less than a factor of 2. This is mainly due to our improved root finding in the slope update. Nevertheless the impact on memory consumption is considerable with increased bin count. The run with 384 bins required more than 3 GB of memory for 343 SPH particles. Improvement on memory management, especially concerning which properties have to be stored in the SPH particle struct, should be a high priority in the future.

7. Turbulent Re-Acceleration of Particles

According to Sec. 1.3.3 the reacceleration of particles, or their diffusion in momentum space, is caused by scattering off Alfvén waves, driven by turbulence. Following Cassano and Brunetti (2005) the change in momentum due to turbulent reacceleration per timestep can be expressed as

$$\left(\frac{dp}{dt}\right)_{\text{acc}}^{\text{sys}} = -\chi p \simeq -2 \frac{D_{pp}}{p} \quad (7.1)$$

with the additional minus sign to match our formalism. For an isotropic distribution of wave and particle momenta and $v_A < v_M$, with v_A being the Alfvén velocity and

$$v_M^2 \simeq \frac{4}{3} v_{\text{ion}}^2 + v_A^2 \quad (7.2)$$

the diffusion coefficient D_{pp} is given by Eilek (1979) as

$$D_{pp}(p, t) \simeq 4.45 \pi^2 \frac{v_M^2}{c} \frac{p^2}{B^2} \int_{k_{\text{min}}}^{k_{\text{max}}} dk k \mathcal{W}_k^B(t) \quad (7.3)$$

$$= D_0(t) p^2 \quad (7.4)$$

This assumes that the infall of substructure causes plasma instabilities and turbulence which in turn drives magneto-sonic (MS) waves. These instabilities lead to a stochastic second order Fermi acceleration process, as described in Sec. 1.3.3. The integral on the RHS of Eq. 7.3 is therefore the integral over the spectrum of the MS waves and the boundaries of this integral are defined by the minimum and maximum wave numbers of the underlying turbulence spectrum. Combining Eq. 7.1 and Eq. 7.4 gives the short form of

$$\left(\frac{dp}{dt}\right)_{\text{acc}}^{\text{sys}} = -2D_0(t) p \quad (7.5)$$

This can be solved either by explicitly solving Eq. 7.3 over the relevant turbulence scales, or by giving a constant factor for diffusion in momentum space.

7.1. Explicit Solution for $D_0(t)$

Explicitly solving $D_0(t)$ proves difficult due to the integral on the RHS of Eq. 7.3. Since the time evolution of $W_k(t)$, the modified spectrum of the MS waves, depends on wave-wave interaction and wave-particle interaction and is therefore very expensive to solve.

Cassano and Brunetti (2005) use an approximation that simplifies the form of W_k to only depend on the injection spectrum of the waves $I(k)$, which for this purposes is assumed to be a simple powerlaw $I(k) = I_0 k^{-a}$, and the most prominent dampening mechanism, the dampening by thermal electrons $\Gamma_{th,e}(k)$

$$W_k \simeq \frac{I(k)}{\Gamma_{th,e}(k)} \quad (7.6)$$

with

$$\Gamma_{th,e}(k) = \sqrt{32\pi^3} \rho \sqrt{m_e k_B T} \left(\frac{v_M}{B} \right)^2 \frac{W_k^B}{W_k} \mathcal{I}(x) k \quad (7.7)$$

and

$$\mathcal{I}(x) = 2 \int_1^\infty dx \left(\frac{1}{x} - \frac{1}{x^3} \right) \exp \left[-x^2 \left(\frac{v_M}{v_{th}} \right)^2 \right] \quad (7.8)$$

Here v_M is given by Eq. 7.2 and $v_{th}^2 = \frac{2k_B T}{m_e}$ is the thermal velocity of the electrons. Please see Sec. 4.2 in Cassano and Brunetti (2005) for more details. To explicitly solve D_0 at every timestep we follow the implementation by Donnert and Brunetti (2014) who take this approximation and find that

$$D_0(t) = \frac{4.45\pi^2}{c \sqrt{32\pi^3} m_e k_B} \frac{\eta_t a_k E_{turb}}{n_e V_p \sqrt{T} \Delta t \mathcal{I}(x)} \quad (7.9)$$

where η_t is the free parameter introduced by Cassano and Brunetti (2005) with $\eta_t = 0.2$ in this model, E_{turb} is the turbulent energy, V_p is the kernel volume of a particle and a_k is the turbulent scale factor

$$a_k = \frac{k_{max}^{-2/3} - k_{min}^{-2/3}}{k_{mps}^{-2/3} - k_h^{-2/3}} \quad (7.10)$$

The different components of this are k_{min} and k_{max} for Eq. 7.3, the wavelength of the mean particle separation

$$k_{mps} = \frac{N_{ngb,i}^{1/3}}{2h_i} \quad (7.11)$$

and the maximum wavelength within a kernel of compact kernel support h_i

$$k_h = \frac{1}{2h_i} \quad (7.12)$$

k_{min} and k_{max} are free parameters in this model and can be expressed as the inverse of the injection and dampening scale of the MS waves and for the purpose of this work take the form

$$k_{min} = (\Lambda_{inj})^{-1} = (200 \text{ kpc})^{-1} \quad (7.13)$$

$$k_{max} = (\Lambda_{damp})^{-1} = (0.1 \text{ kpc})^{-1} \quad (7.14)$$

7.2. Fluxes

As for the previous effects we first need to calculate the upper boundaries of our flux integrals. To obtain an analytic solution we assume that $D_0(t)$ is constant over a simulation timestep.

$$\frac{dp}{dt} = -2D_0(t) p = -2D_0 p \quad (7.15)$$

Separation of variable and integrating both sides gives

$$\Delta t = \frac{1}{2D_0} \int_{p'_i}^{p'_u} dp' p'^{-1} \quad (7.16)$$

$$= \frac{1}{2D_0} [\ln(p_u) - \ln(p_i)] \quad (7.17)$$

and with that the upper integration boundary

$$p_u = \exp(\ln(p_i) - 2D_0 \Delta t) \quad (7.18)$$

$$= p_i e^{-2D_0 \Delta t} \quad (7.19)$$

As before, the cut is then updated by solving Eq. 7.19 for p_i and associating this with the new spectral cut after a timestep Δt

$$p_{\text{cut}}(t + \Delta t) = p_{\text{cut}}(t) e^{2D_0 \Delta t} \quad (7.20)$$

7.3. Number- and Energy Density Gains

The number density after a timestep Δt is again given by the fluxes between momentum bins, which can be solved from inserting p_u from Eq. 7.19 into Eq. 3.26 and 3.27 respectively. By treating the turbulent re-acceleration as an additional loss term¹ for simplicity we can reuse Eq. 3.21 by solving R_i as

$$R_i(q_i, p_i) = \frac{4 - q_i}{p_{i+1}^{4-q_i} - p_i^{4-q_i}} \int_{p'_i}^{p'_{i+1}} dp p^{2-q_i} \left(\frac{dp}{dt} \right)_{\text{acc}}^{\text{sys}} \quad (7.21)$$

$$= -2D_0(t) \frac{4 - q_i}{p_{i+1}^{4-q_i} - p_i^{4-q_i}} \int_{p'_i}^{p'_{i+1}} dp p^{3-q_i} \quad (7.22)$$

$$= -2D_0(t) \frac{4 - q_i}{p_{i+1}^{4-q_i} - p_i^{4-q_i}} \frac{p_{i+1}^{4-q_i} - p_i^{4-q_i}}{4 - q_i} \quad (7.23)$$

$$= -2D_0(t) \quad (7.24)$$

¹In a last-minute revision we noticed that this may not be valid due to the dependence on $\frac{\partial^2 f}{\partial p^2}$ and therefore has to be revisited in future work.

and then evaluating the time integration.

7.4. Standalone Test

To test the functionality of the turbulent reacceleration model we set up another standalone test. Here we set up an initial distribution as in the adiabatic and radiative tests and evolved the distribution with a constant factor of $D_{pp} = 10^{-18} \frac{1}{s}$. This value is roughly the mean of what Donnert and Brunetti (2014) used from the simulation of Cassano and Brunetti (2005) to test the convergence of their model.

As a first test we only looked at the reacceleration term and how it modifies the spectrum. From an initial powerlaw spectrum we expect the distribution to contain its shape and only be shifted to the right, as re-acceleration should be a self-similar process (e.g. Fermi (1949)). The result of this test can be seen in Fig. 7.1. We can observe a slight right-shift of the distribution function, while the overall shape stays intact.

Next we reran the test, but also allowed for synchrotron losses with a constant magnetic field of $B = 5\mu G$, as in Sec. 6.4. For this test we expect the synchrotron losses to dominate over the re-acceleration, until the high energy electrons are cooled off. Once the cooling time of the remaining electrons is equal to the re-acceleration timescale the two effects should balance the spectral cutoff at some value. We tried to illustrate this behavior in the left of Fig. 7.2. As can be seen in the case without re-acceleration the spectral cut decreases constantly, while in the case with re-acceleration the cut starts to be balanced and heads towards a stable value. Unfortunately there was still a slight error in the model by the time of this writing and the re-acceleration caused the model to break if too much energy is cooled off by synchrotron or inverse Compton losses. Besides our best efforts we were not able to find this bug in time and refer this problem to future work.

7.5. $D_0(t)$ from Cluster Merger

To test the time-dependent implementation of D_{pp} , calculated on every timestep via Eq. 7.3, we set up a test simulation of a cluster merger similar to the one discussed in Sec. 8, but with additional substructure. The initial condition can be seen in Fig. IV.10. For details on the initial condition setup and SPH mapping details, please see Sec. 8. The left part of Fig. IV.10 shows the surface density of the system, while the right part shows the magnetic field strength. As this model contains infalling substructure, the approach by Cassano and Brunetti (2005) that turbulence is triggered by ram-pressure stripping is physically motivated. Unfortunately as was the case in the standalone model the same bug caused the simulation to crash at $t \sim 500\text{Myrs}$. Nonetheless, in the right plot of Fig. 7.2 we show the obtained values for $D_0(t)$. We note that these lie slightly above the values from Cassano and Brunetti (2005), but attribute this to the very different nature of the simulated systems. Nonetheless this needs to be further investigated in future work, once the problems with the implementation have been fixed.

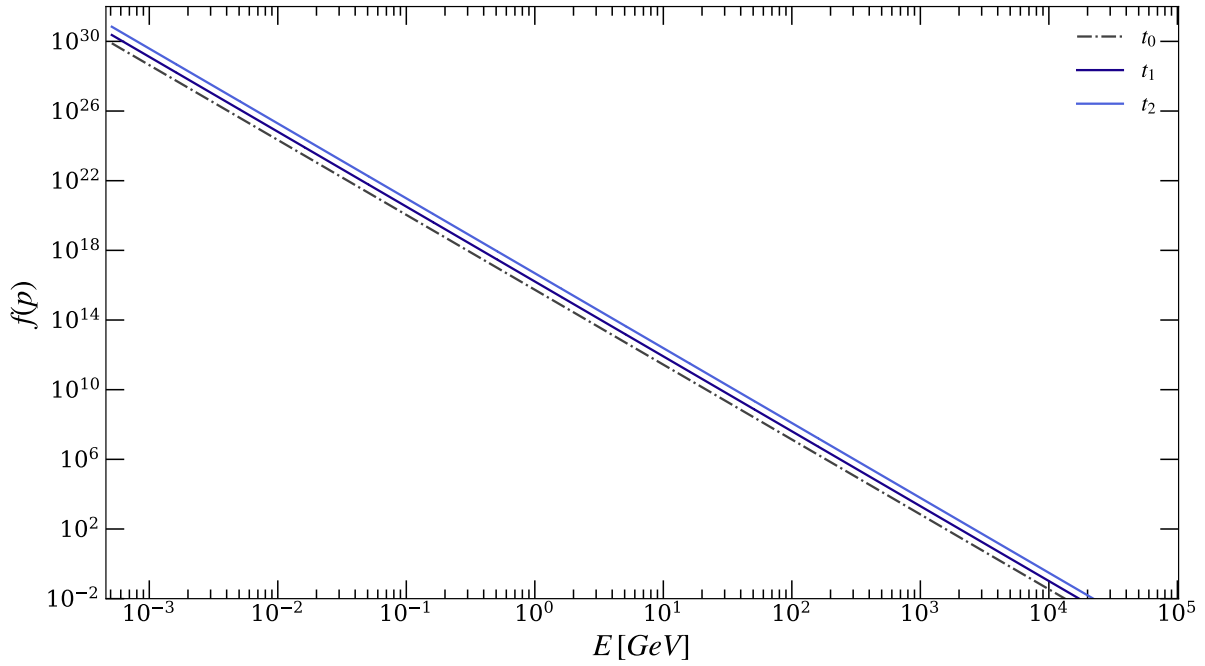


Figure 7.1.: Distribution function shift due to turbulent re-acceleration with constant momentum diffusion coefficient $D_{pp} = 10^{-18} \frac{1}{s}$.

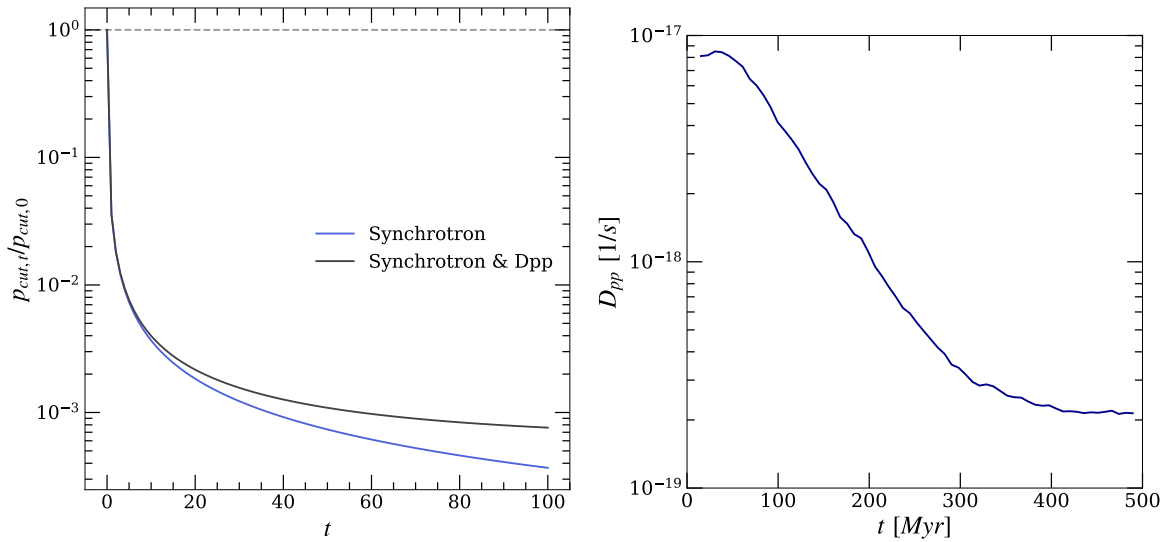


Figure 7.2.: Left: Test of simultaneous synchrotron losses and D_{pp} reacceleration. Shown are the cutoffs of the spectra relative to the initial cut. Blue: Pure synchrotron losses. Black: Synchrotron losses balances by D_{pp} reacceleration. Right: $D_0(t)$ obtained from a cluster merger simulation with infalling substructure.

8. Idealized Galaxy Cluster Merger

To test our model in a more physical test case than shocktubes we ran a set of idealized galaxy cluster merger simulations. All simulations were run with the single weighted shock finder, advanced SPH and full MHD. For the CR model we used 48 bins, adiabatic changes updated before every pressure calculation of the main code, radiative losses and shock injection. CRs are injected following the efficiency model of Ryu et al. (2019) with an electron to proton ratio of $R_{e/p} = 0.005$.

We did not employ turbulent re-acceleration of particles due to the idealized nature of the simulation. Since we only sample two smooth halos without substructure (see 8.1) the fundamental concept of turbulence injected by the ram-pressure stripping of infalling substructure cannot hold. Furthermore we did not use the B-field angle dependent efficiency term η_B (see 4.1.3) because of the simplified nature of our initial magnetic field structure.

The construction of images by means of SPH mapping was performed with the `Smac` code, see Dolag et al. (2005a) for details about the mapping process and conservation of quantities. Mapping of gas surface density and magnetic field was performed over a thick slice containing 5 Mpc of the box. Mach number and CR pressure to thermal pressure ratio (X_{cr}) mapping is confined to a thin slice of 200 kpc, which corresponds to roughly the kernel size of particles at the outskirts of the clusters. This leads to slightly more numerical noise, as the particle count used for mapping is smaller, but avoids geometric projection effects.

8.1. Initial Conditions

The setup of the initial conditions (ICs) was performed with the `ToyCluster` code in the same way as described in Donnert (2014), albeit at much lower resolution. Donnert (2014) uses the analytic solution of the Hernquist profile (Hernquist (1990)) to sample a dark matter halo with a pre-defined mass. For the gas component a β -profile (Cavaliere and Fusco-Femiano (1978)) whose gas density follows

$$\rho_{gas}(r) = \rho_0 \left(1 + \frac{r^2}{r_c^2}\right)^{-\frac{3}{2}\beta} \quad (8.1)$$

is set up in such a way that it is in hydrostatic equilibrium. See Donnert (2014) Eq. 6-13 for details.

The magnetic field is modeled as proposed by Bonafede et al. (2010) and follows a radial

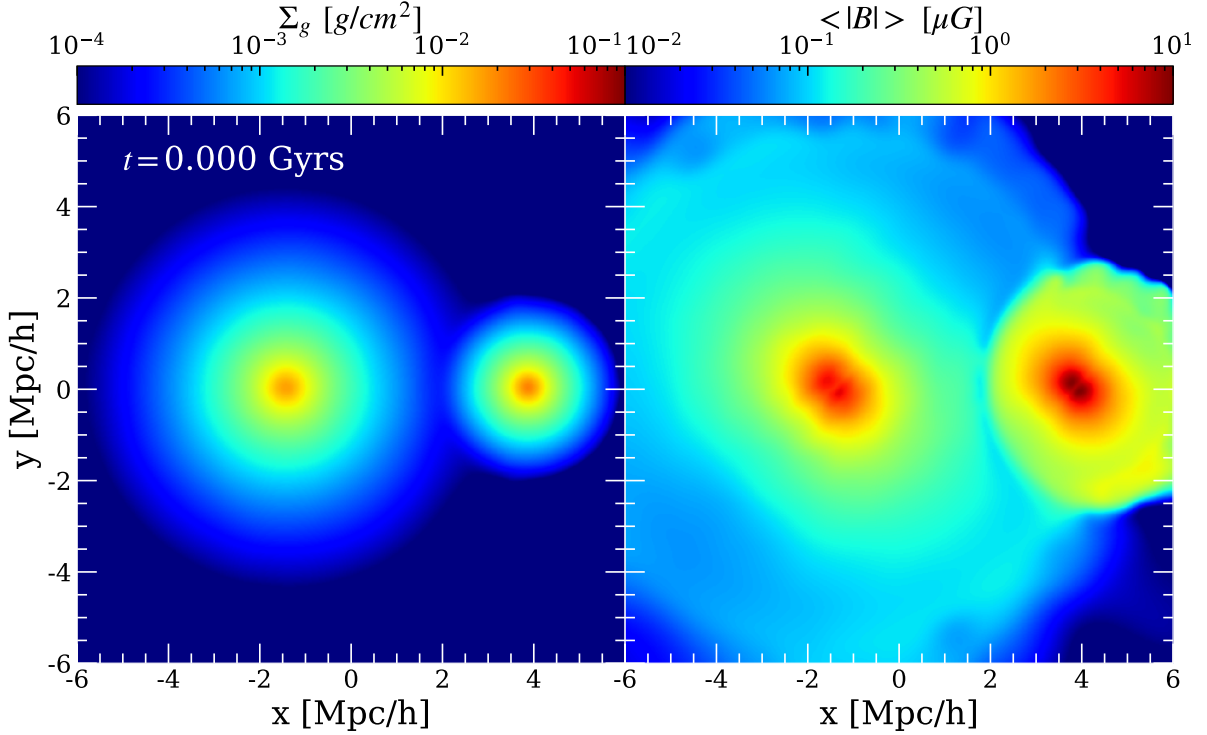


Figure 8.1.: Initial conditions of the cluster merger. Left shows the gas surface density, right shows the magnetic field. Both images are mapped to a grid using a 5 Mpc slice of the box.

distribution of

$$\langle \vec{B} \rangle(r) = \langle \vec{B}_0 \rangle \left(\frac{n_e(r)}{n_0} \right)^\eta \quad (8.2)$$

where \vec{B}_0 and η are free parameters.

The initial conditions of the merger can be seen in Fig. 8.1. Our ICs contain 2 million particles, half gas and half dark matter. The mass ratio of the clusters is roughly 2:1 with the left cluster being the more massive one. All relevant properties of the merger setup can be found in Table 8.1. Halo 0 (left) will also be referred to as the target, Halo 1 (right) as bullet. Please note that the magnetic field on the right hand side of Fig. 8.1 looks more disturbed than the density on the left hand side since the figure shows snapshot 0. As OpenGadget3 performs an initial halfstep kick on startup, before writing the zeroth snapshot, the magnetic field has already been evolved for half a timestep and is therefore distorted.

8.2. Results

We will analyze the results of the idealized cluster merger in three steps. First in Sec. 8.2.1 we will look at the whole system and where CRs are injected by the resulting shocks,

	Halo 0	Halo 1
N_{Total}	1493726	506274
N_{Gas}	738257	261743
N_{DM}	755469	244531
$M_{Total} [M_{\odot}]$	1.00789e+15	4.99924e+14
$M_{Gas} [M_{\odot}]$	1.4604e+14	7.25556e+13
$M_{DM} [M_{\odot}]$	8.61853e+14	4.27368e+14
$\rho_0 [g/cm^3]$	6.56805e-27	1.20976e-26
$r_c [kpc]$	215.588	159.986
$ B [\mu G]$	5.0	5.0
η	0.5	0.5
$\Delta x_{COM} [kpc]$	-1233.38	2466.77
$v_x [km/s]$	497.992	-1493.97

Table 8.1.: Properties of the merging halos.

next in Sec. 8.2.2 we will look at the strong shock after the first passage of the cluster cores and last we will analyze the properties of a single SPH particle as it runs through that shock and how its spectrum evolves over the simulation in Sec. 8.2.3.

8.2.1. Time Evolution of the Merger

To illustrate the time evolution of the merger we show 4 different times of the merger process in Fig. 8.2 and 8.3. We plot the logarithm of the density integrated over a 5 Mpc slice in black and white. The limits are the same as in the left hand side of Fig. 8.1, we therefore don't use an additional colorbar to avoid confusion. The colorbar indicates Mach number and the ratio between CR proton pressure component and thermal pressure component (X_{cr}), respectively. As previously described we only take a 200 kpc slice of these quantities to avoid projection effects.

The top of Fig. 8.2 shows a very early stage of the merger, shortly after the impact of the outer parts of the bullet halo into the target halo. While we can observe density waves indicating a shock moving through the cluster, the slice we used for Mach number measurements does not contain any supersonic shocks in that area. Looking at the right side of the plot we can see that there must have been a supersonic shock moving through the medium, as there has been shock acceleration of particles, still visible in the wake of the shockwave. In the bottom plot of Fig. 8.2 the system is in the state shortly after the first passage of the bullet through the target cluster. A symmetric bow shock can be observed to the left of the cluster center, with a radius of ~ 500 kpc. Furthermore there is a weak shock following the v-shaped density structure of the in-falling halo. In the wake of the cluster there is an additional shock structure which resembles the complex c-shaped shock structure observed in Beck et al. (2015a). The pressure ratio on the right again shows a region of CRs accelerated by the shocks near the cluster center and in the wake of the cluster. Additionally we can observe remnants of the initial shock still present

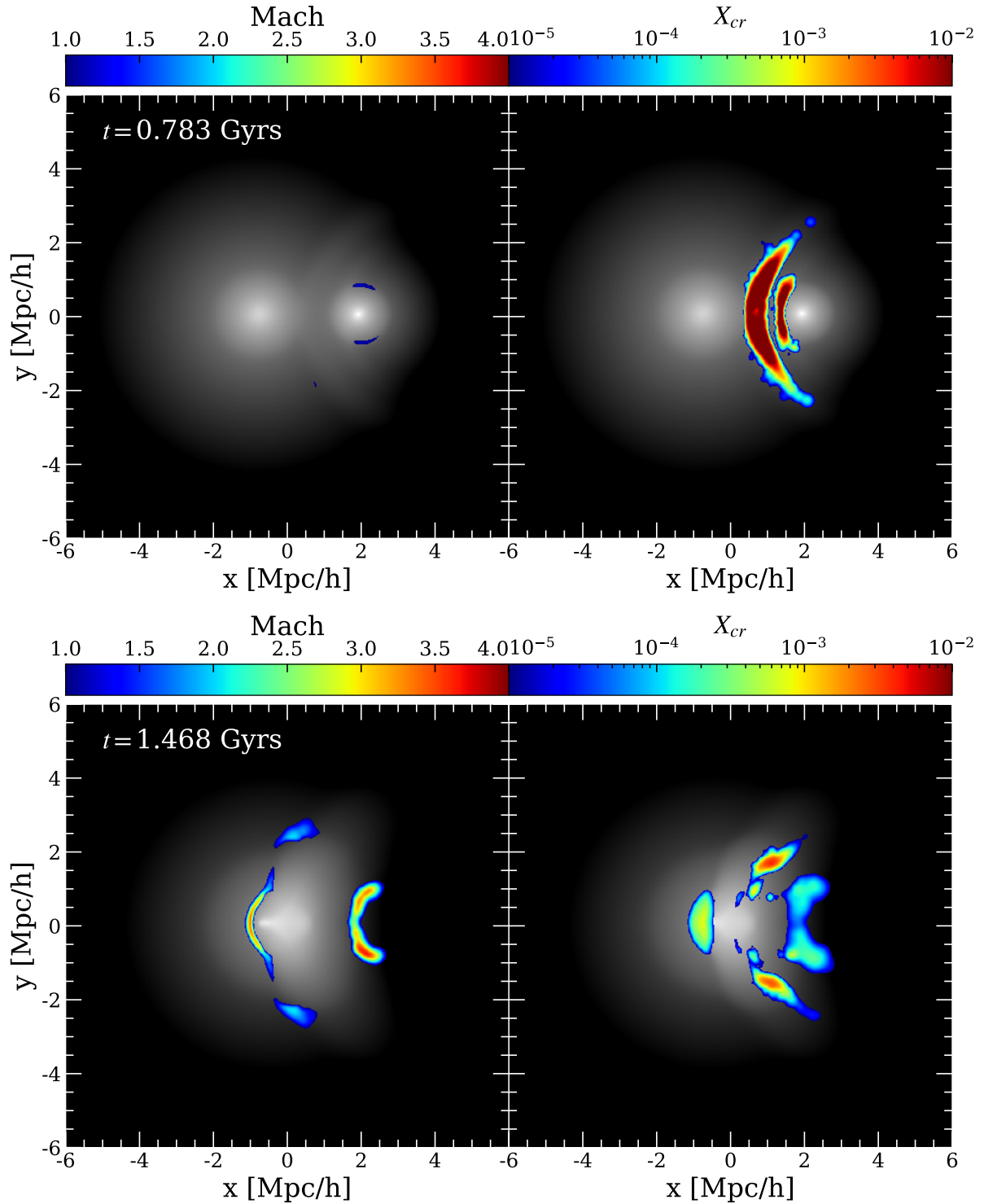


Figure 8.2.: Left panels: Surface density overplotted by Mach number. Right panels: Surface density overplotted by CR to thermal pressure ratio X_{cr} . Top: State of the merger shortly after initial contact of the halos. Bottom: State of the merger shortly after first passage of the cluster cores.

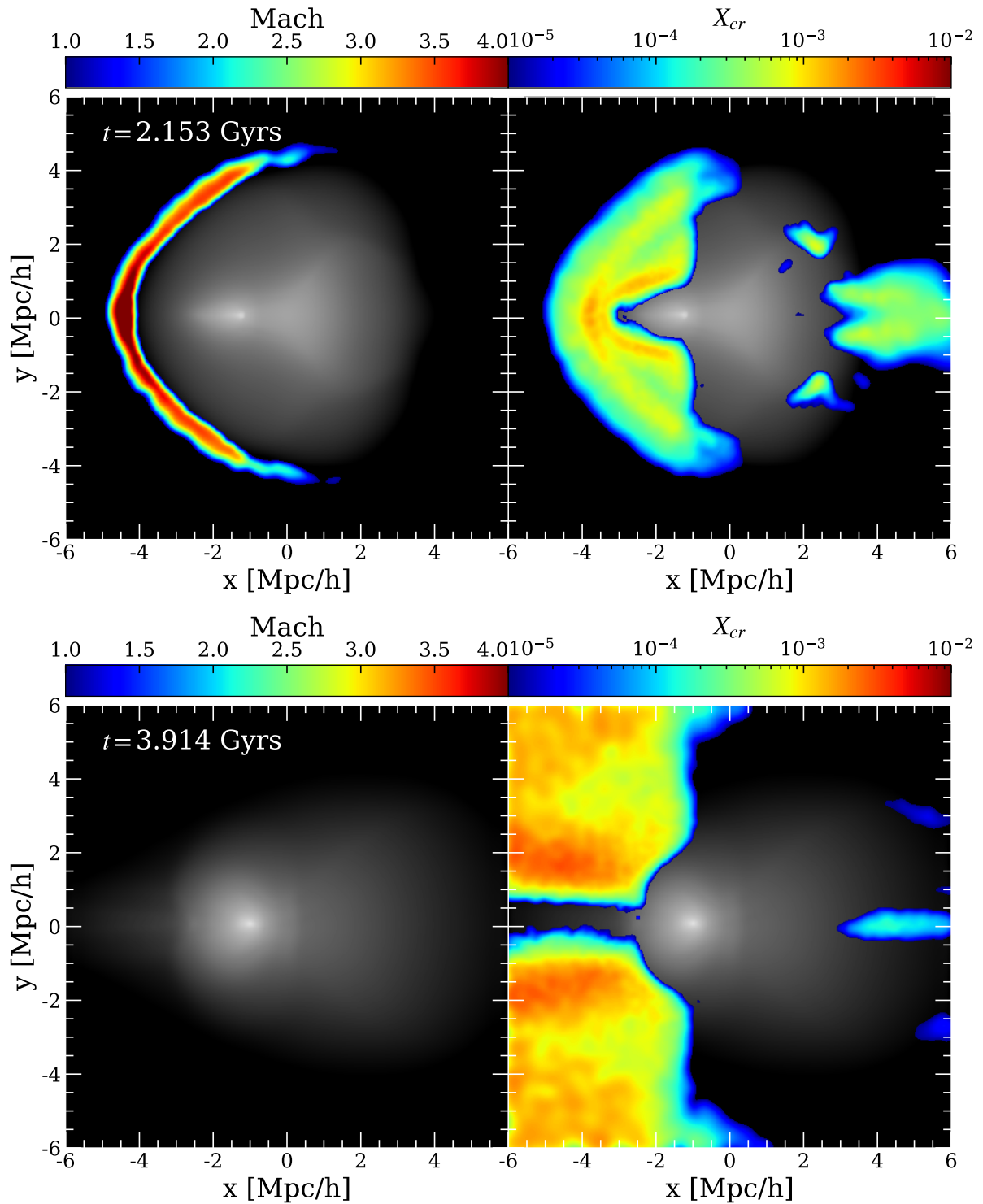


Figure 8.3.: As in Fig. 8.2. Top: State of the merger after the second core passage with outwards moving shock front. Bottom: End of the simulation with merged clusters, still undergoing relaxation.

off-axis of the merger. These are located at around ± 2 Mpc/h in y -direction and show high values for X_{cr} . Further analysis shows that this is the case because these CRs were initially accelerated by the first shock front moving ahead of the bullet cluster and now splash back due to the shock front caused by the target cluster. Since the target cluster also travels at a high velocity and is not stationary it causes a shock moving into to right side of the simulation domain. This weaker shock seems to be enough to re-accelerate particles, cause the high value for X_{cr} and move the CR component further to the right in later snapshots.

The top part of Fig. 8.3 shows the outward traveling merger shock as it reaches the outskirts of the cluster. We can see a very symmetric shockfront with a radius of about 4 Mpc traveling away from the clusters at more then Mach 4. The corresponding X_{cr} signal shows that there is consistent CR acceleration happening all along the shock front. In addition to the new acceleration we can see a significant CR component at the border of the newly formed cluster core. This is due to previously accelerated CRs in that region being folded around the core by infalling gas. On the right side of the cluster we can still observe the remnants from the CR acceleration at the wake and the initial shock wave entering the cluster.

In the bottom part of Fig. 8.3 the merger itself is complete, even though the resulting cluster has not relaxed yet. As can be seen in the left plot there are no more shocks running through the cluster and the two cluster cores have settled into one. In the right plot we can still observe multiple relics of the acceleration at the right side of the cluster. The outskirts of the cluster left of the initial center of mass shows a large fraction of CR pressure component. This can be attributed to the cold gas outside of the cluster and our lack of diffusion in the model. As the shock travels outwards from the cluster, to the background gas, there is still a significant rate of acceleration. The Mach number will increase, as the sound speed in the surrounding medium drops while the shock speed stays constant. This increases the acceleration efficiency and leads to a fairly homogeneous value of $X_{cr} \sim 1 - 3 \cdot 10^{-3}$. Since we did not implement spacial diffusion in this model and there are no more adiabatic changes happening in the outskirts of the cluster at this stage of the merger we expect this steady state behavior. In the case with spacial diffusion we would expect the CR component to also be present around the cluster on the right side of the center, as it should have diffused over the simulation volume by the end of the simulation.

8.2.2. Analysis of the Initial Shock Front

To get a more detailed picture of the properties of the initial shock front at 1.5 Gyrs we extracted a thin slice of the merging system. The location and size of the slice we base the following analysis on is marked with white lines in Fig. 8.4. It extends 1.3 Mpc in x direction, from shortly before the shock to ca. the center of mass of the system. In y and z direction we take only a very thin slice of 20 kpc to minimize geometric effects. As in the left sides of Fig. 8.3 + 8.3 the black and white refers to the surface density, while color refers to the Mach number detected by the shock finder.

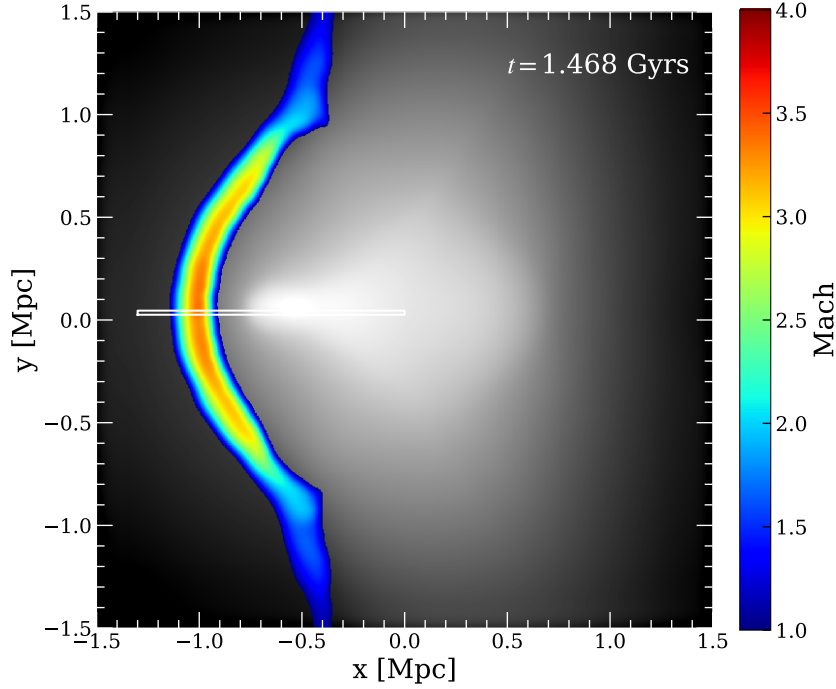


Figure 8.4.: Zoom on the first developing shockfront. The background indicates surface density, colors show the Mach number and the white lines represent size and location of the slice for Fig. 8.5

To get a comparison for the shock properties we reproduced a slightly modified version of Fig. 9 in Beck et al. (2015a). Fig. 8.5 shows some of the key properties of the initial shock front. Solid lines represent the result of the simulation with all particles plotted. Dotted lines indicate the size of the kernel of the particle with the highest Mach number. The top left panel shows the density profile along the slice to the cluster centers. While the density shows no indication of a shock front, it is clearly visible in the temperature jump in the left middle panel. Top and middle panel on the right show shock speed and sound speed respectively. While the shock speed is a direct output of the shock finder, the sound speed is calculated in post-processing via Eq. 2.36. This allows for a consistency check, via calculating the Mach number of every particle 'by hand'. As they match perfectly with the output Mach numbers we omit overplotting the result here for clarity. The output Mach number is shown in the bottom right plot. The maximum Mach number is detected to be $M = 3.74$ and nicely coincides with the maximum of the temperature jump. This almost perfectly matches the original results by Beck et al. (2015a), even at the lower resolution. Finally the bottom left panel shows the ratio between CR pressure and thermal pressure X_{cr} . The maximum value reaches $X_{cr} \approx 3.5 \cdot 10^{-3}$ which is very close to the ideal value (see Fig. 4.2), albeit a little too low. Concerning the structure of the injected component we can see that it slightly trails behind the temperature jump, contrary to slightly before, as in the shocktube tests (Fig. 4.3). This gives further confidence in the applicability of

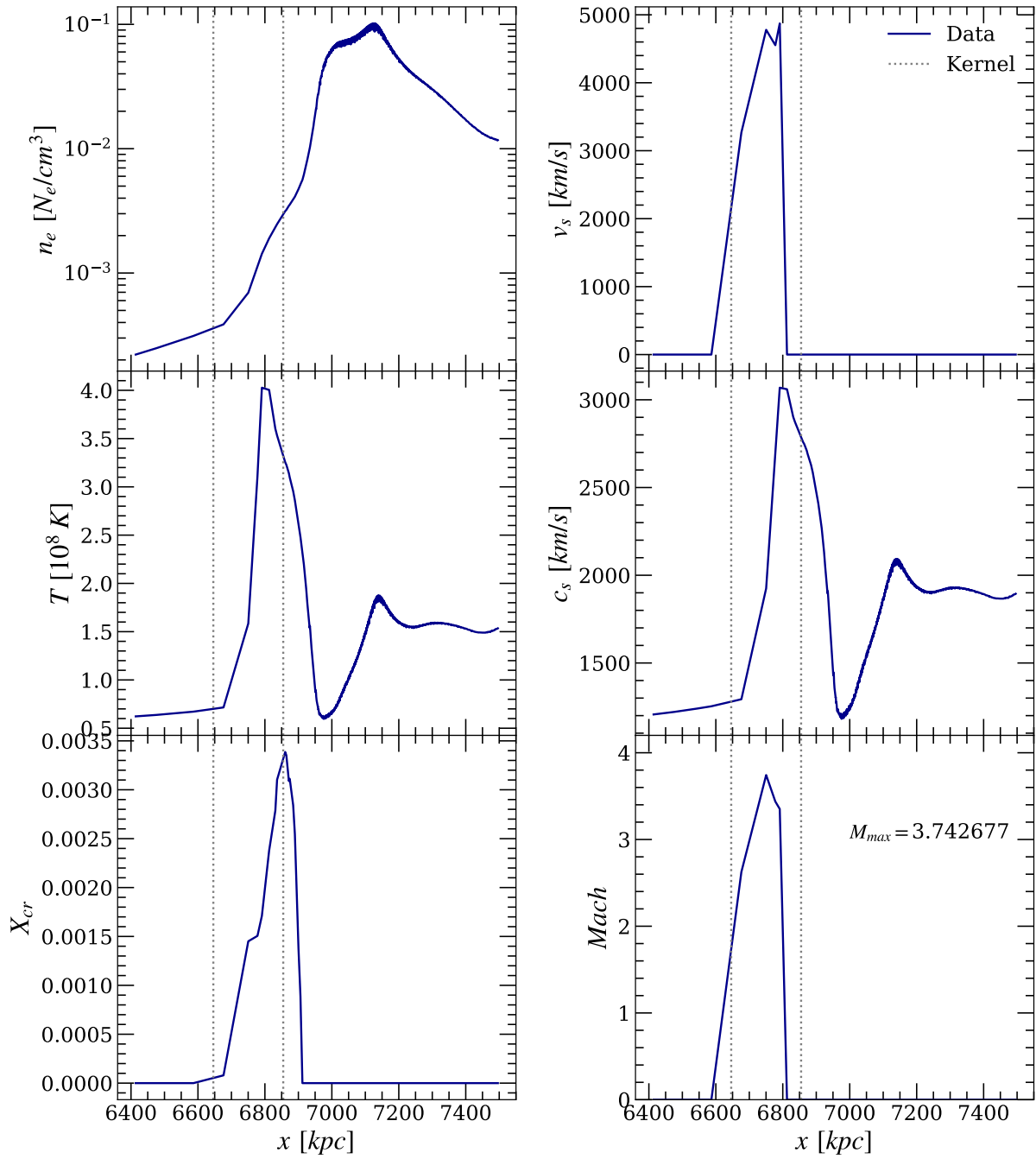


Figure 8.5.: Particle properties within the slice indicated in Fig. 8.4.

the model to realistic problems.

8.2.3. Analysis of a Single Shocked Particle

As a final step we analyze a single SPH particle and look at the injection of the CR component and its spectral evolution. We picked the particle with the maximum Mach number of Fig. 8.5.

The injection process can be seen in Fig. 8.6. The left panel shows the detected Mach number, the middle panel the corresponding injection efficiency $\eta(M)$ and the right panel the shock energy and the final injected CR energy. We plot the values for every timestep and normalize the total time the particle "feels" the shock to 1.

The Mach number panel on the left shows the familiar behavior of the particle running into the shock, increasing its Mach number as it travels through the shock front and reaching the maximum Mach number in the center of the shock, as the outskirts of its kernel can reach both the real up- and downstream properties. Except for a single timestep with a miss-identification of the Mach number this works very accurately in the first half of the shock. The second half shows the expected decline as the particle leaves the center of the shock, but shows considerably more noise. In the middle panel the efficiency shows very similar behavior, since the efficiency model by Ryu et al. (2019) is fairly linear in this Mach number regime and the variance in Mach number over the shock is not large. The miss-identification of the Mach number lead to a detected Mach number below the minimum one required by the model and therefore the efficiency was zero over two timesteps. While this is unfortunate, it is only a small error over the course of the injection process. In the right panel we can see that the shock energy stays very constant over the entire injection phase, which again shows that our correction for the kernel broadening (Eq. 4.3) works very well. The injected energy E_{CR} is therefore also very constant, except for the already mentioned two timesteps with zero injection efficiency.

Fig. 8.7 shows the spectral and density evolution of the same particle over the whole simulation. In the top plot we can see the spectral evolution of protons (left) and electrons (right). We plot normalization of the distribution function as a function of dimensionless momentum. The colors indicate the time evolution of the simulation. In the lower plot we show the density evolution of the same particle.

In the evolution of the proton spectra we can see the injection as a single power law at $t \approx 1.5$ Gyrs and the consequent left-shift of the distribution with adiabatic expansion, as indicated in the density plot. Overall the distribution contains a consistent powerlaw shape, with two exceptions. First we can see inconsistencies at the high momentum end of the spectrum. The slopes of the higher momentum bins diverge from the slope of the initial spectrum. While this is aesthetically displeasing, the kinetic impact of the highest momentum bins is too small for this to impose a large error.

What poses a problem is the rise in the low momentum bins over the last three snapshots. As this happens in both protons and electrons it is either a problem with the shock injection, or the adiabatic changes. Since the particle did not experience any more shocks according to the output file, and the slope of the zeroth bin is larger than 12, which can't be achieved by a shock of minimum Mach 2.25, which is required by the efficiency function, we attribute this issue to the adiabatic changes. More specifically since the injection norm is defined by the number density and the norm is most likely the source

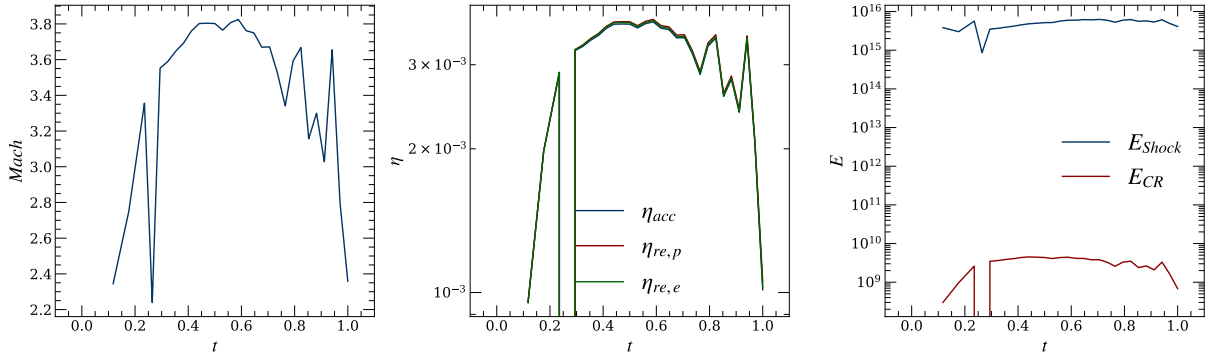


Figure 8.6.: Properties a particles experiences over the first shockfront.

of the error we expect the error to be in the number density calculation. This needs to be examined further in future work.

The evolution of the electron spectra shows an additional problematic feature at the high momentum end. This feature must therefore come from the synchrotron and inverse Compton cooling. One reason of that may be a lack of timestep constraint. Since the high momentum cooling is so efficient we can't resolve the update of the spectral cutoff with the usual simulation timestep. Miniati (2001) notes that to accurately follow the evolution of the high momentum regime the timestep Δt must follow

$$\Delta t \leq 0.1\tau \quad (8.3)$$

where τ is the cooling time of synchrotron and inverse Compton cooling at the spectral cutoff. Considering Fig. 1.4 we can see that the cooling time at the highest momentum of $\hat{p}_{max} \approx 1\text{Myr}$ this would lead to a maximum timestep of $\Delta t_{max} = 0.1\text{Myr}$. We note that this is about one order of magnitude below the mean timestep of the merger simulation. Additionally we find that the error in the high momentum cooling is emphasized by the spectral slope. As seen in Fig. 6.1 the cooling losses with a slope smaller than 4.0 are more prone to error. Considering the Mach 3.75 shock in the merger we would expect from the analytic solution a compression ratio of $x_s = 3.3$ and with that an injection slope of $q_0 = 4.3$. In the simulation data at $t \approx 2\text{ Gyrs}$ we find a mean slope of $\bar{q} = 3.47$. Part of that can be explained by our slope correction, introduced in Sec. ???. Assuming again a correct compression factor from the shock finder we would expect a slope due to our correction factor of $q_0 = 3.91$. This means that the compression factor measured by the shockfinder is slightly overestimated in physical simulations and that our correction factor should not applied in this case to not increase this error. We will need to revisit this problem in future work.

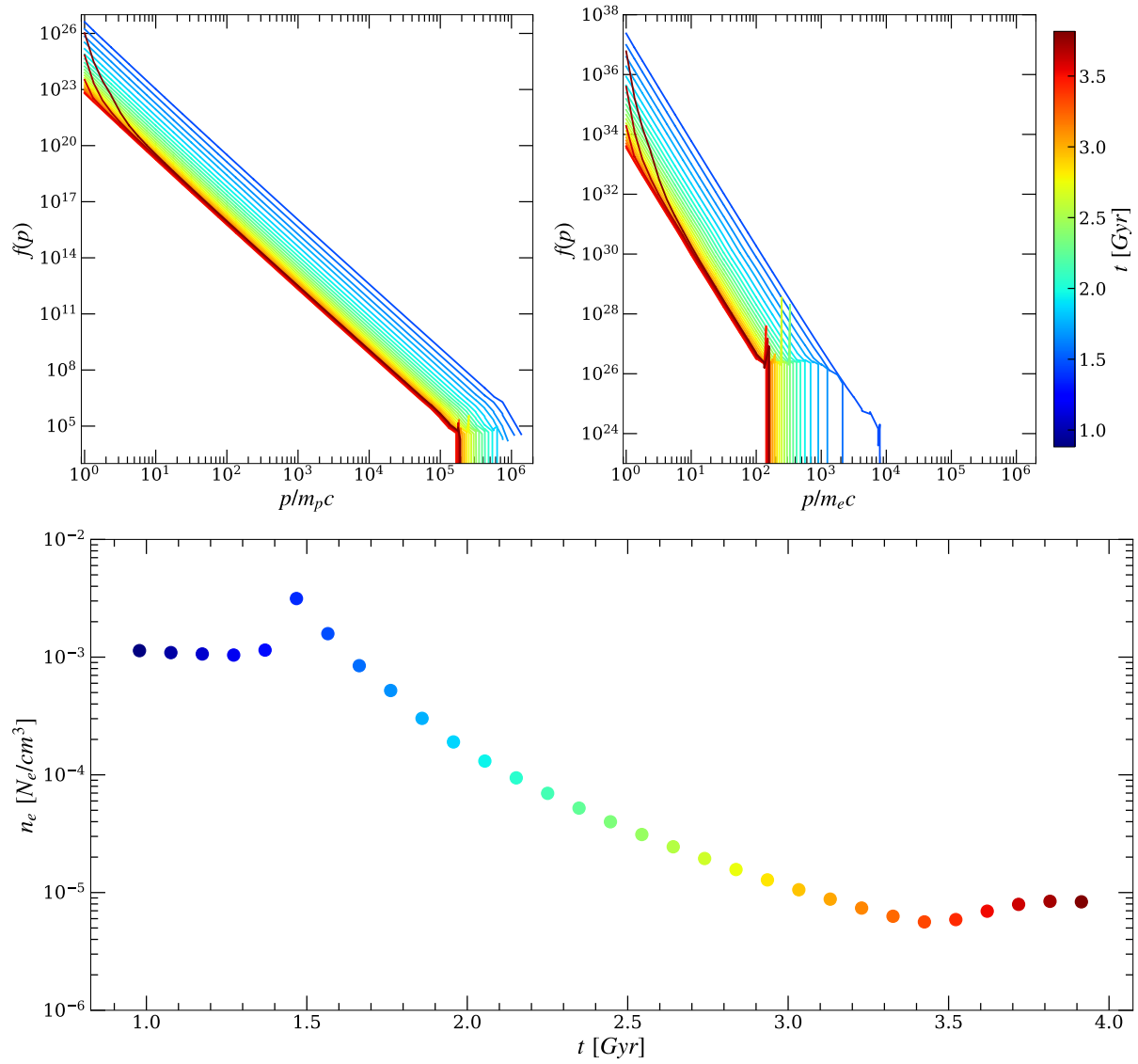


Figure 8.7.: Top: Spectral evolution of a single particle. Left: Protons. Right: Electrons.
Bottom: Density evolution of the same particle.

9. Conclusion and Outlook

In this work we presented a novel implementation of an on-the-fly Fokker-Planck solver to model spectrally resolved Cosmic Ray physics in cosmological simulations. We will summarize the key results of this work in the following and will address open problems that need to be revisited in future work.

9.1. This Work

In Sec. 4 we showed the implementation of CR injection due to shock acceleration. We presented four different models for Mach number dependent acceleration efficiencies. Tests showed that we agree very well with the analytic solutions and can capture the post-shock CR pressure component accurately, while showing high numerical stability even at very strong shocks. Additionally we introduced an efficiency parameter depending on the angle between shock normal and magnetic field. We showed that our description is capable of capturing the angle with high accuracy and we again agree very well with the analytic solution. The slope of the injected spectrum is also captured within a reasonable margin by our implementation. Lastly we tested a subgrid model for CR injection at supernova shocks. This model does not yet deliver satisfying results and needs to be revisited in future work.

Sec. 5 discussed our implementation of adiabatic changes. We showed that our treatment of boundary conditions leads to a consistent preservation of the shape of the distribution function. For adiabatic compression this introduces a systematic error of $\sim 15\%$, which is to be expected, since our implementation of compression does not conserve CR energy. Nonetheless we found in shocktube tests that the total energy is still conserved and our coupling to the hydro solver stays stable even for large Mach number shocks. In the case of adiabatic expansion due to cosmological expansion our model also stays stable and preserves its powerlaw shape within a small margin of error. Still we find a small error in the CR energy under expansion, which has to be analyzed further in future work.

For the radiative losses in Sec. 6 we found excellent agreement in the standalone tests. The model converges nicely to the analytic solution with increased bin count. We find that the agreement for models with 24 bins is acceptable, while with 48 bins and above it shows good convergence. Additionally the scaling tests showed that our improvements to the slope finding method are rewarding and that our model scales very well with computational cost. The cost in memory needs to be addressed in future work, but has many options for improvement at this point.

The re-acceleration of particles due to turbulence discussed in Sec. 7 shows in principle promising results, but needs to be revisited in future work, as our current treatment as

an additional loss mechanism is likely not valid. Regardless of the implementation in the Fokker-Planck solver our time-dependent calculation of $D_0(t)$ gives first promising results and needs to be tested further in real simulation setups.

Finally in Sec. 8 we used most of the effects implemented in the model to run an idealized galaxy cluster merger simulation. This test showed overall promising results. The injection worked even in more complex environments, adiabatic expansion shifted the distribution function as expected and radiative losses for electrons lead to the expected spectral cutoff. Nonetheless we still found some issues, like the wrong slope due to our unnecessary slope correction at injection, noise in the high momentum radiative losses for electrons and an unexpected upturn of the distribution function at low momenta towards the end of the simulation. All these issues need to be investigated further.

All in all we are confident that this work lay the foundation for many interesting projects in the future.

9.2. Future Work

To expand this model we will need to add some more effects in the near future.

First and foremost we will need to implement some form of spacial diffusion. This will be based on the anisotropic thermal conduction model by Arth et al. (2014). Preliminary studies could be done with a simple Bohm-like isotropic diffusion model, as a proof of concept. It would also be worth to study different diffusion models, as recently done by Hopkins et al. (2020b) and different diffusion velocities, see e.g. Holman et al. (1979).

Next we will need to implement Coulomb losses for electrons and protons to mediate the kinetic impact of protons on the surrounding gas and to accurately trace the spectrum of electrons.

In addition to that the treatment of catastrophic losses and production of secondary electrons needs to be implemented. This can be based on the work by Dolag and Ensslin (2000).

Furthermore we will need to reformulate the solver to use comoving coordinates and code units. Currently we convert all required properties into physical CGS units. This works well, as we saw in the case of the Bertschinger test for adiabatic expansion, but is computationally expensive. A basis for this is given in Pfrommer et al. (2016).

On the post-processing side we will need to implement the construction of synchrotron spectra and radio emission from our CR electron spectra into the SPH mapping code `Smac`. We started some preliminary work on this for the similar code `P-Smac2`, which showed promising results, see Fig. 4.11. This will allow us to construct mock radio observations from our self-consistently evolved electron spectra and compare those to real observations. Finally we will need to invest some more time into performance and memory consumption improvements to meet the ambitious science goals of the upcoming COMPASS simulation set.

Bibliography

Ackermann, M., M. Ajello, A. Allafort, L. Baldini, J. Ballet, G. Barbiellini, M. G. Baring, D. Bastieri, K. Bechtol, R. Bellazzini, R. D. Blandford, E. D. Bloom, E. Bonamente, A. W. Borgland, E. Bottacini, T. J. Brandt, J. Bregeon, M. Brigida, P. Bruel, R. Buehler, G. Busetto, S. Buson, G. A. Caliandro, R. A. Cameron, P. A. Caraveo, J. M. Casandjian, C. Cecchi, O. Celik, E. Charles, S. Chaty, R. C. G. Chaves, A. Chekhtman, C. C. Cheung, J. Chiang, G. Chiaro, A. N. Cillis, S. Ciprini, R. Claus, J. Cohen-Tanugi, L. R. Cominsky, J. Conrad, S. Corbel, S. Cutini, F. D'Ammando, A. de Angelis, F. de Palma, C. D. Dermer, E. do Couto e Silva, P. S. Drell, A. Drlica-Wagner, L. Falletti, C. Favuzzi, E. C. Ferrara, A. Franckowiak, Y. Fukazawa, S. Funk, P. Fusco, F. Gargano, S. Germani, N. Giglietto, P. Giommi, F. Giordano, M. Giroletti, T. Glanzman, G. Godfrey, I. A. Grenier, M.-H. Grondin, J. E. Grove, S. Guiriec, D. Hadasch, Y. Hanabata, A. K. Harding, M. Hayashida, K. Hayashi, E. Hays, J. W. Hewitt, A. B. Hill, R. E. Hughes, M. S. Jackson, T. Jogler, G. Johannesson, A. S. Johnson, T. Kamae, J. Kataoka, J. Katsuta, J. Knodlseder, M. Kuss, J. Lande, S. Larsson, L. Latronico, M. Lemoine-Goumard, F. Longo, F. Loparco, M. N. Lovellette, P. Lubrano, G. M. Madejski, F. Massaro, M. Mayer, M. N. Mazziotta, J. E. McEnery, J. Mehault, P. F. Michelson, R. P. Mignani, W. Mitthumsiri, T. Mizuno, A. A. Moiseev, M. E. Monzani, A. Morselli, I. V. Moskalenko, S. Murgia, T. Nakamori, R. Nemmen, E. Nuss, M. Ohno, T. Ohsugi, N. Omodei, M. Orienti, E. Orlando, J. F. Ormes, D. Paneque, J. S. Perkins, M. Pesce-Rollins, F. Piron, G. Pivato, S. Raino, R. Rando, M. Razzano, S. Razzaque, A. Reimer, O. Reimer, S. Ritz, C. Romoli, M. Sanchez-Conde, A. Schulz, C. Sgro, P. E. Simeon, E. J. Siskind, D. A. Smith, G. Spandre, P. Spinelli, F. W. Stecker, A. W. Strong, D. J. Suson, H. Tajima, H. Takahashi, T. Takahashi, T. Tanaka, J. G. Thayer, J. B. Thayer, D. J. Thompson, S. E. Thorsett, L. Tibaldo, O. Tibolla, M. Tinivella, E. Troja, Y. Uchiyama, T. L. Usher, J. Vandenbroucke, V. Vasileiou, G. Vianello, V. Vitale, A. P. Waite, M. Werner, B. L. Winer, K. S. Wood, M. Wood, R. Yamazaki, Z. Yang, and S. Zimmer
2013. Detection of the characteristic pion-decay signature in supernova remnants. *Science*, 339(6121):807–811.

Arth, A., K. Dolag, A. M. Beck, M. Petkova, and H. Lesch
2014. Anisotropic thermal conduction in galaxy clusters with mhd in gadget.
<http://arxiv.org/abs/1412.6533v2>.

Beck, A. M., K. Dolag, and J. M. F. Donnert
2015a. Geometrical on-the-fly shock detection in sph.
<http://arxiv.org/abs/1511.07444v2>.

- Beck, A. M., K. Dolag, H. Lesch, and P. P. Kronberg
2013. Strong magnetic fields and large rotation measures in protogalaxies from supernova seeding. *Monthly Notices of the Royal Astronomical Society*, 435(4):3575–3586.
- Beck, A. M., G. Murante, A. Arth, R.-S. Remus, A. F. Teklu, J. M. F. Donnert, S. Planelles, M. C. Beck, P. Förster, M. Imgrund, K. Dolag, and S. Borgani
2015b. An improved SPH scheme for cosmological simulations. *Monthly Notices of the Royal Astronomical Society*, 455(2):2110–2130.
- Beck, R. and M. Krause
2005. Revised equipartition and minimum energy formula for magnetic field strength estimates from radio synchrotron observations. *Astronomische Nachrichten*, 326(6):414–427.
- Berezhko, E. G. and D. C. Ellison
1999. A simple model of nonlinear diffusive shock acceleration. *The Astrophysical Journal*, 526(1):385–399.
- Bertschinger, E.
1985. The self-similar evolution of holes in an einstein-de sitter universe. *The Astrophysical Journal Supplement Series*, 58:1.
- Bonafede, A., L. Feretti, M. Murgia, F. Govoni, G. Giovannini, D. Dallacasa, K. Dolag, and G. B. Taylor
2010. The coma cluster magnetic field from faraday rotation measures. *Astronomy and Astrophysics*, 513:A30.
- Brent, R. P.
2013. *Algorithms for Minimization Without Derivatives*. DOVER PUBN INC.
- Brüggen, M. and F. Vazza
2020. Analytical model for cluster radio relics. <http://arxiv.org/abs/2002.02986v1>.
- Brunetti, G., G. Setti, L. Feretti, and G. Giovannini
2001. Particle reacceleration in the coma cluster: radio properties and hard x-ray emission. *Monthly Notices of the Royal Astronomical Society*, 320(3):365–378.
- Brunetti, G., S. Zimmer, and F. Zandanel
2017. Relativistic protons in the coma galaxy cluster: first gamma-ray constraints ever on turbulent reacceleration. *Monthly Notices of the Royal Astronomical Society*, 472(2):1506–1525.
- Caprioli, D. and C. C. Haggerty
2019. The issue with diffusive shock acceleration. <http://arxiv.org/abs/1909.06288>.
- Caprioli, D. and A. Spitkovsky
2014. Simulations of ion acceleration at non-relativistic shocks. i. acceleration efficiency. *The Astrophysical Journal*, 783(2):91.

- Caprioli, D., H. Zhang, and A. Spitkovsky
2018. Diffusive shock re-acceleration. *Journal of Plasma Physics*, 84(3).
- Cassano, R. and G. Brunetti
2005. Cluster mergers and non-thermal phenomena: a statistical magneto-turbulent model. *Monthly Notices of the Royal Astronomical Society*, 357(4):1313–1329.
- Cavaliere, A. and R. Fusco-Femiano
1978. The Distribution of Hot Gas in Clusters of Galaxies. *Astronomy and Astrophysics*, 70:677.
- Chabrier, G.
2003. Galactic stellar and substellar initial mass function. *Publications of the Astronomical Society of the Pacific*, 115(809):763–795.
- Clarke, C. and B. Carswell
2014. *Principles of Astrophysical Fluid Dynamics*. Cambridge University Press.
- de Gasperin, F., R. J. van Weeren, M. Brüggen, F. Vazza, A. Bonafede, and H. T. Intema
2014. A new double radio relic in psz1 g096.89+24.17 and a radio relic mass-luminosity relation. *Monthly Notices of the Royal Astronomical Society*, 444(4):3130–3138.
- Dehnen, W. and H. Aly
2012. Improving convergence in smoothed particle hydrodynamics simulations without pairing instability. *Monthly Notices of the Royal Astronomical Society*, 425(2):1068–1082.
- Dolag, K., M. Bartelmann, and H. Lesch
2002. Evolution and structure of magnetic fields in simulated galaxy clusters. *Astronomy and Astrophysics*.
- Dolag, K. and T. A. Ensslin
2000. Radio halos of galaxy clusters from hadronic secondary electron injection in realistic magnetic field configurations. *Astronomy and Astrophysics*, 362:151–157.
- Dolag, K., F. K. Hansen, M. Roncarelli, and L. Moscardini
2005a. The imprints of local superclusters on the sunyaev-zeldovich signals and their detectability with planck. *Monthly Notices of the Royal Astronomical Society*, 363(1):29–39.
- Dolag, K. and F. Stasyszyn
2009. An MHD gadget for cosmological simulations. *Monthly Notices of the Royal Astronomical Society*, 398(4):1678–1697.
- Dolag, K., F. Vazza, G. Brunetti, and G. Tormen
2005b. Turbulent gas motions in galaxy cluster simulations: the role of smoothed particle hydrodynamics viscosity. *Monthly Notices of the Royal Astronomical Society*, 364(3):753–772.

Donnert, J. and G. Brunetti

2014. An efficient fokker–planck solver and its application to stochastic particle acceleration in galaxy clusters. *Monthly Notices of the Royal Astronomical Society*, 443(4):3564–3577.

Donnert, J. M. F.

2014. Initial conditions for idealized clusters mergers, simulating ‘el gordo’. *Monthly Notices of the Royal Astronomical Society*, 438(3):1971–1984.

Drury, L. O.

1983. An introduction to the theory of diffusive shock acceleration of energetic particles in tenuous plasmas. *Reports on Progress in Physics*, 46(8):973–1027.

Dubois, Y., B. Commerçon, A. Marcowith, and L. Brahim

2019. Shock-accelerated cosmic rays and streaming instability in the adaptive mesh refinement code ramses. *Astronomy and Astrophysics*.

Eilek, J. A.

1979. Particle reacceleration in radio galaxies. *The Astrophysical Journal*, 230:373.

Enßlin, T. A., C. Pfrommer, V. Springel, and M. Jubelgas

2007. Cosmic ray physics in calculations of cosmological structure formation. *Astronomy & Astrophysics*, 473(1):41–57.

Fermi, E.

1949. On the origin of the cosmic radiation. *Physical Review*, 75(8):1169–1174.

Fokker, A. D.

1914. Die mittlere energie rotierender elektrischer dipole im strahlungsfeld. *Annalen der Physik*, 348(5):810–820.

Gennaro, G. D., R. J. van Weeren, M. Hoeft, H. Kang, D. Ryu, L. Rudnick, W. Forman, H. J. A. Röttgering, M. Brüggen, W. A. Dawson, N. Golovich, D. N. Hoang, H. T. Intema, C. Jones, R. P. Kraft, T. W. Shimwell, and A. Stroe

2018. Deep very large array observations of the merging cluster CIZA j2242.8+5301: Continuum and spectral imaging. *The Astrophysical Journal*, 865(1):24.

Gingold, R. A. and J. J. Monaghan

1977. Smoothed particle hydrodynamics: theory and application to non-spherical stars. *Monthly Notices of the Royal Astronomical Society*, 181(3):375–389.

Girichidis, P., C. Pfrommer, M. Hanaasz, and T. Naab

2019. Spectrally resolved cosmic ray hydrodynamics – i. spectral scheme. <http://arxiv.org/pdf/1909.12840>.

Gould, R.

1972. Energy loss of fast electrons and positrons in a plasma. *Physica*, 60(1):145–154.

- Griffin, R. D., X. Dai, and C. S. Kochanek
2014. NEW LIMITS ON GAMMA-RAY EMISSION FROM GALAXY CLUSTERS. *The Astrophysical Journal*, 795(1):L21.
- Guo, X., L. Sironi, and R. Narayan
2014. NON-THERMAL ELECTRON ACCELERATION IN LOW MACH NUMBER COLLISIONLESS SHOCKS. i. PARTICLE ENERGY SPECTRA AND ACCELERATION MECHANISM. *The Astrophysical Journal*, 794(2):153.
- Ha, J.-H., D. Ryu, H. Kang, and A. J. van Marle
2018. Proton acceleration in weak quasi-parallel intracluster shocks: Injection and early acceleration. *The Astrophysical Journal*, 864(2):105.
- Hanasz, M. and H. Lesch
2003. Incorporation of cosmic ray transport into the ZEUS MHD code. *Astronomy & Astrophysics*, 412(2):331–339.
- Hanusch, A., T. V. Liseykina, M. Malkov, and F. Aharonian
2019. Steepening of cosmic ray spectra in shocks with varying magnetic field direction. <http://arxiv.org/abs/1907.09226v2>.
- Helder, E. A., J. Vink, A. M. Bykov, Y. Ohira, J. C. Raymond, and R. Terrier
2012. Observational signatures of particle acceleration in supernova remnants. *Space Science Reviews*, 173(1-4):369–431.
- Hernquist, L.
1990. An analytical model for spherical galaxies and bulges. *The Astrophysical Journal*, 356:359.
- Hillas, A. M.
2006. Cosmic rays: Recent progress and some current questions. <http://arxiv.org/abs/astro-ph/0607109v2>.
- Holman, G. D., J. A. Ionson, and J. S. Scott
1979. Particle streaming - is the alfvén velocity the ultimate speed limit. *The Astrophysical Journal*, 228:576–581.
- Hopkins, P. F., T. K. Chan, S. Garrison-Kimmel, S. Ji, K.-Y. Su, C. B. Hummels, D. Keres, E. Quataert, and C.-A. Faucher-Giguere
2020a. But what about... cosmic rays, magnetic fields, conduction, & viscosity in galaxy formation. *Monthly Notices of the Royal Astronomical Society*, (492):3465.
- Hopkins, P. F., T. K. Chan, S. Ji, C. Hummels, D. Keres, E. Quataert, and C.-A. Faucher-Giguere
2020b. Cosmic-ray driven outflows to mpc scales from l_* galaxies. <http://arxiv.org/abs/2002.02462v1>.

- Kang, H. and T. W. Jones
2007. Self-similar evolution of cosmic-ray-modified quasi-parallel plane shocks.
- Kang, H., V. Petrosian, D. Ryu, and T. W. Jones
2014. Injection of κ -like suprathermal particles into diffusive shock acceleration. *The Astrophysical Journal*.
- Kang, H. and D. Ryu
2013. Diffusive shock acceleration at cosmological shock waves. *The Astrophysical Journal*, 764(1):95.
- Kang, H., D. Ryu, R. Cen, and J. P. Ostriker
2007. Cosmological shock waves in the large-scale structure of the universe: Nongravitational effects. *The Astrophysical Journal*, 669(2):729–740.
- Kardashev, N. S.
1962. Nonstationarity of spectra of young sources of nonthermal radio emission. *Soviet Astronomy*, 6:317.
- Keshet, U., O. Arad, and Y. Lyubarski
2019. Diffusive shock-acceleration: breakdown of spatial diffusion and isotropy. <http://arxiv.org/abs/1910.08083v1>.
- Kudoh, Y. and T. Hanawa
2016. Approximate riemann solvers for the cosmic ray magnetohydrodynamical equations. *Monthly Notices of the Royal Astronomical Society*, 462(4):4517–4531.
- Kulsrud, R. and W. P. Pearce
1969. The effect of wave-particle interactions on the propagation of cosmic rays. *The Astrophysical Journal*, 156:445.
- Lerche, I.
1967. Unstable magnetosonic waves in a relativistic plasma. *The Astrophysical Journal*, 147:689.
- Lucy, L. B.
1977. A numerical approach to the testing of the fission hypothesis. *The Astronomical Journal*, 82:1013.
- Mannheim, K. and R. Schlickeiser
1994. Interactions of cosmic ray nuclei. *Astronomy and Astrophysics*, 286:983–996.
- Maoz, D.
2016. *Astrophysics in a Nutshell*. Princeton University Press.
- Miniati, F.
2001. COSMOCR: A numerical code for cosmic ray studies in computational cosmology. *Computer Physics Communications*, 141(1):17–38.

- Molnar, S. M., N. Hearn, Z. Haiman, G. Bryan, A. E. Evrard, and G. Lake
2009. ACCRETION SHOCKS IN CLUSTERS OF GALAXIES AND THEIR SZ SIGNATURE FROM COSMOLOGICAL SIMULATIONS. *The Astrophysical Journal*, 696(2):1640–1656.
- Morlino, G. and D. Caprioli
2012. Strong evidence for hadron acceleration in tycho’s supernova remnant. *Astronomy & Astrophysics*, 538:A81.
- Pais, M., C. Pfrommer, K. Ehlert, and R. Pakmor
2018. The effect of cosmic ray acceleration on supernova blast wave dynamics. *Monthly Notices of the Royal Astronomical Society*, 478(4):5278–5295.
- Pasternak, B.
in prep. PhD thesis.
- Petrosian, V.
2001. On the nonthermal emission and acceleration of electrons in coma and other clusters of galaxies. *The Astrophysical Journal*, 557(2):560–572.
- Pfrommer, C., R. Pakmor, K. Schaal, C. M. Simpson, and V. Springel
2016. Simulating cosmic ray physics on a moving mesh. *Monthly Notices of the Royal Astronomical Society*, 465(4):4500–4529.
- Pfrommer, C., V. Springel, T. A. Ensslin, and M. Jubelgas
2006. Detecting shock waves in cosmological smoothed particle hydrodynamics simulations. *Monthly Notices of the Royal Astronomical Society*, 367(1):113–131.
- Planck, M.
1917. *Über einen Satz der statistischen Dynamik und seine Erweiterung in der Quantentheorie*. Reimer: Berlin.
- Pohl, M., M. Hoshino, and J. Niemiec
2019. Pic simulation methods for cosmic radiation and plasma instabilities. <http://arxiv.org/abs/1912.02673v1>.
- Price, D. J.
2012. Smoothed particle hydrodynamics and magnetohydrodynamics. *Journal of Computational Physics*, 231(3):759–794.
- Romero, G. E., M. Boettcher, S. Markoff, and F. Tavecchio
2017. Relativistic jets in active galactic nuclei and microquasars. *Space Science Reviews*, 207(1-4):5–61.
- Ryu, D., H. Kang, and J.-H. Ha
2019. A diffusive shock acceleration model for protons in weak quasi-parallel intracluster shocks. <http://arxiv.org/abs/1905.04476v1>.

- Ryu, D., H. Kang, E. Hallman, and T. W. Jones
2003. Cosmological shock waves and their role in the large-scale structure of the universe. *The Astrophysical Journal*, 593(2):599–610.
- Schaal, K. and V. Springel
2014. Shock finding on a moving mesh – i. shock statistics in non-radiative cosmological simulations. *Monthly Notices of the Royal Astronomical Society*, 446(4):3992–4007.
- Schlickeiser, R.
2002. *Cosmic Ray Astrophysics*. Springer Berlin Heidelberg.
- Skilling, J.
1975. Cosmic ray streaming–i EFFECT OF ALFVEN WAVES ON PARTICLES. *Monthly Notices of the Royal Astronomical Society*, 172(3):557–566.
- Sod, G. A.
1978. A survey of several finite difference methods for systems of nonlinear hyperbolic conservation laws. *Journal of Computational Physics*, 27(1):1–31.
- Springel, V.
2005. The cosmological simulation code gadget-2. *Monthly Notices of the Royal Astronomical Society*, 364(4):1105–1134.
- Springel, V. and L. Hernquist
2003. Cosmological smoothed particle hydrodynamics simulations: a hybrid multi-phase model for star formation. *Monthly Notices of the Royal Astronomical Society*, 339(2):289–311.
- Startsev, E. A., R. C. Davidson, and H. Qin
2007. Collective temperature anisotropy instabilities in intense charged particle beams. *Physics of Plasmas*, 14(5):056705.
- Steinwandel, U. P., K. Dolag, H. Lesch, B. P. Moster, A. Burkert, and A. Prieto
2019a. On the origin of magnetic driven winds and the structure of the galactic dynamo in isolated galaxies. <http://arxiv.org/abs/1907.11727v1>.
- Steinwandel, U. P., B. P. Moster, T. Naab, C.-Y. Hu, and S. Walch
2019b. Hot phase generation by supernovae: resolution, chemistry and thermal conduction. <http://arxiv.org/abs/1907.13153v1>.
- Strong, A. W. and I. V. Moskalenko
1998. Propagation of cosmic-ray nucleons in the galaxy. *The Astrophysical Journal*, 509(1):212–228.
- van Weeren, R. J., F. de Gasperin, H. Akamatsu, M. Brüggen, L. Feretti, H. Kang, A. Stroe, and F. Zandanel
2019. Diffuse radio emission from galaxy clusters. *Space Science Reviews*, 215(1).

- van Weeren, R. J., H. J. A. Rottgering, M. Brüggen, and M. Hoeft
2010. Particle acceleration on megaparsec scales in a merging galaxy cluster. *Science*, 330(6002):347–349.
- Vazza, F., M. Brüggen, and C. Gheller
2012. Thermal and non-thermal traces of AGN feedback: results from cosmological AMR simulations. *Monthly Notices of the Royal Astronomical Society*, 428(3):2366–2388.
- Vazza, F., M. Brüggen, D. Wittor, C. Gheller, D. Eckert, and M. Stubbe
2016. Constraining the efficiency of cosmic ray acceleration by cluster shocks. *Monthly Notices of the Royal Astronomical Society*, 459(1):70–83.
- Weibel, E. S.
1959. Spontaneously growing transverse waves in a plasma due to an anisotropic velocity distribution. *Physical Review Letters*, 2(3):83–84.
- White, S. D. M., U. G. Briel, and J. P. Henry
1993. X-ray archaeology in the coma cluster. *Monthly Notices of the Royal Astronomical Society*, 261(1):L8–L12.
- Winner, G., C. Pfrommer, P. Girichidis, and R. Pakmor
2019. Evolution of cosmic ray electron spectra in magnetohydrodynamical simulations. *Monthly Notices of the Royal Astronomical Society*.

List of Figures

1.1.	Illustration of Weibel instability caused by a shock moving in x-direction. Taken from Startsev et al. (2007).	2
1.2.	CR propagation along a regular and irregular magnetic field line. Adopted from Pasternak (prep).	4
1.3.	Gyration of charged particles in irregular magnetic fields. r_g describes the gyro radius of the particle, while λ is the typical scale of the irregularities. Adopted from Pasternak (prep).	4
1.4.	Cooling times of different loss mechanisms for protons and electrons. Dotted lines indicate the typical energy range used for the simulations in this work.	10
1.5.	From van Weeren et al. (2019): <i>Left panel</i> : Spectral index map for the double radio shock in PSZ1G108.18–11.53 between 323 and 1380 MHz from de Gasperin et al. (2014). For both radio shocks, the spectral index steepens in the direction towards the cluster center. The 323 MHz radio contours are overlaid in black at levels of [1, 4, 16, ...] $\times 4\sigma_{\text{rms}}$, where σ_{rms} is the map noise. <i>Right panel</i> : Combined radio (red, GMRT 323 MHz) and X-ray (blue, Chandra 0.5–2.0 keV) image of PSZ1G108.18–11.53	14
1.6.	From van Weeren et al. (2019): <i>Top panel</i> : Spectral index distribution across the northern cluster radio shock in CIZA J2242.8+5301 between 0.15 and 3.0 GHz at 5" resolution (Gennaro et al. (2018)). Black contours are from a 1–4 GHz continuum image. Contours are drawn at levels of [1, 4, 16, ...] $\times 5\sigma_{\text{rms}}$, where σ_{rms} is the map noise. <i>Bottom panel</i> : Polarized intensity image at 3 GHz (Di Gennaro et al. in prep). Overlaid are the polarization electric field vectors corrected for Faraday Rotation. Black contours are the same as for the top panel	15
2.1.	Schematics of the shockfinder. Taken from Beck et al. (2015a).	22
2.2.	Results of the shockfinder performance tests. Left to right panels display density, velocity component in x direction, internal energy of the gas and machnumber of the resulting shock. The red errorbars in the machnumber panels indicate the mean size of the kernel support. Included in these panels is information in the target machnumber, the width of the shock in units of the mean kernel support, as well as the number of SPH particles within the shock.	25
3.1.	Example parameterspace of the slope.	33

4.1.	Example for the modelling of the efficiency functions. Points correspond to the datapoints provided by the respective authors and lines show the fit.	37
4.2.	Comparison of all implemented DSA models.	39
4.3.	Result of a Mach 6 shocktube test with the Ryu et al. (2019) efficiency model. Dashed lines show the analytic solution, solid lines the result of the simulation. Every particle is plotted.	39
4.4.	Result of all shocktubes with Ryu et al. (2019) efficiency. Shown are the ratios of the resulting CR energy in the post shock region divided by the ideal energy obtained via our modification of the Riemann solver for CR acceleration proposed by Pfrommer et al. (2016).	40
4.5.	Shown here is the accuracy with which we can capture the angle between the shock-normal and the B-field. The bars correspond to a histogram normalized to the total number of shocked particles. They are binned in 1° bins $\pm 5^\circ$ around the target value for θ_B . The lines show a gaussian fit to the data with the values for mean (μ) and standard deviation (σ) next to the fit.	43
4.6.	Shock angle and θ_B efficiency a particle experiences over the shock duration with fixed B.	44
4.7.	Left: $\eta(\theta_B)$ as a function of θ_B . The simulation values are obtained from the median value of a segment of the post-shock region, indicated with grey dashed vertical lines in the right plot. Right: CR pressure component in the postshock region. Dashed lines indicate the ideal solution, solid lines the result from the simulations. Colors correspond to the input value of θ_B as in the previous plots.	44
4.8.	Shock angle and θ_B efficiency a particle experiences over the shock duration with B-field evolution.	45
4.9.	Left: Measured and ideal slopes of the resulting power spectrum. Right: relative error of the compression ratio in the simulation and the ideal solution.	46
4.10.	Left: Analytic solution to the compression ratio as a function of Mach number for different efficiency models. Right: Analytic solution to the resulting powerlaw slope from standard DSA.	47
4.11.	Early snapshot of an isolated galaxy simulation. Left shows gas density, while right shows the magnetic field. Contour lines indicate the modelled synchrotron emission by CR electrons. They are normalized to the maximum emission and spaced out by an order of magnitude in intensity.	50
5.1.	Collapse and expansion test without bin interpolation.	52
5.2.	Schematics of fluxes at the boundary conditions. Adopted from Pasternak (prep).	53
5.3.	Collapse and expansion test with bin interpolation.	56
5.4.	Relative error of the adiabatic bounce test after the collapse phase (solid lines) and after the expansion phase (dashed lines).	57
5.5.	Result of a shocktube test with a seed CR population and $P_{cr} = 0.3 P_{th}$	59

5.6.	Evolution of the densities as a function of cosmological scale factor. While the comoving density increases (right y-axis) the physical density decreases because of the cosmic expansion.	60
5.7.	Relative change of pressure under adiabatic expansion.	61
5.8.	Top: Spectral evolution of the initial distribution (dashed line). As in the non-cosmological case a decrease in density, hence adiabatic expansion, leads to a left-shift of the distribution function. The slope of the bins below the cut-off should remain constant and does so in the simulation. Bottom: Change of the slope of the bins below the cut-off. As can be seen the slope stays nicely constant over the whole simulation.	63
6.1.	Synchrotron cooling with $B_x = 5\mu G$ and inverse Compton scattering at $z = 0$ with 192 momentum bins.	67
6.2.	Convergence to the analytic solution for synchrotron and inverse Compton cooling for different numbers of momentum bins.	68
7.1.	Distribution function shift due to turbulent re-acceleration with constant momentum diffusion coefficient $D_{pp} = 10^{-18} \frac{1}{s}$	75
7.2.	Left: Test of simultaneous synchrotron losses and D_{pp} reacceleration. Shown are the cutoffs of the spectra relative to the initial cut. Blue: Pure synchrotron losses. Black: Synchrotron losses balances by D_{pp} reacceleration. Right: $D_0(t)$ obtained from a cluster merger simulation with infalling substructure.	75
8.1.	Initial conditions of the cluster merger. Left shows the gas surface density, right shows the magnetic field. Both images are mapped to a grid using a 5 Mpc slice of the box.	78
8.2.	Left panels: Surface density overplotted by Mach number. Right panels: Surface density overplotted by CR to thermal pressure ratio X_{cr} . Top: State of the merger shortly after initial contact of the halos. Bottom: State of the merger shortly after first passage of the cluster cores.	80
8.3.	As in Fig. 8.2. Top: State of the merger after the second core passage with outwards moving shock front. Bottom: End of the simulation with merged clusters, still undergoing relaxation.	81
8.4.	Zoom on the first developing shockfront. The background indicates surface density, colors show the Mach number and the white lines represent size and location of the slice for Fig. 8.5	83
8.5.	Particle properties within the slice indicated in Fig. 8.4.	84
8.6.	Properties a particles experiences over the first shockfront.	86
8.7.	Top: Spectral evolution of a single particle. Left: Protons. Right: Electrons. Bottom: Density evolution of the same particle.	87
IV.1.	Fully developed hydrodynamic shock with a target mach-number of Mach 10. Blue solid lines show the simulation result of the OpenGadget3 code, while red dashed lines indicate the ideal solution.	108

IV.2. Result of a Mach 3 shock with Gadget (green) and Arepo (blue). For Gadget we used the SPH improvements by Beck et al. (2015b). Arepo uses a static mesh. Both runs were performed with the same initial conditions.	110
IV.3. The same as Fig. IV.2 with a Mach 30 shock.	111
IV.6. Result of a Mach 10 shocktube with a seed CR population of $X_{cr} = 0.3$	113
IV.9. Performance of simulations with synchrotron and IC cooling.	114
IV.10. Initial condition of the cluster merger simulation with substructure.	115
IV.4. Shocktube tests for the efficiency model by Kang and Ryu (2013). From top to bottom: Pressure, density, energy and shock finder. From left to right: Shocks with Mach numbers 3, 4, 6, 10, 30, 60 and 100. We find overall excellent agreement.	116
IV.5. Shocktube tests for the efficiency model by Kang and Ryu (2013) and a pre-existing CR component. From top to bottom: Pressure, density, energy and shock finder. From left to right: Shocks with Mach numbers 3, 4, 6, 10, 30, 60 and 100. We can't compare to the analytic solution yet, but find more CR acceleration in the low Mach number shocks than in Fig. IV.4, which is expected by the more efficient re-acceleration by the shock.	117
IV.7. Result of a set of shocktube tests with only adiabatic expansion and no CR acceleration.	118
IV.8. Spectral distribution multiplied by p^{q_0} , where q_0 is the initial powerlaw slope.	119

List of Tables

5.1. Values for compression factor, upstream CR pressure, ideal solution and simulation data of the downstream CR pressure and the corresponding error for a set of shocktube tests with Mach numbers ranging from Mach 3 to Mach 100.	59
8.1. Properties of the merging halos.	79

IV. Appendix

IV.1. Technical Setup of Sod Shocktubes

As a reference for future work this section gives a short manual on how to set up simple shocktubes in SPH. These shocktubes were first investigated by Sod (1978), therefore they are often simply called "Sod-shocks". Sod-shocks start out as a contact discontinuity in density and pressure with all particles initially at rest. The first step is to obtain the contact discontinuity in density. The right-hand side of this contact discontinuity can be easily obtained by constructing a cube with a side-length of 1 and almost any number of particles. For SPH one only has to account for the minimum number of neighbors in the kernel to avoid self-interaction. To avoid numerical noise it is best to use a glass-like distribution for the cube. This glass-like distribution can be obtained by setting up the particles in a grid (or randomly) and letting it relax by running the cube in a SPH code for a long while. The run should be reset a number of times by looking for the snapshot with the lowest mean velocity of all particles, setting all particle velocities of that snapshot to zero and using this file as a new IC. This process should be repeated until the particles show hardly any movement after the end of the simulation. This guarantees that the particles are as force-free as possible and have found an equilibrium state.

The left-hand side of the density discontinuity can be obtained by using the same cube from the right and stacking it in such a way that a new large cube consisting of four small cubes is constructed. The particles distances are then divided by two, to assure that the large cube also has a side-length of one. This then results in the common density jump of $\rho_L = 1.0$ to $\rho_R = 1/8$.

These two boxes can then be used to build a tube by stacking them in x-direction. The number of stacks is arbitrary, although one should take care that the tube is long enough to avoid interference from the back-running wave. Since shocktubes have to be run with periodic boundary conditions there are two contact discontinuity, one in the middle of the tube and one where the ends of the tube are connected by the periodicity. Commonly a number of 70 stacks is used to get a tube of length 140.

After the tube is set up the pressure jump can be constructed from the equation of state

$$P = (\gamma - 1) \rho U \tag{IV.1}$$

and the resulting U values can be written to the IC file.

IV.2. Exact Riemann Solver

A Sod-shock can be split into 5 zones, as shown in Fig. IV.1.

Sod Shock
Mach 10 $t = 1.5$

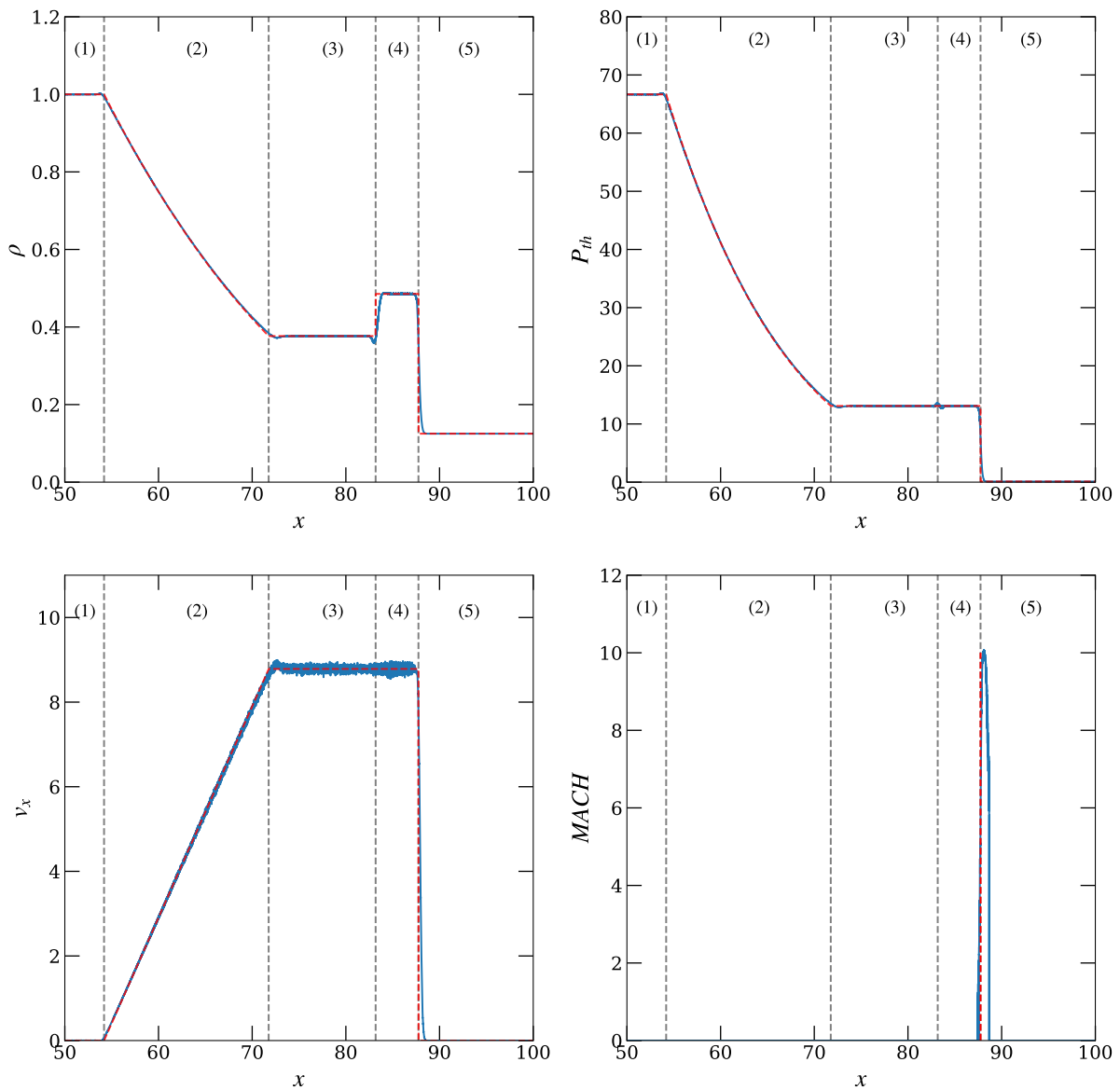


Figure IV.1.: Fully developed hydrodynamic shock with a target mach-number of Mach 10. Blue solid lines show the simulation result of the OpenGadget3 code, while red dashed lines indicate the ideal solution.

- (1) Initial state left
- (2) Rarefaction state
- (3) Constant state
- (4) Post-shock region
- (5) Initial state right

Initial conditions need to contain: P_5, P_1, ρ_1, ρ_5 . Optionally U instead of P.
This also gives speed of sound at both ends of shock tube:

$$c_{1,5} = \sqrt{\gamma_{th} \frac{P_{1,5}}{\rho_{1,5}}} \quad (\text{IV.2})$$

To find P_{34} solve:

$$\frac{2}{\gamma_{th} - 1} \frac{c_1}{c_5} \left(1 - \left(\frac{P_{34}}{P_1} \right)^{\frac{\gamma_{th}-1}{2\gamma}} \right) = \left(\frac{P_{34}}{P_5} - 1 \right) \sqrt{\frac{1 - \eta}{\gamma_{th} \left(\frac{P_{34}}{P_1} + \eta \right)}} \quad (\text{IV.3})$$

with

$$\eta = \frac{\gamma_{th} - 1}{\gamma_{th} + 1} . \quad (\text{IV.4})$$

Now we can solve the velocity component in the post-shock region:

$$v_{34} = \frac{2c_1}{\gamma_{th} - 1} \left(1 - \left(\frac{P_{34}}{P_1} \right)^{\frac{\gamma_{th}-1}{2\gamma}} \right) \quad (\text{IV.5})$$

Next we solve the post-shock density, defined by the Mach number and the adiabatic coefficient:

$$\rho_4 = \frac{(\gamma_{th} - 1)M^2}{2 + (\gamma_{th} - 1)M^2} \rho_5 \quad (\text{IV.6})$$

Final ρ component:

$$\rho_3 = \rho_1 \left(\frac{P_{34}}{P_1} \right)^{\frac{1}{\gamma_{th}}} \quad (\text{IV.7})$$

Other velocity components can now be solved:

$$v_s = \frac{v_{34}}{1 - \frac{\rho_5}{\rho_4}} \quad (\text{IV.8})$$

$$v_t = c_1 - \frac{v_{34}}{1 - \eta} \quad (\text{IV.9})$$

IV.3. Additional Figures

IV.3.1. Section 2

Arepo Tests Mach 3.0 $t = 1.5$

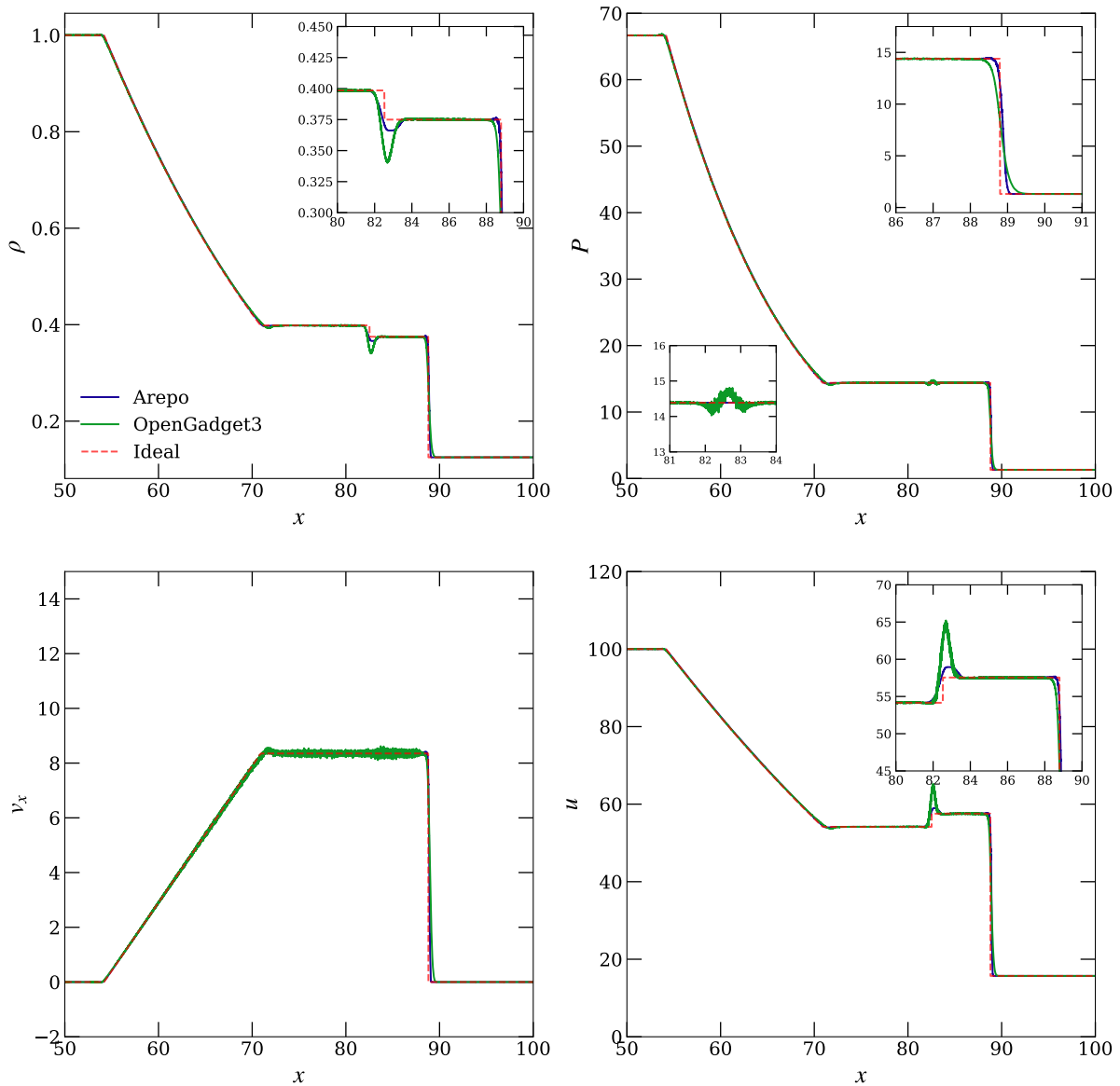


Figure IV.2.: Result of a Mach 3 shock with Gadget (green) and Arepo (blue). For Gadget we used the SPH improvements by Beck et al. (2015b). Arepo uses a static mesh. Both runs were performed with the same initial conditions.

Arepo Tests
Mach 30.0 $t = 1.5$

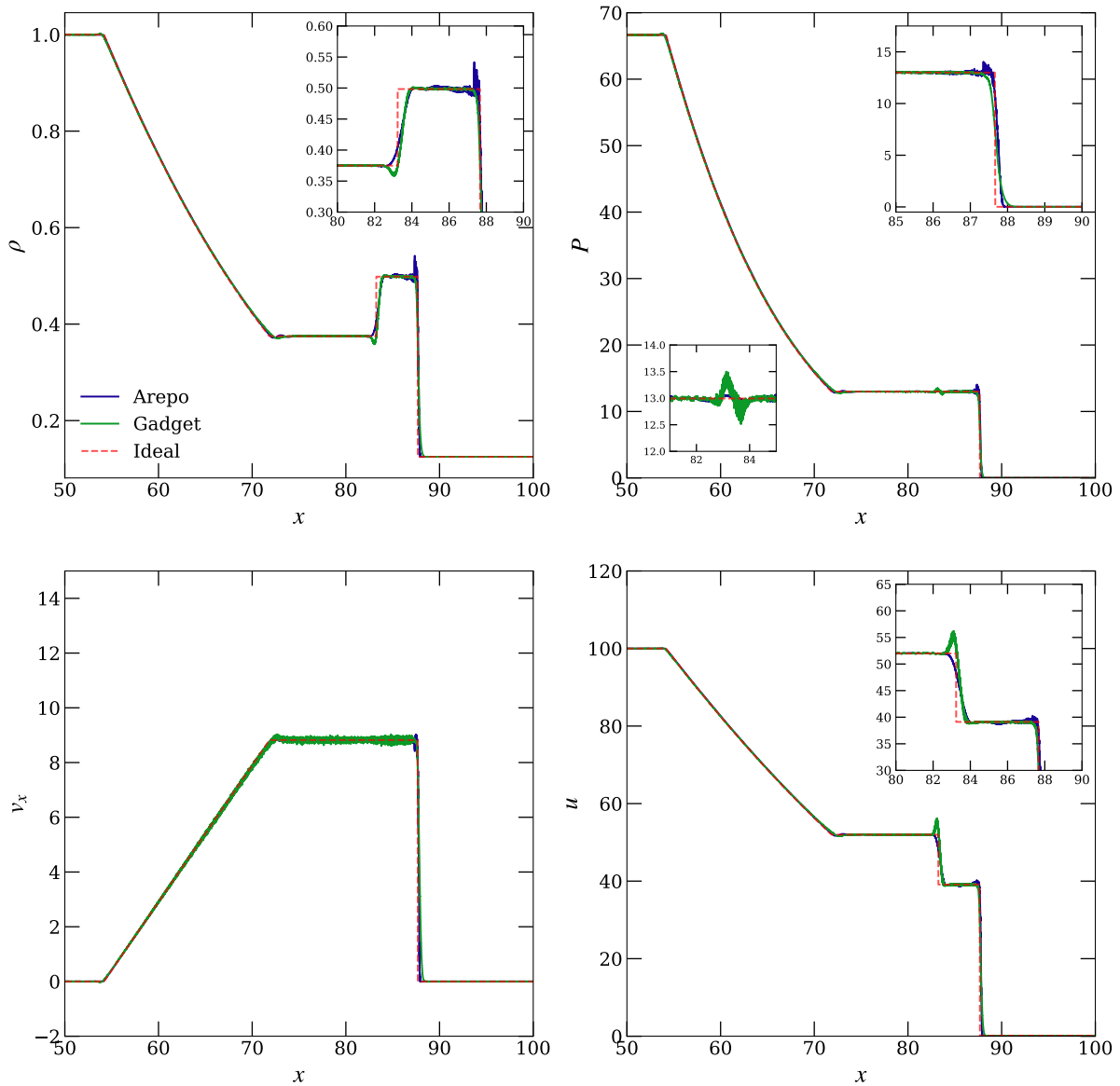


Figure IV.3.: The same as Fig. IV.2 with a Mach 30 shock.

IV.3.2. Section 4

IV.3.3. Section 5

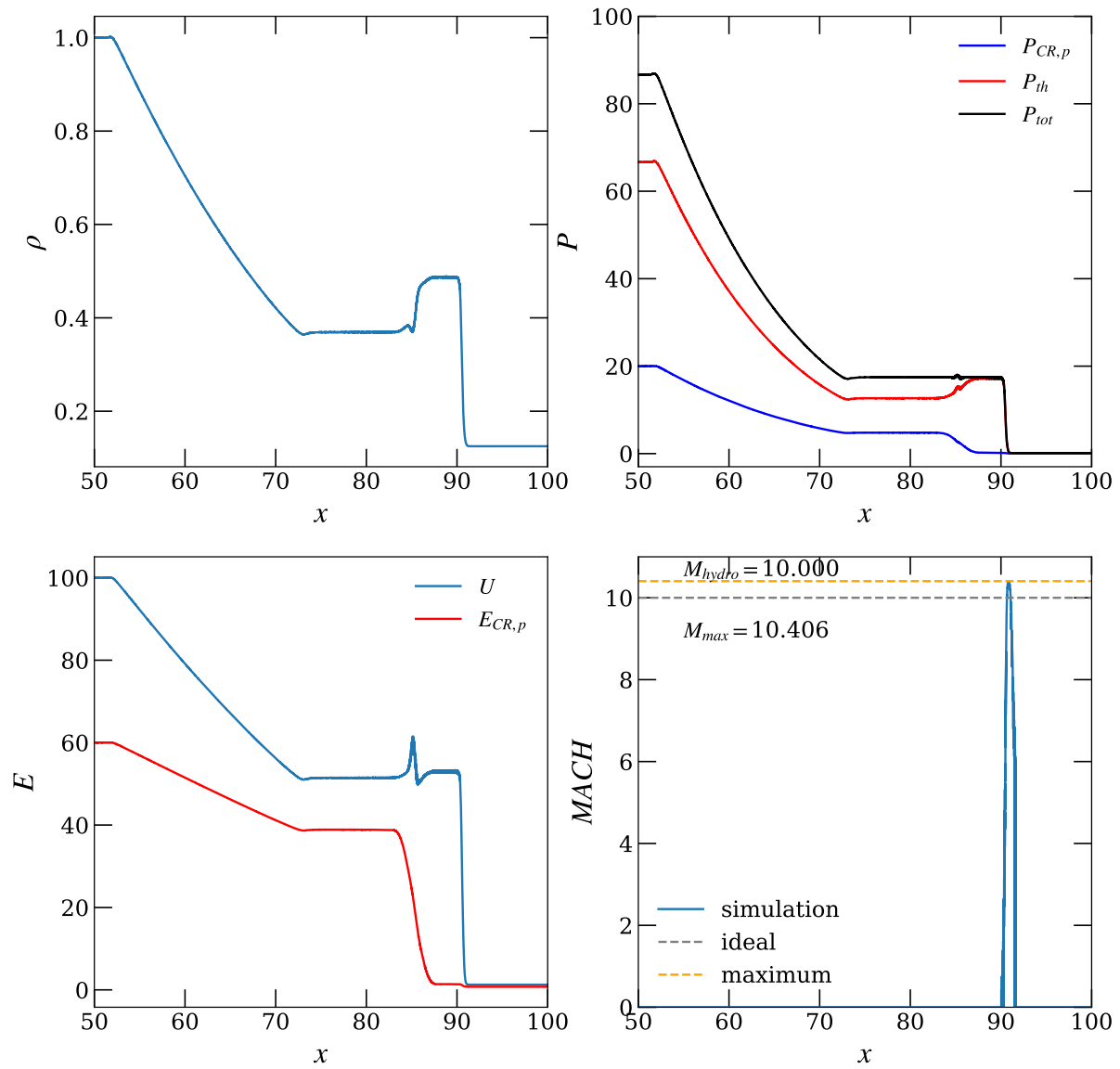


Figure IV.6.: Result of a Mach 10 shocktube with a seed CR population of $X_{cr} = 0.3$.

IV.3.4. Section 6

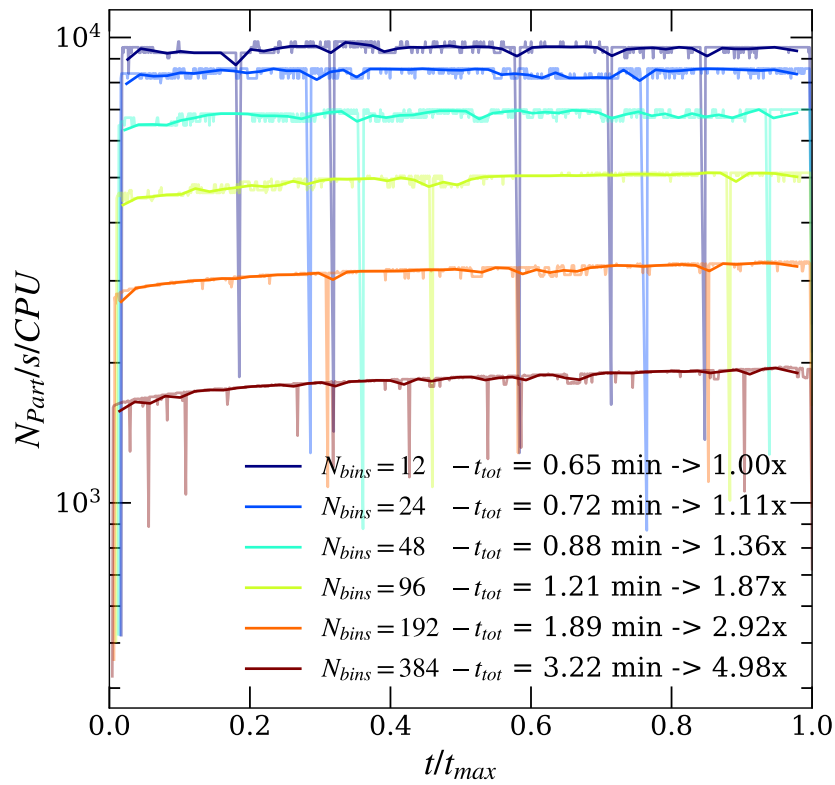


Figure IV.9.: Performance of simulations with synchrotron and IC cooling.

IV.3.5. Section 7

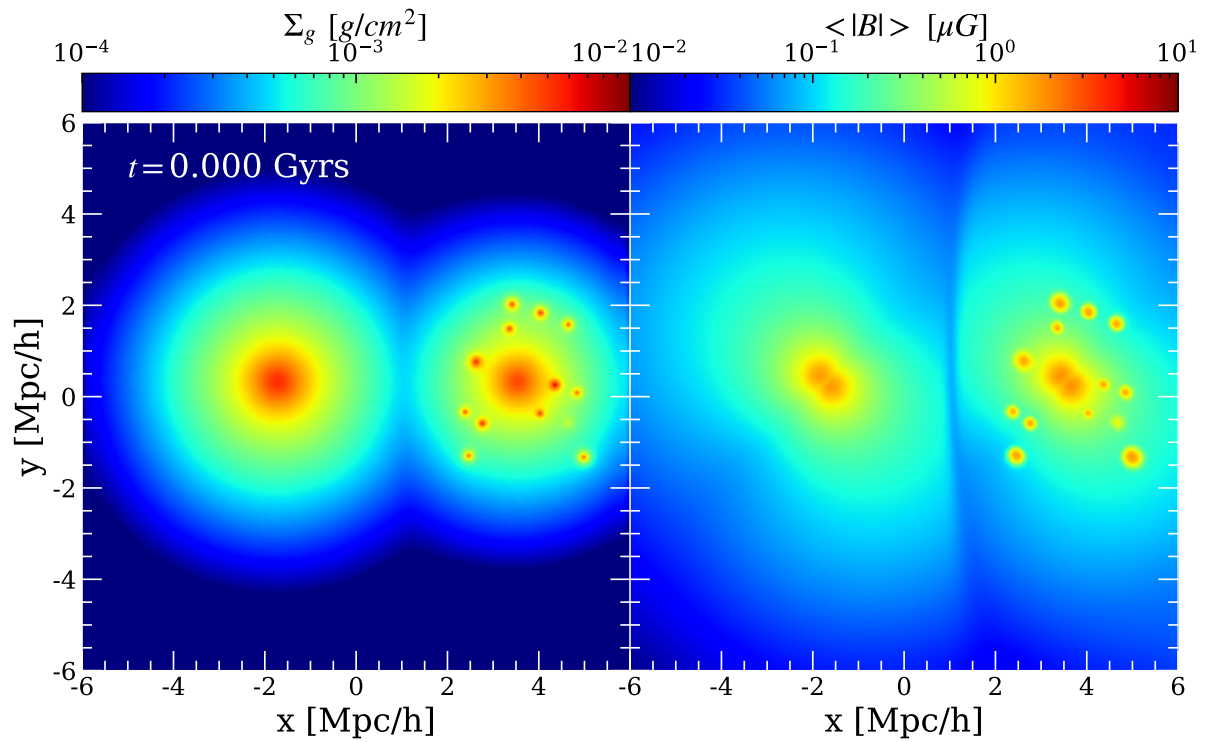


Figure IV.10.: Initial condition of the cluster merger simulation with substructure.

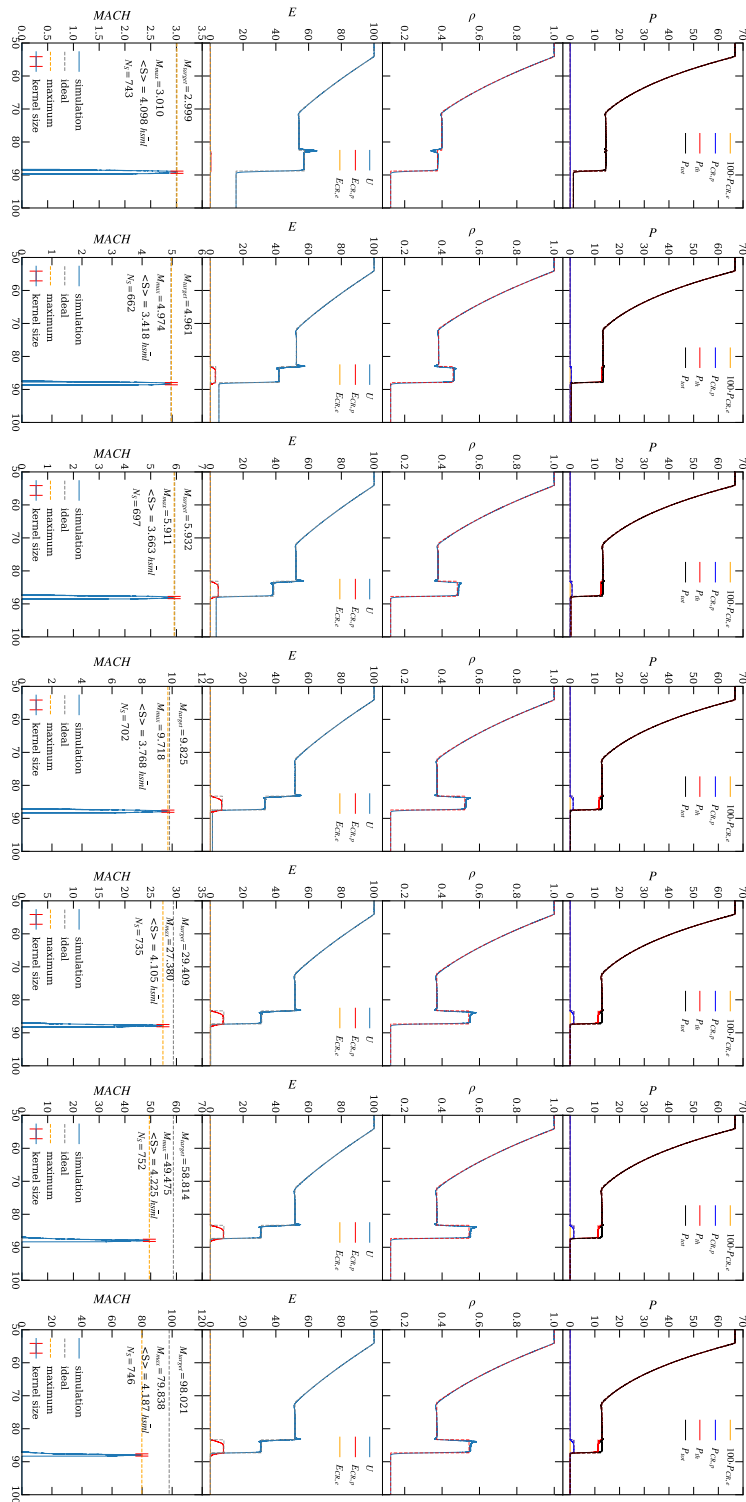


Figure IV.4: Shocktube tests for the efficiency model by Kang and Ryu (2013). From top to bottom: Pressure, density, energy and shock finder. From left to right: Shocks with Mach numbers 3, 4, 6, 10, 30, 60 and 100. We find overall excellent agreement.

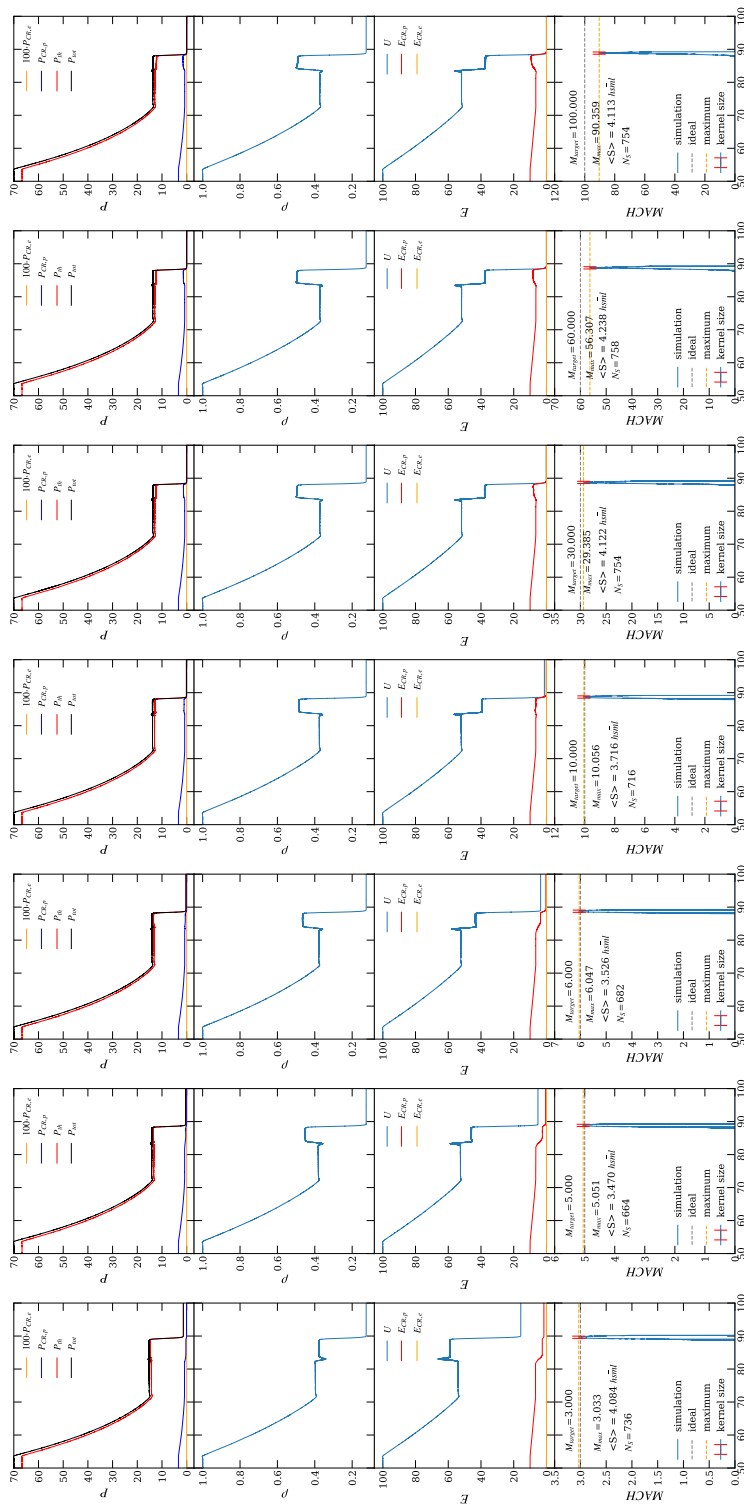


Figure IV.5: Shocktube tests for the efficiency model by Kang and Ryu (2013) and a pre-existing CR component. From top to bottom: Pressure, density, energy and shock finder. From left to right: Shocks with Mach numbers 3, 4, 6, 10, 30, 60 and 100. We can't compare to the analytic solution yet, but find more CR acceleration in the low Mach number shocks than in Fig. IV.4, which is expected by the more efficient re-acceleration by the shock.

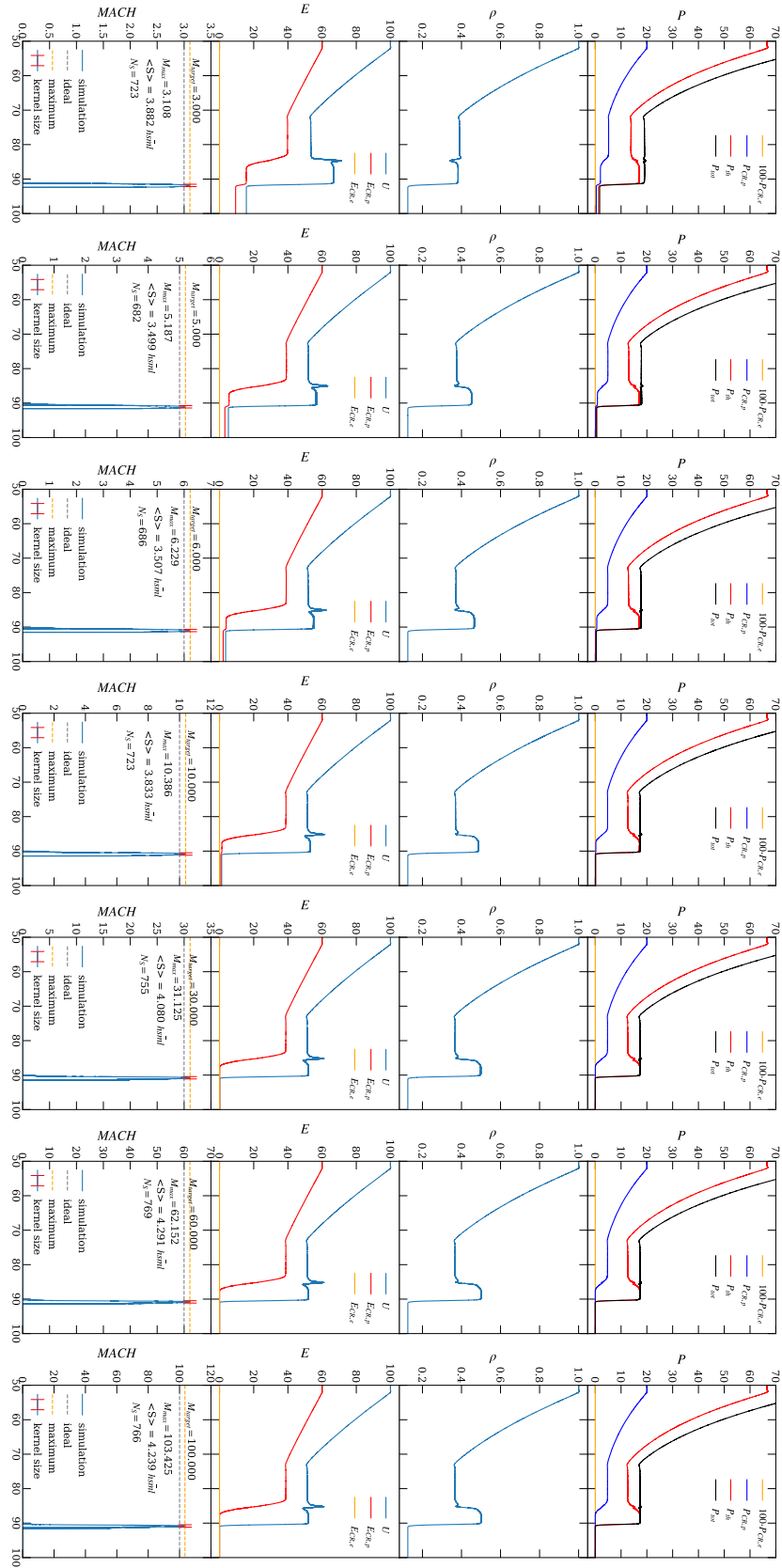


Figure IV.7.: Result of a set of shocktube tests with only adiabatic expansion and no CR acceleration.

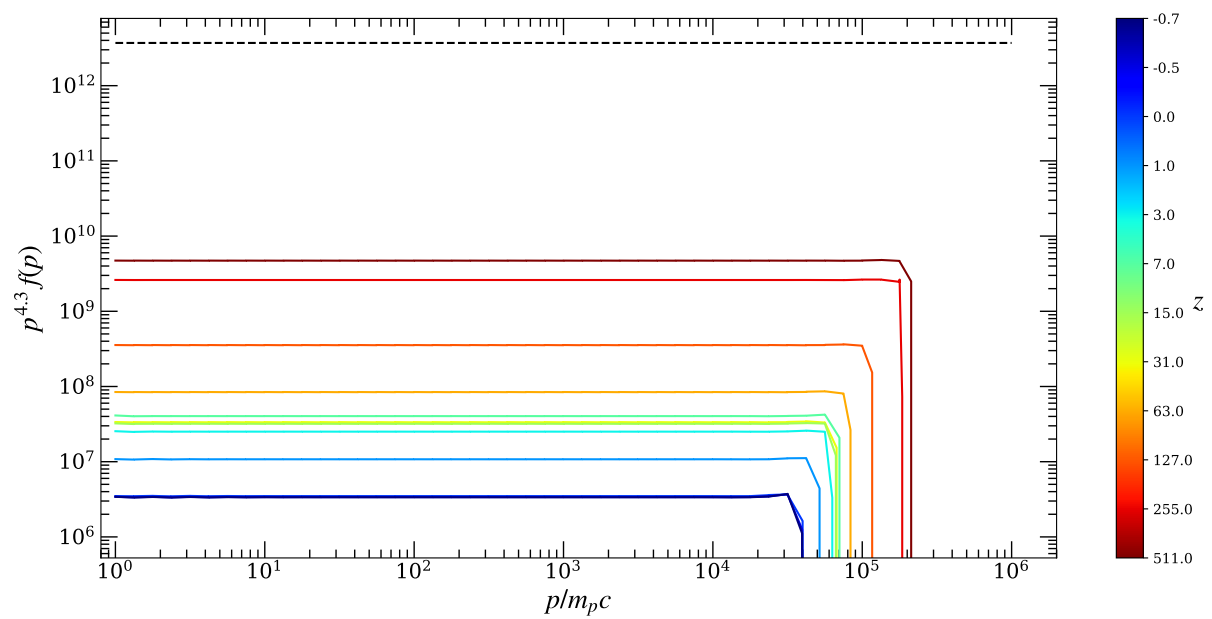


Figure IV.8.: Spectral distribution multiplied by p^{q_0} , where q_0 is the initial powerlaw slope.

V. Acknowledgements

Vielen Dank an

Klaus Dolag für dieses spannende Thema, super Betreuung und viel Freiraum um selbstständig zu arbeiten und eigene Ideen einzubringen. Es hat mir sehr viel Spaß gemacht und ich freu mich darauf wie es weiter geht!

Nadia Wildner, dass du schon die zweite Abschlussarbeit mit mir durchgestanden hast. Ohne deine Unterstützung und Fürsorge wäre ich wahrscheinlich eingegangen. ;)

Harald Lesch für anschauliche, intuitive Erklärungen von komplexen Zusammenhängen. Ich freu mich auf die nächsten Jahre!

Ulrich Steinwandel für Hilfe, gute Diskussionen, Motivation und einen konstanten Fluss von Spongebob Memes.

Paul Hinz für tolle Zusammenarbeit über das letzte Jahr, eine super Zeit auf Teneriffa und das Korrekturlesen der Arbeit.

Joseph O’Leary for helpful discussions and great food on Tenerife and in Munich. Also: so. many. memes.

Felix Schulze für morgendliche Unterhaltungen nach dem Wasser holen und einfach allgemeines Felix-sein.

Beata Pasternak for great preliminary work that I could extend upon. Also for providing her standalone implementations so that I was able to compare my results to hers.

Die CAST Gruppe für eine lustige Zeit die mir das Arbeiten hier sehr angenehm gemacht hat.

VI. Selbstständigkeitserklärung

Hiermit erkläre ich, die vorliegende Arbeit selbständig verfasst zu haben und keine anderen als die in der Arbeit angegebenen Quellen und Hilfsmittel benutzt zu haben.

München, am 24. Februar 2020,

Ludwig Böss